University of South Florida
Scholar Commons

Graduate Theses and Dissertations | Graduate School

January 2014

DC and RF Characterization of High Frequency ALD Enhanced Nanostructured Metal-Insulator-Metal Diodes

Olawale Adebimpe Ajayi
University of South Florida, oajayi@mail.usf.edu

Follow this and additional works at: http://scholarcommons.usf.edu/etd

Part of the Nanoscience and Nanotechnology Commons

Scholar Commons Citation
Ajayi, Olawale Adebimpe, "DC and RF Characterization of High Frequency ALD Enhanced Nanostructured Metal-Insulator-Metal Diodes" (2014). *Graduate Theses and Dissertations.*
http://scholarcommons.usf.edu/etd/5166

This Dissertation is brought to you for free and open access by the Graduate School at Scholar Commons. It has been accepted for inclusion in Graduate Theses and Dissertations by an authorized administrator of Scholar Commons. For more information, please contact scholarcommons@usf.edu.

DC and RF Characterization of High Frequency ALD Enhanced Nanostructured Metal-Insulator-Metal Diodes

by

Adebimpe Olawale Ajayi

A dissertation submitted in partial fulfillment
of the requirements for the degree of
Doctor of Philosophy
Department of Electrical Engineering
College of Engineering
University of South Florida

Co-Major Professor: Jing Wang, Ph.D.
Co-Major Professor: Gokhan Mumcu, Ph.D.
Sanjukta Bhanja, Ph.D.
Delcie Durham, Ph.D.
Sarath Witanachchi, Ph.D.
Andrew Hoff, Ph.D.

Date of Approval:
June 30, 2014

Keywords: Tunneling, Barrier Height, Metallic Oxides, Transmission Probability, Impedance

Copyright © 2014, Adebimpe Olawale Ajayi

DEDICATION

This dissertation is dedicated to the loving memory of my maternal grandparents Mr. Bankole Dada Jacob and Mrs. Bankole Fakorede Elizabeth. You made everything happen. You believe in me even when I doubt my God given ability. I cannot forget how both of you combined your little resources for my educational causes. I will continually cherish your love and affection. Thank you Papa and Mama.

ACKNOWLEDGMENTS

First and foremost, I would like to thank my God and my savior, who is the author and finisher of my faith. THANK YOU LORD.

I want to appreciate my two advisers who patiently walked through this long journey with me, Dr. Jing Wang and Dr. Gokhan Mumcu. Thank you for your guidance, inspiration, motivation, insight and support throughout my entire doctorate program. I would also like to express gratitude to the members of my dissertation committee for their understanding, helpful advice and suggestions: Dr. Sanjukta Bhanja, Dr. Delcie Durham, Dr. Sarath Witanachchi, and Dr. Andrew Hoff.

I would also like to thank all my group members for their understanding, contribution and sharing some of their precious time with me when there was need for it, Ahmad Gheethan, Patrick Nesbitt, Saurabh Gupta, Abhishek Dey, I-Tsang Wu, Ivan Rivera, and Mian Wei. I would especially like to thank Patrick Nesbitt, who is my buddy all the way in the clean room, noise laboratory and in developing the codes.

I will like to acknowledge the assistance of all the staff of the Nanotechnology Research and Education Center at the University of South Florida for their constant help and support: Robert Tufts, Everly Richard and Louise-Jeune Sclafani. Thank you.

In addition, I would like to acknowledge the support of the Center for Nanoscale Materials Argonne at Argonne National Laboratory for allowing me to use their tools to fabricate the nano-size devices. Dr. David Czaplewski, thank you for working with me in the clean room

to get the work done in a timely manner. Your patience to show me how to operate the E-Beam tool for the fabrication goes a long way.

I would also like to sincerely express gratitude to all my family at USF: Dr. Tony Price and Dr. Dorielle Price (thank you so much, we did it together), Innocent Udom (you are such a wonderful friend – I appreciate you and your family), Edikan Archibong (thank you sister), Dr. Frank Alexander (I appreciate you), Dr. Al-Aakhir Rogers and Mr. Bernard Batson. Thank you for all your support during the course of this journey.

I would also like to thank the administrative staff of the Electrical Engineering Department: Cherie Dilley, Judy Hyde and Jessica Procko – thank you for your patience, assistance and understanding. To the staff of International Services at USF, especially Marcia Taylor, Thora Collymore and Daniela Mui, I appreciate you all.

I would also like to express my appreciation to the National Science Foundation for their financial support throughout the work in this dissertation, from National Science Foundation (NSF) under Grant: ECCS-1029067.

To my extended families and friends, Mr. and Mrs. Gbenga Aguda, Mr. Michael Sekoni and Dr. Kenya Sekoni, Mr. Banjo Adedeji and Dr. Kofo Adedeji, Mr. and Mrs. Gbenga Oderinde, Mr. and Mrs. Tope Odewale, Mr. and Mrs. Olusegun Ayuba, Mr. and Mrs. Keneth Sobola, and Mr. and Mrs. Olu-Ajayi Komolafe. I appreciate you for all the support. To my father in the Lord, Dr. Gabriel Dada, thank you. I would also like to say a big thank you to Dr. and Mrs. Taiwo Ajani for taking time out of their busy schedules to read through this dissertation.

My mother, Mrs. Mary Abike Ajayi, we did this together. The journey has been long, but we finished it together. I want to thank you for your financial, moral, and spiritual support. Thank you for understanding, even when we disagree. I could never trade you for anything. To

my siblings, Mr. Kayode Ojo-Osagie, Mr. Gbenga Ojo-Osagie, Mrs. Funmi Ojo-Osagie, Mr. Damola Olatidoye, Mrs. Yemisi Olatidoye, and Mr. Ayotunde Daniel Ajayi, thank you for your understanding and support. To my in-laws, Mr. and Mrs. Idown Otubusin, Bayo, Bimbo, Femi and Tolu, thank you for all your support.

Most importantly, I will like to thank the most important woman in my life, Yetunde Atinuke Ikemi Ajayi, my partner through this journey. You're truly a life partner, a friend, and companion. Thank you for your spiritual and moral support. There is no way I would have gone through this five years journey without you. None of your sacrifice is taken for granted. To our two adorable sons, Oluwapelumi Ijerisi and Ebunife Araoluwa, words cannot describe how appreciative I am to both of you. Thank you for your understanding. I love you.

TABLE OF CONTENTS

LIST OF TABLES ... iv

LIST OF FIGURES ... vi

ABSTRACT ... xi

CHAPTER 1: INTRODUCTION ... 1
1.1 Background ... 2
1.2 Terahertz Radiation ... 5
1.2.1 Detection of THz Radiation ... 7
1.3 Dissertation Overview ... 10
1.4 Goals ... 11
1.5 Research Objectives ... 12
1.6 Dissertation Organization ... 13

CHAPTER 2: THEORETICAL ANALYSIS OF MIM TUNNELING DIODES ... 15
2.1 MIM Tunneling Diode Model ... 15
2.1.1 Analysis of TMM Formulation ... 21
2.1.2 WKB Approximation ... 28
2.2 Multi Tunnel Layer MIM Diode ... 28
2.2.1 TMM Method ... 28
2.2.2 WKB for Multi-tunnel layer ... 29
2.3 Characteristics of MIM Diode ... 29
2.3.1 Current-Voltage (*I*-*V*) Characteristics ... 29
2.3.2 Nonlinearity ... 34
2.3.3 Asymmetry ... 35
2.3.4 Rectification and Mixing Operation ... 35
2.3.5 MIM Diode Performance and RC Time Constant ... 36

CHAPTER 3: MIM DIODE FABRICATION PROCESSING ... 38
3.1 Lithography ... 38
3.1.1 Optical Lithography ... 38
3.1.2 Electron Beam Lithography ... 42
3.2 Scanning Electron Microscope (SEM) for E-beam Lithography ... 44
3.3 Thin Film Deposition ... 49
3.3.1 Atomic Layer Deposition (ALD) ... 51
3.4 Etching ... 54
3.5 Device Fabrication and Metrology ... 55
3.5.1 Device Fabrication Process ... 55

3.5.1.1 Substrates 56
3.5.1.2 Metal Selection 58
3.5.1.3 Micro Device Mask Design 59
3.5.1.4 Metal Oxide 62
3.5.1.5 Fabrication 63
3.5.2 Metrology..65
3.6 Summary 68

CHAPTER 4: DC CHARACTERIZATION 69
4.1 DC Experimental Setup 69
4.1.1 Characteristics of Pt-HfO_2-Ti MIM Diodes with 2nm-thick Tunnel Layer 71
4.1.2 Characteristics of Pt-HfO_2-Ti MIM Diodes with 3nm-thick Tunnel Layer 73
4.1.3 Characteristics of Pt-TiO_2-Ti MIM Diodes with 3nm-thick Tunnel Layer 74
4.1.4 Characteristics of Pt-TiO_2-Ti MIM Diodes with 4nm-thick Tunnel Layer 76
4.2 Characteristics of Multi-layer MIIM Diode (Pt-HfO_2-TiO_2-Ti) 80
4.3 Barrier Height Extraction..87
4.4 Summary 90

CHAPTER 5: FABRICATION AND CHARACTERIZATION OF MIM/MIIM DIODES WITH NANOSCALE JUNCTIONS 93
5.1 Electron Beam...93
5.1.1 E-Beam Exposure Process 94
5.1.2 Fabrication and Metrology..98
5.1.3 DC Characteristics 101
5.2 Engineering Effective Barrier Height of Multi-Tunnel-Layer MIM Diodes............108
5.2.1 Pt-Al_2O_3-Ti and Pt-HfO_2-Ti MIM Diode 109
5.2.2 Pt-Al_2O_3-TiO_2-Ti MIIM Diode..110
5.2.3 Pt-Al_2O_3-HfO_2- TiO_2-Ti MIIIM Diode...111
5.3 Summary 112

CHAPTER 6: MIM DIODE RF CHARACTERIZATION 114
6.1 Device Characterization...115
6.1.1 Schottky Diode Characterization 115
6.1.2 MIM Tunneling Diode Characterization 117
6.1.3 MIM Diode Equivalent Circuit Model 118
6.1.4 Measurement Setup...119
6.2 Rectification Performance of Diodes...128
6.3 Summary 134

CHAPTER 7: CONCLUDING REMARK AND FUTURE WORK 136
7.1 Conclusion 136
7.2 Contributions..138

7.3 Future Work 139

REFERENCES 140

APPENDICES 150
Appendix I Email Showing Permission to Use Figure 3.7 151
Appendix II Email Showing Permission to Use Figure 1.3 152
Appendix III Email Showing Permission to Use Figure 1.3(b), Figure 3.3, and Figure 3.4 153
Appendix IV Email Showing Permission to Use Figure 5.5, and Figure 5.6 154

LIST OF TABLES

Table 3.1: Summary of the characteristics of different material depositions used in micro and nano fabrication 54

Table 3.2: The comparison of metals properties showing the metal work function, the metal heat conductivity, electrical conductivity, melting point and bulk density 59

Table 3.3: Key properties of candidates materials considered for as plausible tunneling layer 63

Table 4.1: The definition of the key performance parameters for evaluating MIM diodes 71

Table 4.2: A summary of measured characteristics of Pt-HfO_2-Ti MIM diodes with 2nm-thick HfO_2 tunnel layer and different junction sizes ranging from 10µm×10µm to 30µm×30µm. 72

Table 4.3: A summary of measured characteristics of Pt-HfO_2-Ti MIM diodes with 3nm-thick HfO_2 tunnel layer and different junction sizes ranging from 10µm×10µm to 30µm×30µm 74

Table 4.4: A summary of measured characteristics of Pt-TiO_2-Ti MIM diodes with 3nm-thick TiO_2 tunnel layer and different junction sizes ranging from 10µm×10µm to 30µm×30µm. 76

Table 4.5: A summary of measured characteristics of Pt-TiO_2-Ti MIM diodes with 4nm-thick TiO_2 tunnel layer and different junction sizes ranging from 10µm×10µm to 30µm×30µm. 76

Table 4.6: Comparison of parameters extracted from the modeled to measured data 90

Table 4.7: Comparison between DC characteristics of MIM and MIIM diodes 92

Table 5.1: Description of the specific pattern preparation and pattern writing files used by JEOL 9300. 95

Table 6.1: Extracted lumped element values for the equivalent circuit for a Pt-Al_2O_3-HfO_2-TiO_2-Ti diode. 127

Table 6.2: Extracted lumped element values for the equivalent circuit for a Pt-Al_2O_3-TiO_2-Ti diode. 127

Table 6.3: Extracted lumped element values for the equivalent circuit for a Pt-HfO_2-Ti diode....127

Table 6.4: Extracted lumped element values for the equivalent circuit for a Pt- Al_2O_3-Ti diode....127

LIST OF FIGURES

Figure 1.1: Schematic diagram of a rectenna..3

Figure 1.2: Equivalent circuit model for antenna coupled diode 3

Figure 1.3: Electromagnetic spectrum showing the THz range..6

Figure 1.4: Simple schematic diagram of direct detector/receiver setup 8

Figure 1.5: The schematic diagram of indirect/heterodyne receiver setup 9

Figure 2.1: The representation of energy diagram of MIM junction with two dissimilar metal contacts on the opposite side of tunnel junction. 16

Figure 2.2: The applied potential representation of metal-insulator-metal diode under bias 18

Figure 2.3: Representation of energy band diagram showing the potential of multiple different stacks of tunnel layers..28

Figure 2.4: Energy band diagram showing the barrier between dissimilar electrodes at V≈0 31

Figure 2.5: The energy band diagram showing the barrier between dissimilar electrodes at the intermediate potential (V≤0≤φ/q) of the forward bias. 31

Figure 2.6: The energy band diagram showing the barrier between dissimilar electrodes under a forward-biased potential of V≥φ/q 32

Figure 2.7: The measured *I-V* plots of fabricated MIM diodes operated under the intermediate voltage range 33

Figure 3.1: (a) The resist-coated wafer exposure setup under a UV light 40

Figure 3.2: A schematic description of mask projection and photolithography's basic processing to establish metal pattern on a substrate...41

Figure 3.3: Ray diagram of the electron optical system of a round beam electron beam system..45

Figure 3.4: The Hitachi SU-70 analytical field emission SEM 46

Figure 3.5: JEOL JBX-9300FS electron beam lithography system. ...47

Figure 3.6: Generic block diagram for electron beam (E-beam) generation ...48

Figure 3.7: A complete one cycle schematic description of atomic layer deposition...52

Figure 3.8: The mask CAD design image. ...60

Figure 3.9: A top-view photo of the first layer photolithography mask plate ...61

Figure 3.10: Step-by-step illustration of four-mask UV photolithography fabrication process, including the deposition and patterning ...64

Figure 3.11: SEM images of the fabricated MIM diode device showing 50µm×50µm junction size...65

Figure 3.12: TEM cross-sectional image of MIM junction showing interfacial layers of TiO_2 in between Ti (top) and Pt (bottom) electrodes ...66

Figure 3.13: The metrology analysis of the fabricated device showing a TEM cross-sectional image of MIM junction showing the TiO_2 interfacial layer in between Ti (top) and Pt (bottom) electrodes ...67

Figure 3.14: The metrology analysis of the fabricated device showing an EDX spectrum verifying the composition of the (Pt-TiO_2-Ti) MIM tunnel junction. ...67

Figure 4.1: A simplified schematic illustration of DC characterization scheme with a HP4145B semiconductor parametric analyzer ...70

Figure 4.2: Measured DC *I*-*V* characteristics of Pt-HfO_2-Ti MIM diodes with 2nm-thick tunnel layer and different junction area...72

Figure 4.3: Measured DC *I*-*V* characteristics of Pt-HfO_2-Ti MIM diodes with 3nm-thick tunnel layer but different junction sizes ...73

Figure 4.4: Measured DC characteristics of Pt-TiO_2-Ti MIM diodes with 3nm-thick tunnel layer but different junction sizes ...75

Figure 4.5: Measured DC characteristics of Pt-TiO_2-Ti MIM diodes with 4nm-thick tunnel layer but different junction sizes ...77

Figure 4.6: (a) A schematic diagram of MIIM diode, (b) Energy band of a MIM diode having a cascaded barrier ...81

Figure 4.7: Measured DC characteristics of several Pt-HfO_2-TiO_2-Ti MIIM diodes with 20µm×20µm junction area composed of two stacked 1.5nm-thick tunnel layers ...83

Figure 4.8: Measured DC characteristics for several Pt-HfO_2-TiO_2-Ti MIIM diodes with 10μm×10μm junction areas composed of two stacked 1.5nm-thick tunnel layers 84

Figure 4.9: Measured DC characteristics for several Pt-HfO_2-TiO_2-Ti MIIM diodes with 5μm×5μm junction areas composed of two stacked 1.5nm-thick tunnel layers 85

Figure 4.10: Comparison of the measured DC characteristics of 15 Pt-HfO_2-TiO_2-Ti MIIM diodes with 20μm×20μm junction areas composed of two stacked 1.5nm-thick tunnel layers 86

Figure 4.11: Measured MIM diode results vs. modeled predicted *I-V* responses....89

Figure 5.1: Mask layout representation of different design of 200nmx200nm MIM diode 96

Figure 5.2: Top-view SEM image of a nano-fabricated MIM diode showing large coplanar pads patterned by regular UN lithography for measurement purposes....98

Figure 5.3: To characterize the surface morphology of the bottom electrode, the material roughness measurement was done using a atomic force microscopy (AFM) system....100

Figure 5.4: The SEM image of the cross-finger structure of the fabricated MIM diodes with nano-scale junctions 101

Figure 5.5: Measured DC characteristics of Pt-Al_2O_3-Ti MIM diodes with 3nm-thick tunnel layer of junction size of 200nm×200nm....102

Figure 5.6: Measured DC characteristics of Pt-HfO_2-Ti MIM diodes with 3nm-thick tunnel layer of junction sizes of 200nm×200nm 103

Figure 5.7: Measured DCIV characteristics of Pt-Al_2O_3-TiO_2-Ti MIM diodes with 1.5nm-thick constituent tunnel layers and junction sizes of 200nm×200nm....104

Figure 5.8: Measured DC characteristics of Pt-Al_2O_3-TiO_2-Ti MIM diodes with 1.5nm-thick constituent tunnel layers junction sizes of 200nm×200nm 105

Figure 5.9: Measured DC IV characteristics of Pt-Al_2O_3-HfO_2-TiO_2-Ti MIM diodes with 1.5nm-thick constituent tunnel layers for junction sizes of 200nm×200nm 106

Figure 5.10: Measured DC characteristics of Pt-Al_2O_3-HfO_2-TiO_2-Ti MIM diodes with 1.5nm-thick constituent the tunnels layers and junction sizes of 200nm×200nm....107

Figure 5.11: DC *I-V* characteristics of a Pt-Al_2O_3-TiO_2-Ti MIIM diode 113

Figure 6.1: The lumped-elements equivalent circuit model for a MIM tunneling diode 114

Figure 6.2: A measurement substrate showing device under test (DUT) with custom designed calibration microstrip lines 115

Figure 6.3: Equivalent circuit model used to represent RF behavior of Schottky diodes 116

Figure 6.4: S-parameter plot at different bias voltages for 0V, 0.1V and 0.3V..........................116

Figure 6.5: S-parameter plot at different bias voltages for -3V, 0.1V and 0.3V 117

Figure 6.6: Cross-sectional view schematic of a typical MIM diode structure 119

Figure 6.7: SEM image showing the structure of a nano-junction sized MIM diode in the CPW configuration for on wafer measurement..120

Figure 6.8: RF measurement setup with the device under test (DUT) connected to the VNA and the voltage source via a pair of bias Tees 121

Figure 6.9: For direct comparison between measured responses and the model predicted behavior, both the small-signal equivalent circuit model and the measured s2p data were jointly studied by ADS simulation 122

Figure 6.10: The optimization result for the Pt-Al_2O_3-HfO_2-TiO_2-Ti MIIIM diode showing the plots for the measured and modeled S-parameter responses at different bias voltages 123

Figure 6.11: The optimization result for the Pt-Al_2O_3-TiO_2-Ti MIIM diode showing the plots of the measured and modeled S-parameter response at different bias voltages...124

Figure 6.12: The optimization result for the Pt-HfO_2-Ti MIM diode showing the plots of the measured and modeled S-parameter response at different bias voltages 125

Figure 6.13: The optimization result for the Pt-Al_2O_3-Ti MIM diode showing the plots of the measured and modeled S-parameter response at different bias voltages 126

Figure 6.14: Measured *I-V* response vs. the 5th order polynomial fit used in SDD tool for a Pt-Al_2O_3-TiO_2-Ti MIIM diode 129

Figure 6.15: Schematic of the MIM diode detection implementation in ADS 130

Figure 6.16: The simulated characteristics of nano-scale MIIIM and MIIM diodes showing detected the output voltage versus the input power..................................131

Figure 6.17: The detected voltage characteristics of nano junction MIM diodes showing the output voltage versus source input power 132

Figure 6.18: Detector output voltage versus input power simulated with different video resistance and input resistance 133

ABSTRACT

Metal-Insulator-Metal (MIM), Metal-Insulator-Insulator-Metal (MIIM), and Metal-Insulator-Insulator-Insulator-Metal (MIIIM) quantum tunneling diodes have been designed, fabricated, and characterized. The key interest of this work was to develop tunneling diodes capable of operating and detecting THz radiation up to 30THz, which is well beyond the operation ranges of other semiconductor-based diodes.

Al_2O_3, HfO_2 and TiO_2 metal oxides were employed for studying the behavior of metal-insulator-metal (MIM) and metal-insulator-insulator-metal (MIIM) quantum tunneling diodes. Specifically, ultra-thin films of these oxides with varied thicknesses were deposited by atomic layer deposition (ALD) as the tunneling junction material that is sandwiched between platinum (Pt) and titanium (Ti) electrodes, with dissimilar work functions of 5.3 eV and 4.1 eV, respectively.

Due to the unique and well-controlled tunneling characteristic of the ALD ultra-thin films, reproducible MIM and MIIM diode devices have been developed. The DC characteristics of MIM and MIIM tunneling junctions with different junction areas and materials were investigated in this work. The effects of the different compositions and thicknesses of the tunneling layer on the diodes were studied systematically. Through the introduction of stacked dual tunneling layers, it is demonstrated that the MIIM and MIIIM diodes exhibited a high degree of asymmetry (large ratio between forward and reverse currents) and a strong nonlinearity

in their *I-V* characteristics. The characterization was performed on diodes with micro and nano-scale junction areas.

The MIM diodes reported herein exhibited lower junction resistances than those reported by prior works. Moreover, a study was conducted to numerically extract the average barrier heights by fitting the analytical model of the tunneling current to the measured *I-V* responses, which were evaluated with respect to the thickness of the constituent tunneling layer. RF characterization was performed on the MIM diodes up to 65GHz, and its junction impedance was extracted. A rigorous procedure was followed to extract the diode equivalent circuit model to obtain the intrinsic lumped element model parameters of the MIM diodes.

CHAPTER 1: INTRODUCTION

This research focuses on the development of zero-bias and DC-biased diodes with high responsivity for antenna-coupled detectors that are used in tightly packed 2D array formation for high frequency (terahertz THz) radiation detection. For the past few decades, a great deal of effort has been focused on the development of millimeter wave receivers [1-3]. Recently, there has been growing interest in the development of antennas with operating wavelength range between 1μm and 100μm. Despite the numerous potential applications, developments in this wavelength range have been largely unexplored due to the lack of affordable and convenient radiation sources and means of detection. However, advancements in laser and optics technologies in the mid-twentieth century have helped to address issues of radiation sources while the recent progress in semiconductor devices and nanofabrication technologies have been instrumental in building THz detectors [4].

Due to unique resistive switching behavior [5], Metal-Insulator-Metal (MIM) diode have sparked a great deal of interest since the 1960s. The earliest generation of MIM point-contact diodes were composed of an atomically sharp tungsten wire tip, placed in direct contact with a planar metal electrode that was coated with a thin layer of oxide [6, 7]. Despite the challenges of reproducing those point-contact devices, it has been envisioned that MIM diodes coupled with planar antennas to create rectennas would hold great promise for detecting and mixing high frequency signals up to the THz range [8-10]. Particularly in the areas where high frequency rectification is needed, MIM diodes are anticipated to outperform their counterparts with either hetero-junctions or Schottky junctions [11], which have a rather limited cutoff frequency

(<3THz) [10] due to their fast response time. Several prior work on MIM diodes are either directed toward their nonlinearity, or their characteristics when integrated with antenna to form rectenna [12, 13].

1.1 Background

A rectenna (e.g a tunneling diode-coupled antenna) concept, unlike the photovoltaic cell, utilizes the wave nature of electromagnetic radiation by collecting the longer wavelengths at the desired band [14, 15]. The device rectifies captured electromagnetic (EM) radiation and provides direct current (DC) electrical output. A typical rectenna system consists of two major elements, an antenna (slots, dipoles, spirals, and bow-tie) and a fast response tunneling diode. As shown in Fig.1.1, the alternating current (AC) signal collected by the antenna is channeled [16] through the diode where the rectification and mixing take place. It has been predicted that rectennas would not have the fundamental limitation of semiconductor band-gap, which constrains their conversion efficiencies [10, 17]. As a result, rectenna can be used in a variety of applications including harvesting solar energy [18, 19], chemical, and gas detection [20-22], medical imaging systems [23], non-volatile memory systems [24], and many other systems.

While the characteristics and performance of the individual components of the rectenna elements have been extensively studied theoretically and experimentally, it has remained a challenge to perfectly couple the antenna to the diode to realize optimum performance in term of responsivity, sensitivity and noise equivalent power [25]. For example, performance analysis of the tunnel junction diode have been thoroughly reported [9, 11, 26, 27], but the issue of accurately matching diodes to antennas has not been fully addressed. Some attempt have been made to tackle these problems, but most were based on using the antenna model to predict the operating frequencies [28-30]. However, in these prior efforts, the responsivity of the device is

measured without proper matching thus hindering a good agreement with the operation frequencies and performance characteristics.

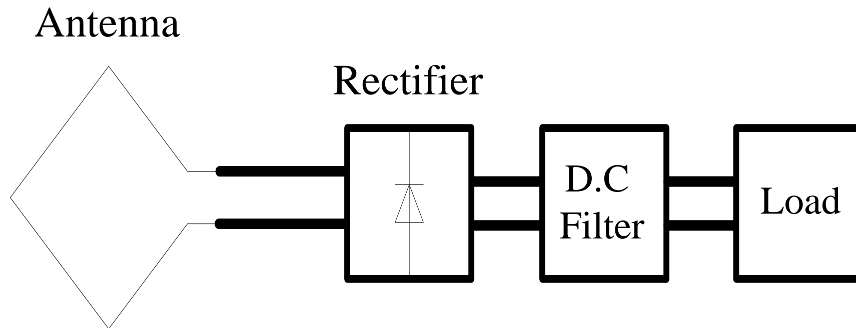

Figure 1.1**:** Schematic diagram of a rectenna. The system is formed by coupling a diode to an antenna to form a detector. The concept is that the antenna absorbs the AC radiation while the incorporated diode rectifies the AC signal to generate a DC output.

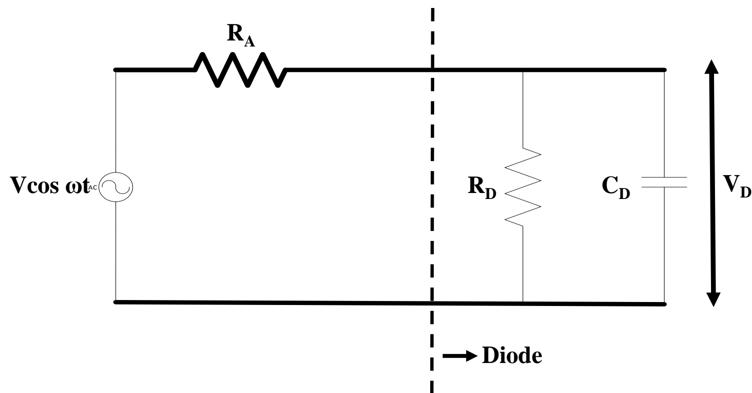

Figure 1.2: Equivalent circuit model for antenna coupled diode. R_A is the antenna impedance, R_D is the diode impedance, C_D is the diode capacitance and the V_D is the DC-bias voltage across the diode.

Fig.1.2 shows an equivalent circuit model of an antenna coupled with a tunneling diode. The antenna section of the system is represented by the voltage source $V\cos\omega t$ in series with internal resistance R_A representing the radiation resistance of the antenna. The nonlinear resistance (R_D) is the diode junction resistance in parallel with the diode shunt junction

capacitance (C_D) representing the behavior of the tunnel diode junction. The theory of impedance matching between the antenna to the diode was discussed by Sanchez [31] and Sarehraz [16]. In particular, Sanchez [31] examined the relationship between diode output voltage and the incident signal captured by the antenna, which is shown in the equations below:

$$V_D = \frac{VZ_D}{(R_A + Z_D)} \tag{1.1}$$

Z_D is the equivalent impedance of MIM diode calculated from the parallel R_D and C_D

$$Z_D = \frac{R_D}{(1 + j\omega C_D R_D)} \qquad 1.2)$$

Augeri [32] introduces the concept of additional voltage generator that represents the local oscillator LO for the heterodyne receiver analysis.

$$V = V_{LO} \cos \omega_{LO} t + V_S \cos \omega_S t \tag{1.3}$$

therefore

$$V_D = \frac{VR_D}{(R_A + R_D + j\omega R_A R_D C_D)} \tag{1.4}$$

where junction capacitance $C_D = \varepsilon_0 \varepsilon A/L$ is due to the finite contact area A and the dielectric layer thickness L, Z_D is the parallel combination of R_D with X_j introducing the concept of "reduced frequency" $q = \omega C_D R_A$, the "reduced diode resistance" $x = R_D/R_A$, and the "incident power" $P = V^2/8R_A$, then

$$V_D = \frac{Vx}{[1 + (1 + jq)x]} \tag{1.5}$$

Now the power dissipated in the shunt MIM diode resistance R_D is:

$$P_r = \frac{|V_D|^2}{R_D} = \frac{V^2 x^2}{R_D\left[(1+x)^2 + q^2 x^2\right]} \quad (1.6)$$

$$P_r = \frac{x^2}{R_D} \frac{V_{LO}{}^2 \cos^2 \omega_{LO} t + V_S^2 \cos^2 \omega_S t + 2V_{LO} V_S \cos \omega_{LO} t \cos \omega_S t}{\left[(1+x)^2 + q^2 x^2\right]} \quad (1.7)$$

$$P_r = \frac{x}{R_A} \frac{V_{LO}{}^2 \cos^2 \omega_{LO} t + V_S^2 \cos^2 \omega_S t + 2V_{LO} V_S \left[\cos(\omega_{LO} - \omega_S)t + \cos(\omega_S + \omega_{LO})t\right]}{\left[(1+x)^2 + q^2 x^2\right]} \quad (1.8)$$

Let

$$\frac{\left(V_{LO}{}^2 \cos^2 \omega_{LO} t + V_S^2 \cos^2 \omega_S t + 2V_{LO} V_S \left[\cos(\omega_{LO} - \omega_S)t + \cos(\omega_S + \omega_{LO})t\right]\right)}{R_A} = P \quad (1.9)$$

$$P_r = \frac{Px}{\left[(1+x)^2 + q^2 x^2\right]} \quad (1.10)$$

The condition to obtain the value of diode resistance that maximized P_r is $\partial P_r / \partial x = 0$. So at $q<1$, the maximum P_r takes place, i.e. $R_D = R_A$.

1.2 Terahertz Radiation

THz (10^{12} Hz) lies between the microwave and infrared regions of the frequency spectrum. The frequencies in this region can be expressed in different units. For example, a) Frequency (f) = 1THz; b) Angular frequency (ω) = $2\pi f$; c) Period (τ) = $1/f$; d) wavelength (λ) = c/f; e) Wave-number (κ) = $\kappa/2\pi$; f) Photon energy ($h\nu$) = $\hbar\omega$; and g) temperature (T) = hf/κ_B [33]. Fig.1.3 shows a detailed view of the position of the THz band on the electromagnetic spectrum.

Historically, generating and detecting radiation in the THz band has been difficult. Only weak and incoherent radiation has been successfully generated, and these required bulky and expensive equipment [34, 35]. Due to these difficulties, frequencies in this region were largely unexplored. Early advancement in laser and optics technologies in the mid-1960s has led to the

discovery of the far-infrared laser [36, 37], and the CO_2-pumped gas laser [38]. Production of these laser technologies has helped to eliminate the former problem (i.e. THz signal generation) while the progress in semiconductor devices and nanofabrication technologies have been instrumental for building terahertz detectors. Other THz radiation sources that are presently in use include photo-mixing [39], free electron laser (FEL) [40], synchrotron light [41], quantum cascade laser [42], and backward wave oscillator (BWO) [43]. Likewise, for the detection of THz radiation, a hybrid technology using ideas from both optical and microwave arenas have been employed that incorporates a quasi-optical collection system.

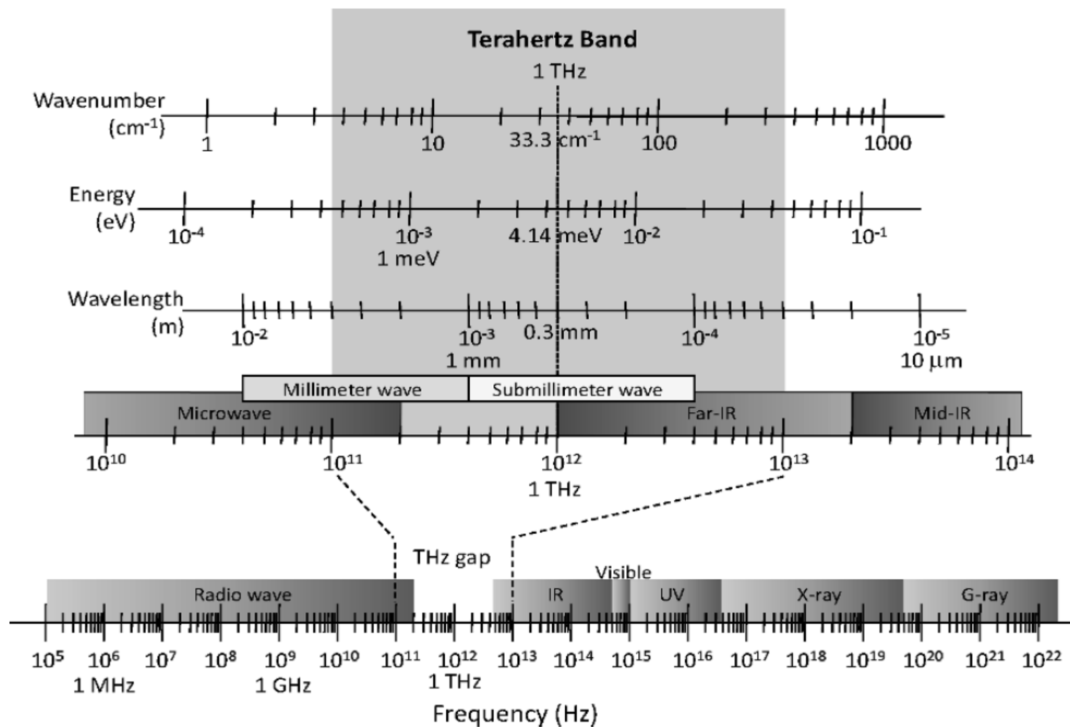

Figure 1.3: Electromagnetic spectrum showing the THz range [33]. The band within the region consists of millimeter wave (MMW): 1-10 mm, 30-300 GHz, 0.03-0.3THz; sub-millimeter wave (SMMW): 0.1-1 mm, 0.3-0.3 THz; and far infrared (FIR): (25-40) to (200-350) μm, (0.86-1.5) to (7.5-12) THz [33].

For the past few decades, a great deal of effort has been focused on the development of terahertz technology due to its increasing importance in a diverse range of human and societal activity. Due to its potential, many disciplines have been involved in the development of THz technologies. These include ultrafast spectroscopy [44], mobile communication [45], energy harvesting [46, 47], explosive substance detection [48], manufacturing [49], drugs [50], and bio-medical imaging [23], and so on.

1.2.1 Detection of THz Radiation

The detection of THz radiation can be classified as either coherent (heterodyne) detection or incoherent (direct) detection [51]. With the coherent detection arrangement, the phase and amplitude of the field is measured [52]. Comparatively, incoherent radiation detection measures only the intensity of the field. Thus, coherent detectors are preferred for detecting THz radiation where higher sensitivity and spectral resolution is required. In coherent techniques, key components of generation and detection mechanisms are closely associated due to the use of the same radiation source. Therefore, coherent schemes are more often associated with generation of THz radiation than that of detection.

Thermal sensors such as micro-bolometers [53], Golay cells [54], and pyroelectric devices [55] are traditionally used for detecting radiation in THz range. In addition, new propositions, based on the advancements in material engineering which explore different material principles and properties, have increased the option for THz radiation. Such innovation produces devices that include the carbon nanotube bolometer [56], hot electron room temperature bipolar semiconductor bolometers [57, 58], hetero-junction and homo-junction internal photoemission detectors [59, 60], the cold electron bolometer [61], the field effect

transistor (FETs) [62-65], quantum dots detectors (QDD) [66, 67], the Schottky diode with single walled nanotubes [68] and different antenna couple detectors [69-71], just to name a few.

In direct detection scheme, the detector detects signal radiation (P_{Signal}) and the background signal ($P_{Background}$). Signals collected by the optics were focused toward the detector, as shown in Fig. 1.4. The electrical signal from the detector is amplified to produce a signal that will be further processed [72]. One of the problems of this detection scheme is that its output signal has lots of distortion due to an inability to totally eliminate the background noise to mitigate its effect of the output. Also, the detected power is of high level due to the system device noise, circuit element and the amplifier. Examples of detector use for direct detection are the Golay cell, the pyroelectric detector, bolometers, microbolometers, and the hot electron InSb, Si, Ge bolometer [73].

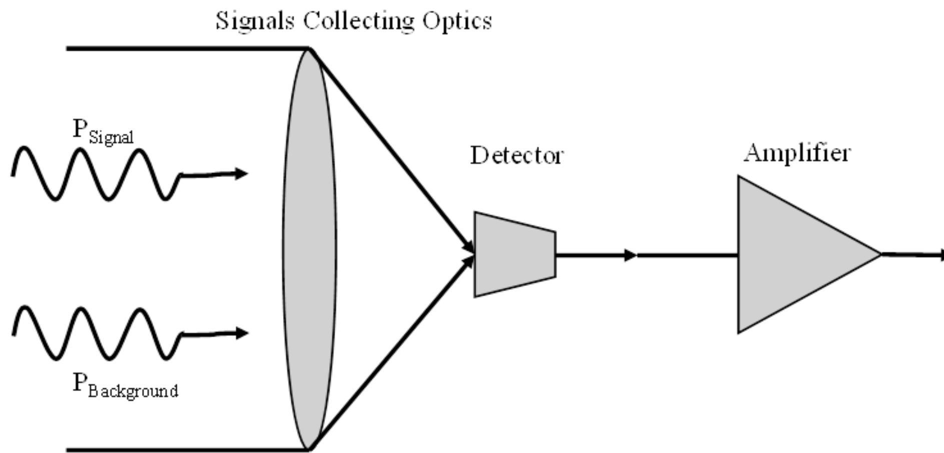

Figure 1.4: Simple schematic diagram of direct detector/receiver setup. The two signals are represented by P_{signal} and $P_{Background}$ for signal and background respectively.

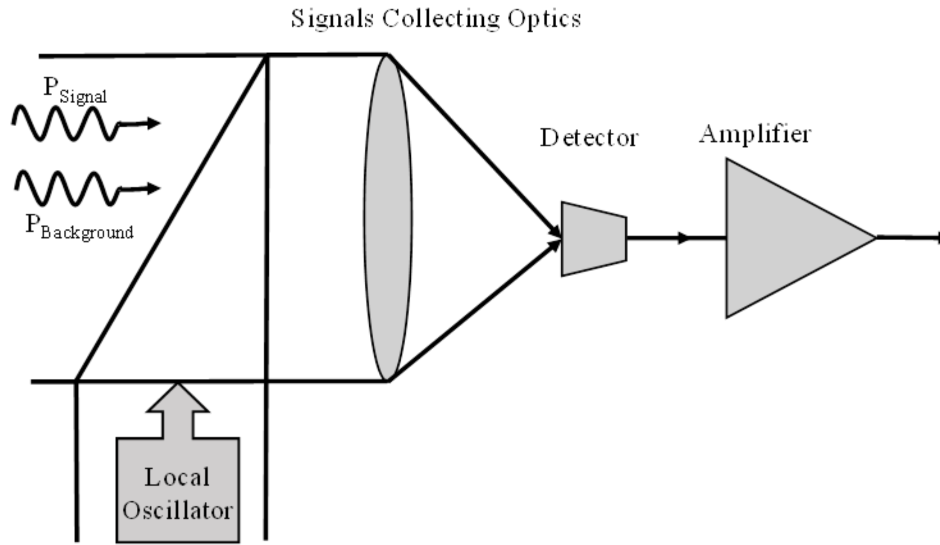

Figure 1.5: The schematic diagram of indirect/heterodyne receiver setup. It includes the local oscillator, mixer and diplexer. P_{signal} is the radiation signal power, $P_{Background}$ is the background radiation power

The heterodyne detector is the one in which the THz frequency signals are down-converted to an intermediate frequency using nonlinear devices [51, 72, 74]. Heterodyne detector achieves preservation of the amplitude and phase of the incident signal. The system is illustrated in Fig. 1.5. One of the key components of this system is the addition of the local oscillator to the signal and background radiant power, which provides the reference radiation power. Another enabling component of the heterodyne detector is the mixer with high nonlinearity for frequency translation.

The most commonly used mixers in heterodyne detector systems include Schottky diodes [75], semiconductors and superconducting HEBs, superlattices (SLs) and the superconductor-insulator-superconductor (SIS) tunneling diodes [76]. These devices have more advantages over other THz detectors, including: a) ability to detect the phase and modulation of the radiation frequency; b) higher spectral resolution ($v/\Delta v \sim 10^5$-10^6) due to intermediate frequency being

significantly lower than radiation signal frequency [77]; and c) the ability to discriminate against noise from background radiation [78].

1.3 Dissertation Overview

Metal-Insulator-Metal (MIM) diodes allow direct detection of THz radiation up to 30THz, which is well beyond the operation ranges of other semiconductor-based diodes. The overlap between top and bottom electrode contacts determines the active device area, while the thickness, quality, bandgap, electron affinity, dielectric constant, and conduction band offset of the ultra-thin barrier set the tunneling characteristics. In the MIM structured diode, a small deviation (in the range of angstrom) of barrier thickness can cause a significant change in the tunnel resistance, and *I-V* responses [79]. So far, most prior efforts have been based on traditional thin-film deposition processes such as thermal oxidation, plasma enhanced chemical vapor deposition (PECVD), sputtering and so on, which have insufficient control over the quality, uniformity and repeatability of the nanometer-thick tunneling layer. In the effort herein, atomic layer depositions (ALD) have been employed for formation of the metal oxide layer(s). Due to the nature of self-limiting surface reactions, atomic layer control of the film growth can be obtained as fine as ~0.1 Å with exceptional uniformity and repeatability. By reducing the thickness of the tunneling barrier while retaining its properties, a new class of MIM diodes is produced with a faster response time (i.e., higher cutoff frequency) due to the use of minimum contact area and ultra-thin tunneling layers.

Another issue that hinders the realization of the optimized responsivity for the antenna-coupled detectors is ascribed to the impedance mismatch between the antenna and the diode. In this work, the equivalent circuit model of the diode will be extracted to study the characteristic impedance of the MIM diode. Subsequently, the configuration and geometry of the antenna will

be designed based on the extracted diode impedance. The quantum tunneling mechanisms infer that the implementation of thinner tunneling barriers could be highly instrumental for the development of MIM diodes with reduced impedance and enhanced responsivity. In addition, the research explores strategic designs of antennas to match the impedance of the diode.

Several prior works [31, 42, 80-85] have suggested that for systems operating in the THz and infrared frequencies, metal-insulator-metal (MIM) (sometime referred to as metal-oxide-metal (MOM) or conductor-insulator-conductor (CIC)) tunneling diodes are anticipated to outperform hetero-junction diodes, with limited cutoff frequencies (<3THz) [86]. In addition, the MIM devices are well-suited for a wide range of applications such as homeland security, medical imaging, material characterization, and energy scavenging. The distinctive characteristics of THz detectors are amenable to address challenges by receiving and delievering THz radiation efficiently to the active part of the detector for processing while suppressing material losses at such high frequencies. Therefore, the efficiency of the detector can be improved by monolithically integrating it with an antenna while satisfying impedance matching, and quasi-optically coupling of THz radiation to the diode [87].

1.4 Goals

Antenna-coupled thin-film metal-insulator-metal diode devices have been extensively explored since the middle of the last century. The challenge of this device has been the inability to achieve the optimum rectification power output. This problem can be ascribed to lack of design strategies for the tunnel diode with well-tailored performance via impedance matching for maximum power transfer and low noise. When designing the antenna-coupled tunnel diodes, the quality, bandgap, electron affinity, dielectric constant, conduction band offset of the tunneling layer(s), as well as the work functions of the electrodes lead to a quantum well at their boundary,

thus resulting in coveted nonlinear and asymmetrical current-voltage (*I*-*V*) characteristics along with low zero-bias impedance. Hence, one of the goals of this work is to design and fabricate the nano-scale zero-bias MIM and MIIM tunneling diodes for high-responsivity antenna-coupled detectors. Another goal is to extract the intrinsic impedance of the MIM and MIIM diode.

1.5 Research Objectives

The objective of this research is to obtain maximum responsivity for antenna-coupled metal-insulator-insulator-metal (MIIM) detectors by exploiting the impedance matching between the antenna and the diode for THz imaging and energy scavenging application. The specific objectives include the following:

- Development of a new class of thin-film MIIM diodes with greatly improved responsivity by employing stacked, multiple-layer tunnel junction deposited by the atomic layer deposition with strategically-designed junction area, thickness and carefully-chosen insulator and metal materials to strengthen nonlinearity and asymmetry of the *I*-*V* response.
- Perform DC *I*-*V* characterization to measure the key figure of merits of the MIM and MIIM diode and its predicts performance in mixing high frequencies.
- Development of the MIM diode parameter extraction procedure to predict the potential barrier height in relation to the thickness of the tunnel layer.
- Characterize the newly developed thin-film MIIM diodes using on-wafer RF probing measurements up to 65GHz and extract equivalent circuit models.

1.6 Dissertation Organization

- Chapter 2: Electron tunneling devices analysis – In this chapter, the review of electron tunneling devices is presented. In particular, the theory of operation of metal-insulator-metal (MIM), metal-insulator-insulator-metal (MIIM) and metal-insulator-insulator-insulator-metal (MIIIM) diodes as electron tunneling devices are elucidated in detail. This will include rectification and mixing mechanism, electron tunneling, thermionic emission, spreading resistance and RC time constant of MIM diode. Additionally, this chapter includes an explanation of the key performance parameters of the MIM diode vis-a-vis *I-V*, asymmetry, nonlinearity characteristics, differential resistance, and responsivity.
- Chapter 3: Fabrication processes and techniques– This chapter focuses on the design and fabrication techniques of MIM diodes. The techniques for manufacturing small (micrometer and nanometer) scale MIM diodes will be discussed. This will include discussion about the process of the optical lithography and electron beam (E-beam) lithography. Furthermore, this chapter will discuss thin film deposition technology of metals and insulators. It will include electron beam (E-beam) evaporation, thermal evaporation and sputtering of metal, while atomic layer deposition (ALD) for metal oxide deposition will also be discussed. This chapter will also include discussion of material-etching chemistry and metal liftoff process.
- Chapter 4: Micro-junction device fabrication, metrology and DC characterization – This chapter will detail the steps taken to fabricate the device. The chapter will also include the metrological analysis of the fabricated devices. In addition, the DC characterization performance of the devices will be discussed, including presentation and comparisons of

current-voltage (*I*-*V*), nonlinearity, differential resistance, responsivity, and asymmetry characteristics of MIM, MIIM and MIIIM.

- Chapter 5: Nano-device fabrication, metrology and DC characterization – This chapter will detail the steps taken to fabricate the nano-devices. Also, the DC characterization performance of the devices will be discussed, including presentation and comparisons of current-voltage (*I*-*V*), nonlinearity, differential resistance, responsivity, and asymmetry characteristics of MIM, MIIM and MIIIM.
- Chapter 6: RF characterization and parameter extraction – This chapter will detail the processes undertaken to improve the fitting of the measured data to the equivalent circuit model of the diode. These studies are aimed toward extraction of the characteristic impedance of MIM/MIIM/MIIIM diodes.
- Chapter 7: Conclusion and future work.

CHAPTER 2: THEORETICAL ANALYSIS OF MIM TUNNELING DIODES

2.1 MIM Tunneling Diode Model

Metal-insulator-metal diode is a quantum mechanical tunnel junction device used mainly as a mixer in THz radiation receivers. The MIM diode has two electrodes separated by a thin film insulating layer. Current bypasses the potential barrier which is normally inhibited by the tunnel junction layer [76, 88]. It is a nonlinear resistance device. The nonlinearity is produced by single electron particle energy travelling through the tunnel barrier. Therefore, MIM diode performance is a factor of the thickness of the tunnel layer. Based on the work function of the electrodes, the device can be symmetric or asymmetric. If the electrodes on the sides of the insulating layer are identical, the potential barrier behaves in symmetric fashion; however, if the electrodes are dissimilar, the potential barrier is asymmetrical.

In this chapter, the theoretical operation of MIM tunneling diode is described in detail. The initial studies on MIM diodes were done with the employment of identical top/bottom electrodes [89]. In such studies, the junction current-voltage response is independent of the polarity of the applied voltage. In the later studies on the topic, analysis of devices with dissimilar electrodes [88, 90] was introduced. The DC *I-V* characteristics of MIM diodes with dissimilar electrodes of different work functions suggested that the potential polarity of applied voltage play a major role in the behavior of the device. For MIM diodes with dissimilar electrodes [88, 91], the generalized expressions found that the *I-V* characteristics of the junction is a factor of the applied voltage. Due to potential difference between the metal contacts of

dissimilar work function, an intrinsic field developed within the insulator. Fig. 2.1 describes the energy band diagram of an MIM diode with dissimilar electrodes. The η, ψ_1 and ψ_2 symbolize the diode Fermi level, electrode1 work function, and electrode2 work function, respectively. The overlap metals electrodes with the insulator layer(s) sandwiched between them form a junction capacitance C_D in parallel with nonlinear voltage dependent resistance R_D [92]. In essence, the junction area, the thickness of the tunnel layer, the junction chemical and physical material composition contributes to the behavior of the MIM tunneling diode. For example, the DC analysis of the asymmetry (η), curvature coefficient (γ), and the degree of non-linearity (χ) calculated from the *I-V* characteristics determine the efficiency of the diode [9, 11, 26, 27, 93].

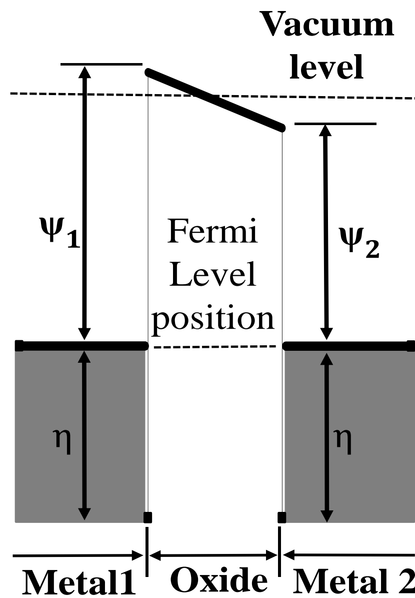

Figure 2.1: The representation of energy diagram of MIM junction with two dissimilar metal contacts on the opposite side of tunnel junction.

As two metal electrodes are separated by an ultra-thin insulating layer to form a MIM diode, and electrical conduction takes place between the two metal electrodes when a voltage is

applied. This is due to electron tunneling via the barrier [9, 11]. The current-voltage (*I-V*) characteristics are calculated from the current density (J) with respect to the applied voltage by integrating the distribution of electrons with all possible energy [31, 88]. The trapezoidal potential within the tunnel layer bounded by two metal contacts is used to calculate the tunnel current through the insulator [32, 85, 88]. The shunt resistance and capacitance of the equivalent circuit for a MIM diode are key factors that affect its cutoff frequency, which depends primarily on the oxide thickness and junction area [32, 91]. In simple terms, the performance of a MIM diode with regard to its responsivity and its cutoff frequency is determined by the asymmetry of its *I-V* characteristics controlled by the oxide thickness, contact area, and barrier height [79, 85].

In a metal-insulator-metal (MIM) tunnel diode, electrons from one metal tunnel through the insulator film and are collected by another metal at the other side of the insulator. In this device arrangement, the sufficient charge is transferred from the interior of the electrodes in either direction, depending on the polarity of the excitation voltage, to give rise to any effective changes in the band. As a result, it displays nonlinear *I-V* characteristics without the presence of negative resistance. Fig. 2.1 illustrates an energy band structure of two metal contacts on an insulator. With the case of two identical electrodes shown in Fig. 2.2(b), the lower part of the insulator conduction band is uniformly flat throughout the whole length. On the contrary, Fig 2.2(c) due to dissimilar electrodes bonded to the surface of the insulator, the interfacial barrier potential differ in energy is given by:

$$(\psi_R - \chi) - (\psi_L - \chi) = \psi_R - \psi_L \tag{2.1}$$

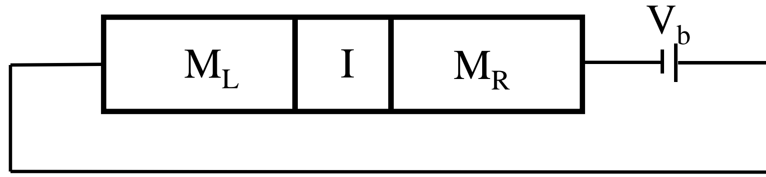

(a)

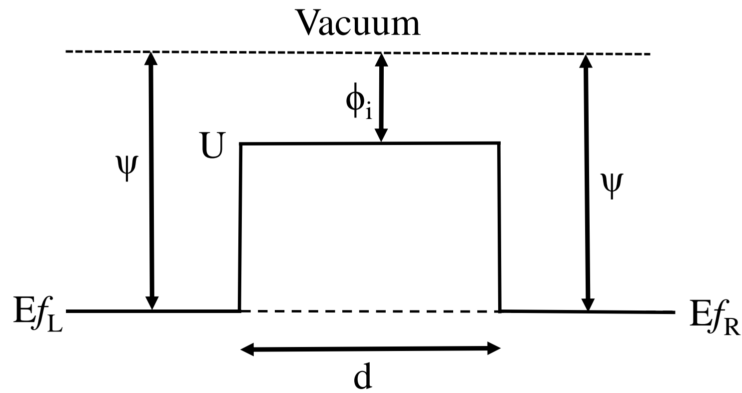

(b)

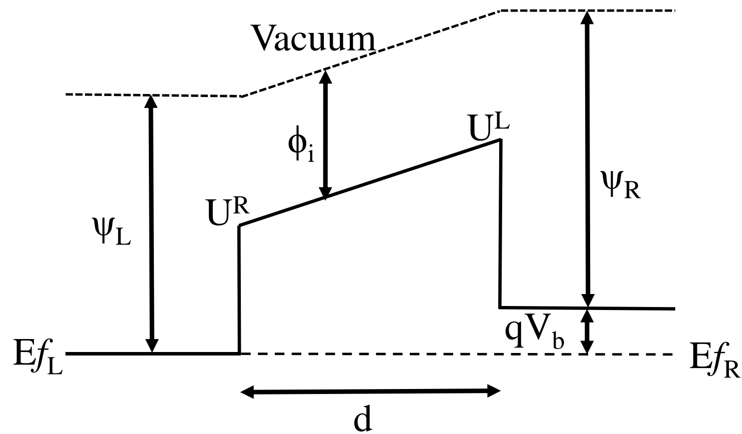

(c)

Figure 2.2: The applied potential representation of metal-insulator-metal diode under bias. d is the tunnel layer thickness, U is the barrier height, V_b is the bias voltage, E_f is the Fermi level, ϕ is the electron affinity, ψ is the metal work function (a) shows the physical structure of the diode with V_b as bias; (b) shows the band diagram when $V_b=0$ for the similar electrode; (c) shows the band diagram when V_b=0 for the similar electrode.

where χ is the electron affinity of the insulator, ψ_R and ψ_L are the work function of right and left metals, respectively. The device's intrinsic electric field magnitude [76, 88] is expressed in Eq. 2.2

$$F_i = \frac{\psi_R - \psi_L}{qd} \tag{2.2}$$

where q is the charge of electrons and d is the thickness of insulating thin film.

The electron tunnel current density flowing across metal electrodes separated by thin film barrier is expressed as [26, 55, 94, 95]:

$$J(V_B) = J_{L-R} - J_{R-L} \tag{2.3}$$

As stated previously, MIM diode consists of an ultra-thin insulating layer sandwiched between two metal electrodes. Electrical conduction takes place between the two electrodes when an electron in the electrode gains enough thermal energy to penetrate the potential barrier of the ultra-thin insulating layer. This can be ascribed to an electron tunneling through the barrier [26, 95]. The predicted current-voltage (*I-V*) characteristics are determined from the current density (*J*) with respect to the applied bias voltage. In theory, the distribution of electrons with respect to energy is integrated in the conduction region [31, 88]. Among the conditions for tunneling in this region is the thickness of the barrier that should be less than 10nm. Electrons tunneling from metal 1 (M_L) to metal 2 (M_R) will generate current from M_R to M_L, as a result of the polarity of the applied potential. Similarly, current will flow from M_L to M_R when a free electron tunnels from M_R to M_L. The current density in the directions is expressed as J_{L-R} and J_{R-L}. The current density from one electrode to another is calculated as:

$$J_{L-R} = \frac{4\pi m_L^2 q}{h^3} \int_0^{E_m} T(E_x) \int_0^{\infty} f_L(E)\, dE\, dE_x \tag{2.4}$$

$$J_{R-L} = \frac{4\pi m_R^2 q}{h^3} \int_0^{E_m} T(E_x) \int_0^{\infty} f_R(E + qV_B) dE dE_x \tag{2.5}$$

therefore

$$J(V_B) = \frac{4\pi m_0^2 q}{h^3} \int_0^{E_m} T(E_x) dE_x \int_0^{\infty} \{ f_L(E) - f_R(E + qV_B) \} dE \tag{2.6}$$

where m is the mass of electron, E is the total energy, E_x is the transverse of energy of a tunneling electron and $T(E_x)$ is the transmission probability through the insulator. The q, h, f_L and f_R represents the electron charge, Planck's constant, left and right Fermi distribution, respectively. The left Fermi distribution is expressed as:

$$f_L(E) = \frac{1}{1 + \exp(\frac{E - E_{FL}}{kT})} \tag{2.7}$$

and right Fermi distribution as

$$f_R(E + qV_B) = \frac{1}{1 + \exp(\frac{E - (E_{FL} - qV_B}{kT})} \tag{2.8}$$

V_B is the voltage difference between the left metal electrode and right metal electrode.

A direct transition of electron through the tunnel layer of the MIM diode is a result of sufficient electric field between the two electrodes on the order of 10^6 V/cm [55]. Due to this effect, a finite tunneling probability occurs [96]. Schrödinger's equation is an approximation of the one electron problem usually employed in solving a one band structure. The analysis can be simply described as a free charge particle q moving in the x direction which inclines into a uniform electric field E_i. So, the electrostatic force $F = qE_i$ acts on this particle, which creates a potential energy $U = -Fx$. To solve for the tunneling probability, the wave-function ψ is determined from the equation [97].

$$\frac{\hbar^2}{2m}\nabla^2 + U(x)\psi(x) = E_x\psi(x) \tag{2.9}$$

where E is the particle total energy.

Wentzel-Kramers-Brillouin (WKB) [98, 99] approximation has been employed to calculate the probability of electron tunneling through forbidden barriers. The limitation with WKB is that it tends to overestimate the tunneling current [26], because the approximation does not take into account effects if the interface(s) on the wave function [95]. So the result will exclude reflection between layers. Another approach that has been employed to estimate the full quantum-mechanical tunneling probability is Green's function formalism [100, 101]. It takes into account the interface wave function reflection and attenuation on the electrical potential barrier. This method involves rigorous quantum simulation techniques. The other methods include the use of the transfer matrix method (TMM) [102], and the quantum transmitting boundary method (QTBM) [103-106]. Both TMM and QTBM solutions are very similar. This study compares the TMM and WKB solutions of MIM diode's tunneling current.

2.1.1 Analysis of TMM Formulation

The solutions of the Schrödinger equation will be solved for both left and right of the tunneling interfaces (as shown in Fig.2.1(c).

- $\Psi_L = q\phi_L$ – Work function of the left metal
- $\Psi_R = q\phi_R$ – Work function of the right metal
- χ – Electron affinity of the thin film barrier
- U_L – Potential of the right metal interface
- U_R – Potential of the left metal interface
- V_b – Applied bias voltage

- X_L – Left interface position
- X_R – Right interface position
- d- Barrier thickness

The tunneling equation can be solved as follow by takin the time independent 1D Schrödinger equation:

$$\frac{\hbar^2}{2m}\frac{d^2\psi(x)}{dx^2}+U(x)\psi(x)=E_x\psi(x) \tag{2.10}$$

$$\frac{\hbar^2}{2m}\frac{d^2\psi(x)}{dx^2}+\left[U(x)-E_x\right]\psi(x)=0$$

Multiplying both sides by $2m/\hbar^2$

$$\frac{d^2\psi(x)}{dx^2}+\frac{2m}{\hbar^2}\left[U(x)-E_x\right]\psi(x)=0 \tag{2.11}$$

Let

$$U(x)=0 \quad ; x<X_L \tag{2.12}$$

$$U(x)=\frac{U_l-U_{Rl}}{X_R-X_L}(x-X_L)+U_R \quad ; X_L<x<X_R \tag{2.13}$$

$$U(x)=qV_b \quad ; x>X_R \tag{2.14}$$

Substituting Eq. 2.12 into Eq. 2.11

$$\frac{d^2\psi(x)}{dx^2}\psi(x)+\frac{2m}{\hbar^2}E_x\psi(x)=0 \tag{2.15}$$

if

$$K^2{}_L=\frac{2m}{\hbar^2}E_x \Rightarrow K_L=\sqrt{\frac{2m}{\hbar^2}E_x} \tag{2.16}$$

Therefore, Eq.2.15 becomes a Helmholtz equation form

$$\frac{d^2\psi(x)}{dx^2}\psi(x) + K_L^2\psi(x) = 0 \tag{2.17}$$

The solution for Eq. 2.17 is

$$\psi_L(x) = A_L e^{ik_L x} + B_L e^{-ik_L x} \quad ; \text{x<X}_\text{L}\text{, U(x) =0} \tag{2.18}$$

and for the right electrode:

$$\psi_R(x) = C_R e^{ik_R x} + D_R e^{-ik_R x} \quad ; \text{x<X}_\text{R}\text{, U(x) =qV}_\text{b} \tag{2.19}$$

and

$$k_L = \sqrt{\frac{2m_L E_x}{\hbar^2}} \tag{2.20}$$

$$k_R = \sqrt{\frac{2m_R(E_x + qV_b)}{\hbar^2}} \tag{2.21}$$

Substituting Eq. 2.13 into eq. 2.11

$$\frac{d^2\psi(x)}{dx^2} - \frac{2m}{\hbar^2}\left[E_x - \frac{U_L - U_R}{X_R - X_L}(x - X_L) + U_L\right]\psi(x) = 0 \tag{2.22}$$

By separating the constant and x dependent variables, Eq. 2.22 is simplified to

$$\frac{d^2\psi(x)}{dx^2} - \frac{2m}{\hbar^2}\left[\underbrace{U_L - E_x - \frac{U_L - U_R}{X_R - X_L}X_L}_{E_j} + \underbrace{\frac{U_L - U_R}{X_R - X_L}x}_{F_j}\right]\psi(x) = 0 \tag{2.23}$$

Now we have the Schrödinger equation in

$$\frac{d^2\psi(x)}{dx^2} - \frac{2m}{\hbar^2}\left[E_j + F_j\right]\psi(x) = 0 \tag{2.24}$$

Applying a change of variable u_j (j = number of the tunnel layer)

$$u_j = \left(x + \frac{E_j}{F_j} \right) \left(\frac{2mF_j}{\hbar^2} \right)^{\frac{1}{3}} \tag{2.25}$$

$$\Rightarrow \quad F_j = \frac{U_L - U_R}{X_R - X_L} \quad and \quad E_j = U_L - E_x - F_j X_L$$

then

$$u_j = \left(x + \frac{U_R - E_x - F_j X_L}{F_j} \right) \left(\frac{2mF_j}{\hbar^2} \right)^{\frac{1}{3}} = \left[\frac{U_R - E_x}{F_j} + (x - X_L) \right] \underbrace{\left[\frac{2mF_j}{\hbar^2} \right]^{\frac{1}{3}}}_{u'} \tag{2.26}$$

The Schrodinger equation is reduced to

$$\frac{d^2\psi(x)}{dx^2} - u_j \psi(x) = 0 \tag{2.27}$$

Expression for the wave function within the tunnel layer of the Eq. 2.27 is converted to Airy function

$$\psi(u_j) = A_j A_i(u_j) + B_j B_i(u_j)$$

For a single tunnel layer

$$\psi(x) = AA_i(u) + BB_i(u) \tag{2.28}$$

where A_i and B_i are the homogenous Airy functions. The potential difference across the insulator layer is,

$$V(x) = (V_b + \phi_L - \phi_R - V_b) \tag{2.29}$$

Deriving the boundary condition at first boundary interface of single layer $x=X_L$:

$\psi_L(\mathrm{X_L}) = \psi_j(\mathrm{X_L})$, Continuity at interface

$$\frac{d\psi_L(X_L)}{dx} = \frac{d\psi_1(X_L)}{dx} \text{, Continuity of derivative at interface} \quad (2.30)$$

$$A_L e^{jk_L x} + B_L e^{-jk_L x} = A_j A_i(u_j(X_L)) + B_j B_i(u_j(X_L)) \quad (2.31)$$

Deriving the boundary condition at secondary boundary interface of single layer $x=X_R$:

$$\psi(x = X_R) = \psi_R(x = X_R) \text{, Continuity at interface}$$

$$\frac{d\psi_j(\mathrm{X_R})}{dx} = \frac{d\psi_R(\mathrm{X_R})}{dx} \text{, Continuity of derivative at interface} \quad (2.29)$$

$$A_j A_i(u(X_R)) + B_j B_i(u(X_R)) = A_R e^{jk_R X_R} + B_R e^{-jk_R X_R} \quad (2.30)$$

$$A_j u_1' A_i'(u(X_L)) + B_j u_1' B_i'(u(X_L)) = Cjk_R e^{jk_R X_L} - Djk_R e^{-jk_R X_L} \quad (2.31)$$

Having Eq. 2.34 and 2.35 in matrix form

$$\begin{bmatrix} A_L e^{jK_L X_L} & B_L e^{-jK_L X_L} \\ A_L jk_L e^{jK_L X_L} & -B_L jk_L e^{-jK_L X_L} \end{bmatrix} = \begin{bmatrix} A_j A_i(u(X_L)) + B_j B(u(X_L)) \\ A_j u' A_i'(u(X_L)) + B_j u' B_i(u(X_L)) \end{bmatrix} \quad (2.35)$$

Re-written Eq. 2.36

$$\begin{bmatrix} 1 & 1 \\ jk_L & -jk_L \end{bmatrix} \begin{bmatrix} A_L e^{jK_L X_L} \\ B_L e^{-jK_L X_L} \end{bmatrix} = \begin{bmatrix} A_j A_i(u(X_L)) + B_j B(u(X_L)) \\ A_j u' A_i'(u(X_L)) + B_j u' B_i(u(X_L)) \end{bmatrix} \begin{bmatrix} A_j \\ B_j \end{bmatrix} \quad (2.36)$$

$$u(x = X_L) = u^-; and$$
$$u(x = X_R) = u^+$$

Solving to isolate transmission and reflection coefficients, the inverse for the $\begin{bmatrix} 1 & 1 \\ jk_L & -jk_L \end{bmatrix}$ can be multiplied on both sides, which is given by

$$\begin{bmatrix} 1 & 1 \\ jk_L & -jk_L \end{bmatrix}^{-1} \begin{bmatrix} 1 & 1 \\ jk_L & -jk_L \end{bmatrix} \begin{bmatrix} A_L e^{jK_L X_L} \\ B_L e^{-jK_L X_L} \end{bmatrix} = \begin{bmatrix} 1 & 1 \\ jk_L & -jk_L \end{bmatrix}^{-1} \begin{bmatrix} A_j A_i(u^-) + B_j B(u^-) \\ A_j u' A_i'(u^-) + B_j u' B_i(u^-) \end{bmatrix} \begin{bmatrix} A_j \\ B_j \end{bmatrix} \quad (2.37)$$

$$\begin{bmatrix} A_L e^{jK_L X_L} \\ B_L e^{-jK_L X_L} \end{bmatrix} = \begin{bmatrix} 1 & 1 \\ jk_L & -jk_L \end{bmatrix}^{-1} \begin{bmatrix} A_j A_i(u^-) + B_j B(u^-) \\ A_j u' A_i'(u^-) + B_j u' B_i(u^-) \end{bmatrix} \begin{bmatrix} A_j \\ B_j \end{bmatrix} \tag{2.38}$$

The inverse of

$$\begin{bmatrix} 1 & 1 \\ jk_L & -jk_L \end{bmatrix}^{-1} = \frac{1}{\det} \begin{bmatrix} jk_L & -1 \\ -jk_L & 1 \end{bmatrix} = \frac{1}{-2jk_L} \begin{bmatrix} -jk_L & -1 \\ -jk_L & 1 \end{bmatrix} = \frac{1}{2} \begin{bmatrix} 1 & \frac{1}{jk_L} \\ 1 & \frac{1}{-jk_L} \end{bmatrix} \tag{2.39}$$

So substituting Eq.2.38 into Eq. 2.39

$$\begin{bmatrix} A_L e^{jK_L X_L} \\ B_L e^{-jK_L X_L} \end{bmatrix} = \frac{1}{2} \left[\underbrace{\begin{matrix} 1 & \frac{1}{jk_L} \\ 1 & \frac{1}{-jk_L} \end{matrix}}_{\bar{I}_1} \right] \left[\underbrace{\begin{matrix} A_j A_i(u^-) + B_j B(u^-) \\ A_j u' A_i'(u^-) + B_j u' B_i(u^-) \end{matrix}}_{\bar{M}_j} \right] \begin{bmatrix} A_j \\ B_j \end{bmatrix} \tag{2.40}$$

At the second boundary, using the Eq. 2.31 defined earlier and simplifying Eq. 2.35

$$\frac{d\psi_j(\mathrm{X_R})}{dx} = \frac{d\psi_R(\mathrm{X_R})}{dx} \tag{2.41}$$

$$A_j u_1' A_i'(u(X_L)) + B_j u_1' B_i'(u(X_L)) = Cjk_R e^{jk_R X_R} - Djk_R e^{-jk_R X_R}$$

Having them in the matrix form,

$$\begin{bmatrix} A_j A_i(u^+) & B_j B_i(u^+) \\ -u' A_j A_i'(u^+) & -u' B_j B_i'(u^+) \end{bmatrix} = \begin{bmatrix} Ce^{jk_R X_R} & De^{-jk_R X_R} \\ jk_R Ce^{jk_R X_R} & -jk_R De^{-jk_R X_R} \end{bmatrix} \tag{2.42}$$

$\Rightarrow$

$$\begin{bmatrix} A_i(u^+) & B_i(u^+) \\ -u' A_i'(u^+) & -u' B_i'(u^+) \end{bmatrix} \begin{bmatrix} A_j \\ B_j \end{bmatrix} = \begin{bmatrix} 1 & 1 \\ jk_R & -jk_R \end{bmatrix} \begin{bmatrix} Ce^{jk_R X_R} \\ De^{-jk_R X_R} \end{bmatrix} \tag{2.43}$$

Isolating the barrier coefficient

$$\begin{bmatrix} A_i(u^+) & B_i(u^+) \\ -u'A_i'(u^+) & -u'B_i'(u^+) \end{bmatrix}^{-1} \begin{bmatrix} A_i(u^+) & B_i(u^+) \\ -u'A_i'(u^+) & -u'B_i'(u^+) \end{bmatrix} \begin{bmatrix} A_j \\ B_j \end{bmatrix} = \begin{bmatrix} A_i(u^+) & B_i(u^+) \\ -u'A_i'(u^+) & -u'B_i'(u^+) \end{bmatrix}^{-1} \begin{bmatrix} 1 & 1 \\ jk_R & -jk_R \end{bmatrix} \begin{bmatrix} Ce^{jk_R X_R} \\ De^{-jk_R X_R} \end{bmatrix}$$

$$\begin{bmatrix} A_j \\ B_j \end{bmatrix} = \begin{bmatrix} A_i(u^+) & B_i(u^+) \\ -u'A_i'(u^+) & -u'B_i'(u^+) \end{bmatrix}^{-1} \begin{bmatrix} 1 & 1 \\ jk_R & -jk_R \end{bmatrix} \begin{bmatrix} Ce^{jk_R X_R} \\ De^{-jk_R X_R} \end{bmatrix} \tag{2.44}$$

$$\begin{bmatrix} A_i(u^+) & B_i(u^+) \\ -u'A_i'(u^+) & -u'B_i'(u^+) \end{bmatrix}^{-1} = \frac{1}{\det} \begin{bmatrix} u'B_i'(u^+) & -B_i(u^+) \\ -u'A_i'(u^+) & A_i(u^+) \end{bmatrix}$$

$$\det = A_i(u^+) \times u'B_i'(u^+) - B_i(u^+) \times u'A_i'(u^+) = u'\left[A_i(u^+)B_i'(u^+) - B_i(u^+)A_i'(u^+)\right]$$

Using the Wronskian relationship [97]

$$\left[A_i(u^+)B_i'(u^+) - B_i(u^+)A_i'(u^+)\right] = \frac{1}{\pi} \tag{2.45}$$

$$\det = u'\frac{1}{\pi}$$

Therefore,

$$\begin{bmatrix} A_i(u^+) & B_i(u^+) \\ -u'A_i'(u^+) & -u'B_i'(u^+) \end{bmatrix}^{-1} = \frac{\pi}{u'} \begin{bmatrix} u'B_i'(u^+) & -B_i(u^+) \\ -u'A_i'(u^+) & A_i(u^+) \end{bmatrix} = \pi \begin{bmatrix} B_i'(u^+) & -\dfrac{B_i(u^+)}{u'} \\ -A_i'(u^+) & \dfrac{A_i(u^+)}{u'} \end{bmatrix}$$

$$\begin{bmatrix} A_i(u^+) & B_i(u^+) \\ \dfrac{u'A_i'(u^+)}{m} & \dfrac{u'B_i'(u^+)}{m} \end{bmatrix}^{-1} = \left(\frac{u'}{\pi m}\right)^{-1} \begin{bmatrix} \dfrac{u'B_i'(u^+)}{m} & -B_i(u^+) \\ -\dfrac{u'A_i'(u^+)}{m} & A_i(u^+) \end{bmatrix} = \pi \begin{bmatrix} B_i'(u^+) & -\dfrac{mB_i(u^+)}{u'} \\ -A_i'(u^+) & \dfrac{mA_i(u^+)}{u'} \end{bmatrix} \tag{2.46}$$

$$\begin{bmatrix} A_j \\ B_j \end{bmatrix} = \pi \left[\underbrace{\begin{matrix} B_i'(u^+) & -\dfrac{mB_i(u^+)}{u'} \\ -A_i'(u^+) & \dfrac{mA_i(u^+)}{u'} \end{matrix}}_{\bar{N}_j} \right] \left[\underbrace{\begin{matrix} 1 & 1 \\ jk_R & -jk_R \end{matrix}}_{\bar{I}_2} \right] \begin{bmatrix} Ce^{jk_R X_R} \\ De^{-jk_R X_R} \end{bmatrix} \tag{2.47}$$

The full matrix is given by combination of the

$$\begin{bmatrix} A_L e^{jK_L X_L} \\ B_L e^{-jK_L X_L} \end{bmatrix} = \frac{1}{2} \begin{bmatrix} \underbrace{\begin{matrix} 1 & \frac{1}{jk_L} \\ 1 & \frac{1}{-jk_L} \end{matrix}}_{\bar{I}_1} \end{bmatrix} \begin{bmatrix} \underbrace{\begin{matrix} A_j A_i(u^-) + B_j B(u^-) \\ A_j u' A_i'(u^-) + B_j u' B_i(u^-) \end{matrix}}_{\bar{M}_j} \end{bmatrix} \pi \begin{bmatrix} \underbrace{\begin{matrix} B_i'(u^+) & -\frac{mB_i(u^+)}{u'} \\ -A_i'(u^+) & \frac{mA_i(u^+)}{u'} \end{matrix}}_{\bar{N}_j} \end{bmatrix} \begin{bmatrix} \underbrace{\begin{matrix} 1 & 1 \\ jk_R & -jk_R \end{matrix}}_{\bar{I}_2} \end{bmatrix} \begin{bmatrix} Ce^{jk_R X_R} \\ De^{-jk_R X_R} \end{bmatrix} \tag{2.48}$$

2.1.2 WKB Approximation

The WKB approximation of the tunneling probability for a barrier with thickness d for one band parabolic dispersion relation is given by [107, 108]:

$$T = \exp\left[-2\sqrt{\frac{2m}{\hbar^2}} \int_0^d \sqrt{U(x) - E} dx \right] \tag{2.49}$$

2.2 Multi Tunnel Layer MIM Diode

2.2.1 TMM Method

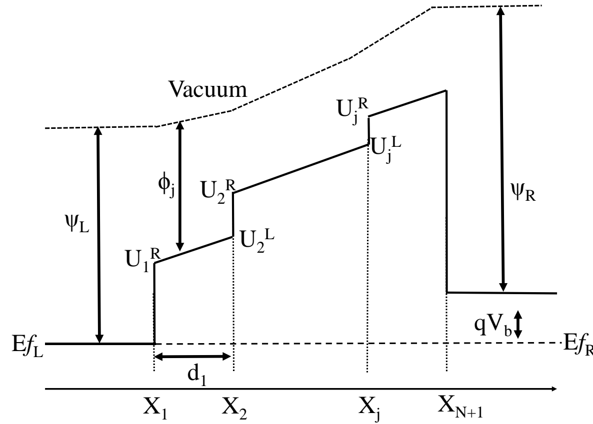

Figure 2.3: Representation of energy band diagram showing the potential of multiple different stacks of tunnel layers.

$$\psi_j(x) = A_j A_i(u_j) + B_j B_i(u_j)$$

The potential difference across the insulator layer is given by:

$$V_j(x) = \frac{d_j / \varepsilon_j}{\sum_{k=1}^{N} d_k / \varepsilon_k} \left(V_b + \phi_L - \phi_R\right) \tag{2.50}$$

2.2.2 WKB for Multi-tunnel Layer

$$T(E_x) = \exp\left[-\frac{2}{\hbar}\sum_{j=1}^{N}\int_{X_j}^{X_{j+1}}\sqrt{2m_j\left(E_x - U_j\right)}dx\right] \tag{2.51}$$

2.3 Characteristics of MIM Diode

This section discusses some important characteristics of MIM tunneling diode. Characteristics such as *I-V* response, junction resistance, junction capacitance, nonlinearity, asymmetry, rectification, mixing, and diode emission affect the performance of the MIM diode with respect to its responsivity and sensitivity. The electron affinity of the tunnel layer, metals work functions, thickness of the insulator and dielectric constant of the insulator are the major parameters that contribute to the changes in these characteristics.

2.3.1 Current –Voltage (*I-V*) Characteristics

For electrons to tunnel through the insulator from the opposite electrode, there is a need for sufficient thermal energy to propel across the potential barrier to the conduction band. The barrier must be thin enough to permit penetration by the electric tunnel effect. The electron tunneling equation was derived from the relationship between current density and voltage in a tunneling junction. Considering the asymmetric barrier, the current flow will be examined from both directions. Although electron tunneling through insulating barrier had been theoretical discussed in the previous section (2.1), the effect of different level of applied voltages will be

briefly discussed here. The voltages are categorized as low, intermediate, and high voltages. The value of these voltages is is quantified with respect to the mean barrier height.

When the current is flowing from electrode one to electrode two in the reverse direction, and for voltage range of $0 \leq V \leq \overline{\varphi}/e$, where $\overline{\varphi}$ is the mean barrier height given by [12, 31, 32, 76, 88, 94, 108]:

$$\overline{\varphi} = (\varphi_1 + \varphi_2 - qV)/2 \tag{2.52}$$

where φ_1 is the barrier height between the interface of the first metal electrode and the insulator and φ_2 is the barrier height at the interface of the second metal electrode and tunnel layer. The relationship between the barrier height and the work function is given as;

$$\varphi_2 = \varphi_1 + (\psi_2 - \psi_1) = \varphi_1 + \Delta\psi$$

if ψ_2 and ψ_1 are metal 2 and metal 1 work functions, respectively. A general expression for calculating tunneling current using the Sommerfeld and Beth model applied to WKB approximation is given by [76]

$$J = J_0 \left\{ \overline{\varphi} \exp\left(-A\overline{\varphi}^{0.5}\right) - (\overline{\varphi} + qV) \times \exp\left[-A(\overline{\varphi} + qV)^{0.5}\right] \right\} \tag{2.53}$$

where *m* is the mass of electron and *h* is the Planck's constant.

$$J_0 = [q/2\pi\hbar] \times \left[1/(\beta\Delta L)^2\right] \tag{2.54}$$

$$A = [(4\pi\beta\Delta L)/\hbar] \times (2m)^2 \tag{2.55}$$

$$\beta = 1 - \left[1/8\overline{\varphi}^2 \Delta L\right] \int_{L_1}^{L_2} [\varphi(x) - \overline{\varphi}]^2 \partial x \tag{2.56}$$

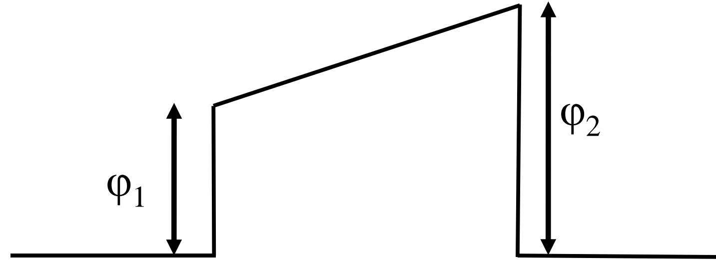

Figure 2.4: Energy band diagram showing the barrier between dissimilar electrodes at $V \cong 0$.

Fig. 2.4 presents the band diagram of low potential barrier between dissimilar electrodes of a MIM diode. At relatively low bias voltage (i.e $V \cong 0$), the current density is calculated as

$$J = \left\{ \frac{(2m)^{0.5}}{\Delta L} \right\} \left(\frac{q}{\hbar} \right)^2 \bar{\varphi}^{0.5} V \exp\left(- A \bar{\varphi}^{0.5} \right) \tag{2.57}$$

$$J = \left(\frac{q^2}{L\hbar^2} \right) \left[m(\phi_1 + \varphi_2) \right]^{0.5} V \times \exp\left[\left(- \frac{4\pi L}{\hbar} \right) m^{0.5} (\phi_1 + \varphi_2)^{0.5} \right] \tag{2.58}$$

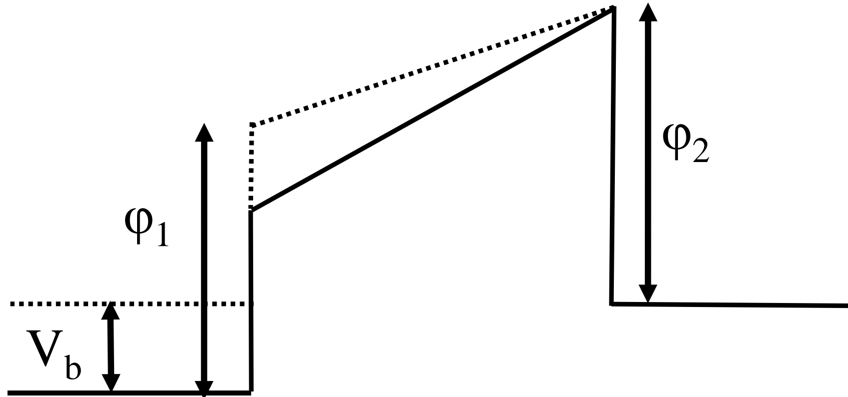

Figure 2.5: The energy band diagram showing the barrier between dissimilar electrodes at the intermediate potential ($V \leq 0 \leq \bar{\varphi}/q$) of the forward bias.

Fig. 2.5 shows an energy diagram of a MIM junction under a intermediate forward bias. Note that the energy band diagram have been tilted to have lower Schottky barrier height at φ_1 compare to φ_2, due to the bias voltage. Though the effect of this creates a trapezoidal barrier that is independent of the bias polarity [76], the electron level moves up in the valence band to allow faster tunneling to the conduction band. The tunneling current is given as:

$$J = \theta\left(V + \gamma V^3\right) \tag{2.59}$$

$$\theta = \left(\frac{q}{h}\right)^2 \frac{\left[m(\varphi_1 + \varphi_2)\right]^{0.5}}{d} \exp\left[-D\left(\frac{\varphi_1 + \varphi_2}{2}\right)^{0.5}\right] \tag{2.60}$$

$$\gamma = \left\{\frac{(Dq)^2}{\left[48(\varphi_1 + \varphi_2)\right]}\right\} - \left(\frac{Dq^2}{32}\right)\left[\frac{2}{(\varphi_1 + \varphi_2)}\right]^{\frac{3}{2}} \tag{2.61}$$

$$D = \frac{4\pi d(2m)^{0.5}}{h} \tag{2.62}$$

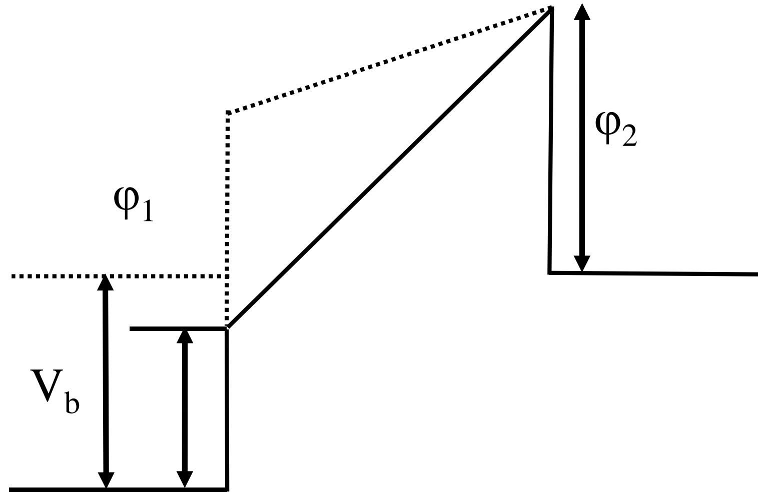

Figure 2.6: The energy band diagram showing the barrier between dissimilar electrodes under a forward-biased potential of $V \geq \overline{\varphi}/q$.

At high voltages (i.e $V > \overline{\varphi}/q$) the rate at which the electrons tunnel from one metal to another is very fast due to the lowering of the barrier height that causes reduction in the length of the electron path. The energy band diagram is shown in Fig. 2.6. The tunneling current under high forward bias voltage is calculated by:

$$J = \left(\frac{BF^2}{\overline{\varphi}}\right)\exp\left[-\left(\frac{\lambda\overline{\varphi}^{\frac{2}{3}}}{F}\right)\right] \tag{2.63}$$

$E = \frac{V}{d}$, is the field between the electrodes

$$B = \frac{1.1q^3}{4\pi h} \tag{2.64}$$

and

$$\lambda = \frac{23\pi m^{0.5}}{6qh} \tag{2.65}$$

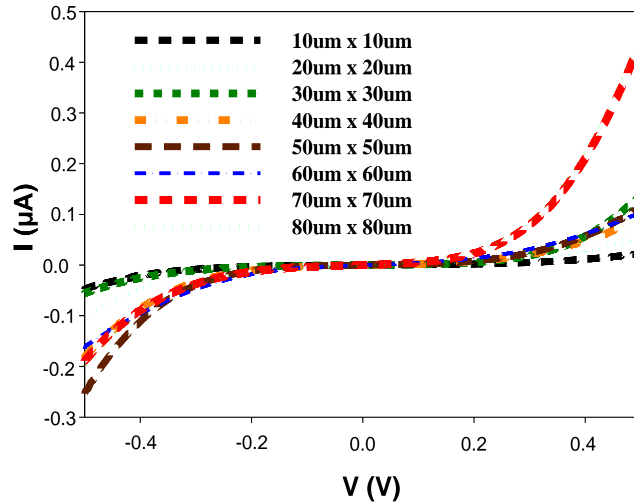

Figure 2.7: The measured *I-V* plots of fabricated MIM diodes operated under the intermediate voltage range.

Typical *I-V* plots of MIM diodes with different junction area are shown in Fig. 2.7. Diode *I-V* characteristics are primarily used to determine the electrical behavior of the device. As de discussed later, the *I-V* characteristic of the MIM diode highly depends on the thickness of the tunnel layer, tunnel material, fabrication methodology, the junction size, and the work function of the electrodes.

2.3.2 Nonlinearity

Nonlinearity can be determined by using the current-voltage plot. When a voltage with a certain frequency is applied to a detector or a mixer, the nonlinear *I-V* response generate a dc output component. Therefore, the performance of a mixer made of a tunneling device depends solely on the nonlinearity of the device [109]. The mathematical expression for the nonlinearity is given by;

$$\chi = \frac{dI}{dV} \Big/ \frac{I}{V} \tag{2.66}$$

The nonlinearity of the diode's *I-V* characteristic is explained in terms of its key parameters such as its work function difference of the contacted metals, their separation, and the applied bias voltage. The tradeoff between nonlinearity and performance of the diode lies in the tunneling layer thickness. High nonlinearity can be achieved by dissimilar metal electrodes and thick tunneling layers; whereas the barrier should be less than 5nm for electrons to tunnel through the barrier. Recently, MIM diodes with multiple thin barrier layers have been used experimentally to improve the nonlinearity.

2.3.3 Asymmetry

Asymmetry is the ratio between the forward current and the reverse current [93]. For rectification, the asymmetry of MIM tunneling should be much greater than one. High asymmetry is anticipated when the difference between the forward turn-on voltage and the reverse breakdown voltage is high. Until recently, development of MIM devices with great asymmetry has been based on application of dissimilar electrodes at both ends of the junction oxide. Thus, asymmetry is determined by the difference between the electrodes' work functions. However, studies have shown that the employment of several different thin tunnel layers to create a metal-insulator-insulator-metal (MIIM) diode can increase the value of asymmetry drastically. Mathematically, the diode's asymmetry is expressed as:

$$\eta = \frac{I_{+}}{I_{-}} \tag{2.67}$$

where I_{+} and I_{-} are currents under forward and reverse bias conditions, respectively.

2.3.4 Rectification and Mixing Operation

MIM is not an ohmic contact device due to a thin tunneling layer that creates a barrier between the two metal electrodes. The rectification can be ascribed to the nonlinearity of tunneling current shown by the current-voltage curve. The mechanism of rectification is based on the proportionality of the rectified signal amplitude to the second derivatives of the *I-V* characteristics [110], which is given by [29]:

$$V_{dc} = \frac{1}{4}\frac{I''(V_b)}{I'(V_b)} \times |V_{ac}|^2 \tag{2.68}$$

where the $I^{"}(V_b)$, and $I^{'}(V_b)$ are the second, first derivative of the tunneling current at a specific bias voltage, respectively. V_{ac} is the magnitude of alternate voltage (AC) signal applied to the tunneling diode. Another factor for evaluating the performance of a MIM diode is its sensitivity. The diode sensitivity is defined as the ratio of the second derivative to the first derivative.

$$S = \frac{I^{"}(V_b)}{I^{'}(V_b)} \tag{2.69}$$

where

$$I^{"}(V_b) = \frac{d^2 I}{dv^2} \tag{2.70}$$

and

$$I^{'}(V_b) = \frac{dI}{dv} \tag{2.71}$$

therefore, rectification can be expressed as:

$$V_{dc} = \propto \frac{1}{4} S \times |V_{ac}|^2 \tag{2.72}$$

MIM diode performance depends on its nonlinearity, differential resistance, responsivity, asymmetry, and applied AC voltage signal.

2.3.5 MIM Diode Performance and RC Time Constant

For a MIM diode designed for high frequency to mix different radiation sources, the response time is required to be fast [29, 111]. One of the significant challenges that limit the operation of MIM diode at THz frequencies is the large junction capacitance and associated RC time constant. An example of equivalent MIM diode circuit model is shown in Fig. 2.8; which

consists of a junction capacitance C_D in parallel with nonlinear resistance R_D, both connected to a series resistance R_s. The cutoff frequency of the circuit is expressed as;

$$f_c = \frac{1}{2\pi R_D C_D} \tag{2.73}$$

junction capacitance is given as

$$C_D = \frac{\varepsilon_o \varepsilon_r A}{d} \tag{2.74}$$

where ε_o is the free space permittivity, ε_r represents the relative permittivity of the tunnel layer, A is the junction area determined by width of the intercept metal electrodes and d represents the tunneling barrier thickness. From the cutoff frequency mathematical expression, it is evident that the value of the junction resistance and capacitance is expected to be fairly low for high frequency operation. While R_D strongly depends on the thickness of the insulator, the contact area and thickness of the insulator have to be kept at the minimum for C_D (as seen in Fig. 1.2). The tunneling time of electrons in MIM devices have been estimated to be on the order of 10^{-16} seconds [112]. However, experimental MIM diodes have been shown to rectify green light (514nm), indicating the tunneling time of carriers is not yet a limitation in the MIM diode [113]. The primary limitation of the MIM diode response time is related to the RC time constant.

CHAPTER 3: MIM DIODE FABRICATION PROCESSING

Lithography, material deposition, and etching are fundamental processes carried out in micro and nano-fabrication. Other important processes include the thin film metrology analysis, mask fabrication, metal lift off and wafer cleaning. In a later section, the device fabrication process and the design consideration of the fabricated devices of this dissertation work will be discussed.

3.1 Lithography

The term lithography is defined as the process employed to transfer micro or nano pattern onto the surface of a wafer. There are two major types of lithography, namely: (1) optical lithography and (2) electron-beam lithography. This study employs both lithography types for device fabrication.

3.1.1 Optical Lithography

This process is mostly used to create micro-size patterns in a photoresist layer already spun on the wafer. The procedures for a photolithography step include: adhesion (optional), resist coating, soft baking, exposure, post-exposure bake, development, and hard bake (optional).

- Resist coating: A small amount of resist (organic polymer whose solubility changes as a result of exposure to UV light) in a liquid form is dispensed onto the wafer with the aid of a clean bottle nozzle or syringe. The resist spinner includes: a) an exhaust hood for eliminating evaporated solvent; b) a vacuum pump for transferring nitrogen gas to the chuck; c) the chuck for holding the wafer down; and d) a timer and speed monitor control

which are adjusted to retain the expected spin rates for the set time to achieve the target thickness. There are two types of photoresist – positive and negative. They are named based on their reactions when exposed to UV radiation. The pattern on the mask is directly transferred to the sample with the use of positive photoresist. This means that every opening in the mask that allows UV radiation to penetrate through to the photoresist will be dissolved in the developer. Contrary to this interaction exhibited by positive photoresist with UV radiation, the negative photoresist tends to be harden over the area of the mask that the UV radiation penetrates through. The unexposed areas are then dissolved in the developer. Resist properties include: viscosity, adhesion, thermal stability, etching resistance, contamination, shelf life, processing difficulty, pinhole density, and charging.

- Soft baking: This process is done to remove residual solvent and to make the resist film dense by applying heat. This process also aids resist stress reduction, planarization on the surface of substrate, polymer cross linking, and oxidation [114].
- Alignment: Mostly used in the micro-fabrication to align one layer to the other, especially when multiple layers of process are required. In that case, alignment is important in order to directly place a new pattern on the top of the preceding layer. This arrangement is important, noting that it is already established in the mask design by including alignment marks. The exposure tool (Fig 3.1(b)) includes an alignment step before exposure.
- Exposure: This is a critical aspect of the photolithography. It is the primary stage that transfers the image pattern to the wafer with the aid of photo-mask and mask aligner. In Fig. 3.1 (a) the wafer is place under the lens in order to project an image of the pattern on the mask directly to the resist coated wafer. With the tool like Karl-Suss presented in

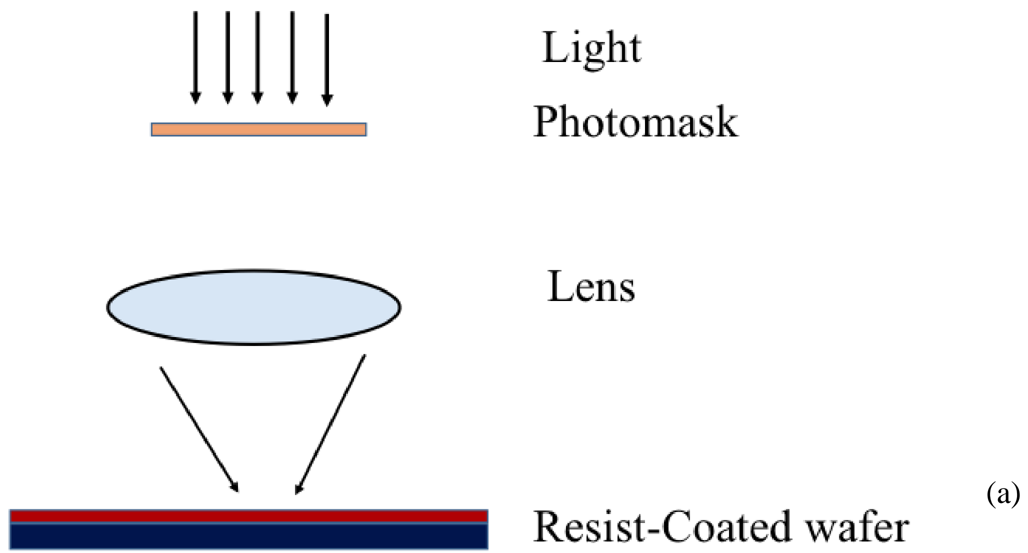

(b)

Figure 3.1: (a) The resist-coated wafer exposure setup under a UV light. (b) The primary tool used for emitting UV radiation. (The image is from Nanotechnology Research & Education Center of University of South Florida.

Fig 3.1(b), the shutter opens and allows UV light to pass through the photo-mask. The pattern is then imaged on the lens that transfers it to the wafer underneath. The optical exposure is performed mostly with the aid of an ultraviolet bulb having a UV signal at either g-line (436nm) or i-line (365nm). The different lines of photoresist are based on a particular photochemistry such as novolak resin and diazonaphthoquinone (DNQ) photoactive compound.

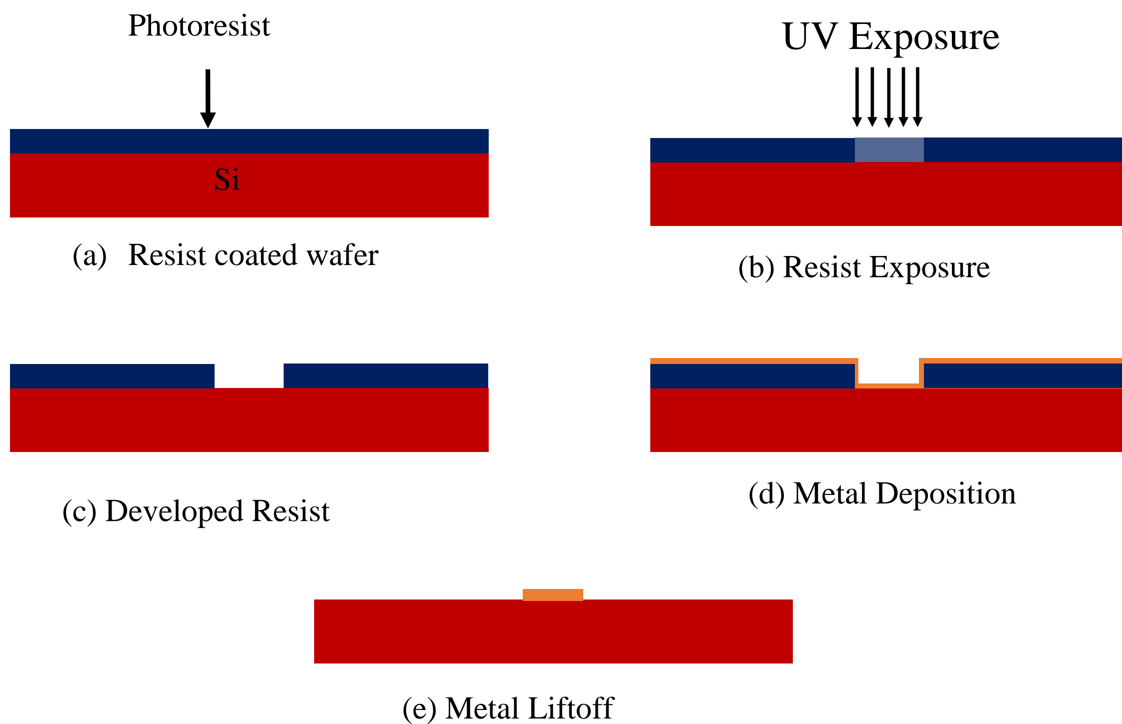

Figure 3.2: A schematic description of mask projection and photolithography's basic processing to establish metal pattern on a substrate. (a) Substrate coated with photoresist, (b) substrate under ultra-violent exposure, (c) resist development showing developed image (d) metal deposition, and (e) metal lift off (removing the photoresist)

- Post-exposure baking: Post exposure baking of resist causes reduction in the polymer decomposition that take place before exposure. Depending on the type of the photoresist, this step is optional; it is primarily applicable to DNQ/novolak resist.
- Development: The exposed resist-coated wafer is immersed into a special resist remover referred to as a developer. Mostly, the exposed resist dissolves in the developer, forming a channel similar to the one shown in Fig. 3.2(c). This process is done in a timely manner to avoid over development. Different resists have different developing time; developer can be of tetramethyl-ammonium hydroxide (TMAH) or of sodium hydroxide (NaOH) base.
- Hard-bake, post-bake or post-development bake: This is an optional and final step of the photolithography process. Compared to soft baking it is usually performed with high temperatures, which serves the purpose of driving out volatile organic materials and water in order to preserve the vacuum integrity. It is a process employed to give the resist adhesion necessary to further substrate processing steps, such as etching and ion implantation.

3.1.2 Electron Beam Lithography

Like optical lithography, E-beam lithography (EBL) is a process of transferring a pattern from one medium to another, but its application is to pattern devices well beyond the UV lithography capability. One of the major advantages of EBL over the conventional UV lithography method is that it produces very high resolution and versatile pattern formation [115]. Another advantage is that the technique can produce a device as small as 10nm. The commonly used process with EBL is liftoff. This process consists of a series of steps: spinning of the e-

beam resist on the wafer substrates, baking of the e-beam resist coated wafer, exposure and e-beam resist development.

- E-Beam resist application: Both positive and negative e-beam resists were employed in the work done in this dissertation. The positive resist becomes soluble in the resist developer after exposure to electron beams. On the other hand, the negative e-beam resist becomes less soluble in the developer and strengthens during exposure to the e-beam radiation. Polymethyl methacrylate (PMMA) and Shipley advanced lithography (SAL) are commonly used positive and negative resist, and they were employed for fabrication. These resists are supplied to the end users in powdered form to be mixed in and dissolved in solvent for appropriately required thickness. The resist liquid is dropped on the substrate and spun at high speed for 1min for uniformed thin coating.
- Soft baking: Following the spinning, the resist is baked on a hot plate or in an oven for 3min at 180 degrees for positive resist and 90 seconds at 95 degrees for the negative resist.
- Exposure: The resist coated substrate is exposed to e-beam direct [115] using a raster scan. In scanning a specific area of the substrate, the desired pattern is transferred through the deposition of energy. Depending on the resist thickness, the exposure dose is measured in $\mu C/cm^2$ at working electron accelerating voltage.
- Development: When the resist is exposed, the polymer compound chain is broken making it soluble in developer. Methyl-isobutyl-ketone (MIBK) mixed with isopropanol (IPA) at ratio 1:3 is commonly used for PMMA development.

Figure 3.2 schematically describes the normal lift-off sequence similar to e-beam lithography. While the resist used under UV radiation described in the figure is for a negative

photoresist, a positive e-beam will be of the same process. This process was used for defining metal contact for both optical and e-beam lithography throughout this work.

3.2 Scanning Electron Microscope (SEM) for E-beam Lithography

Figure 3.3 represents a typical schematic sectional view of an electron optical column for an E-beam generating tool used for lithography. This tool is capable of generating an extremely fine pattern. For simple analysis, the system is divided into two stages. Stage 1 is for electron beam shaping and stage 2 is for the focusing of the electron on the work-piece. In this system, the electron that is emitted by the electron gun is focused toward two magnetic lenses (condenser lenses) by anode aperture. The first and the second condensers are used to step down the excess beam current flowing down the column. Another purpose of stage 1 is that it reduces electron interaction, which increases the diameter of the focused spot on the work-piece. In addition, at stage 1 low current flows through the column increases the opportunity to reduce the contamination from polymerizing residual from hydrocarbon that forms while insulating film on the optical element [116, 117]. Stage 2 consists of an electrostatics deflector used in adjusting the focused beam over the surface of a work-piece. During the lithography process, the beam can be turned off and on by the beam blanker. Beam alignment and stigmatization are corrected and controlled at this section of the e-beam tool system.

The dose D which is charge density to be delivered to the exposed region is given by

$$D = \frac{T \times I}{A} \tag{3.1}$$

where I is the beam current delivered to the work-piece, A is the area on the wafer to be exposed to the e-beam, and T is the total exposure time. The delivered current **I** is a factor numerical

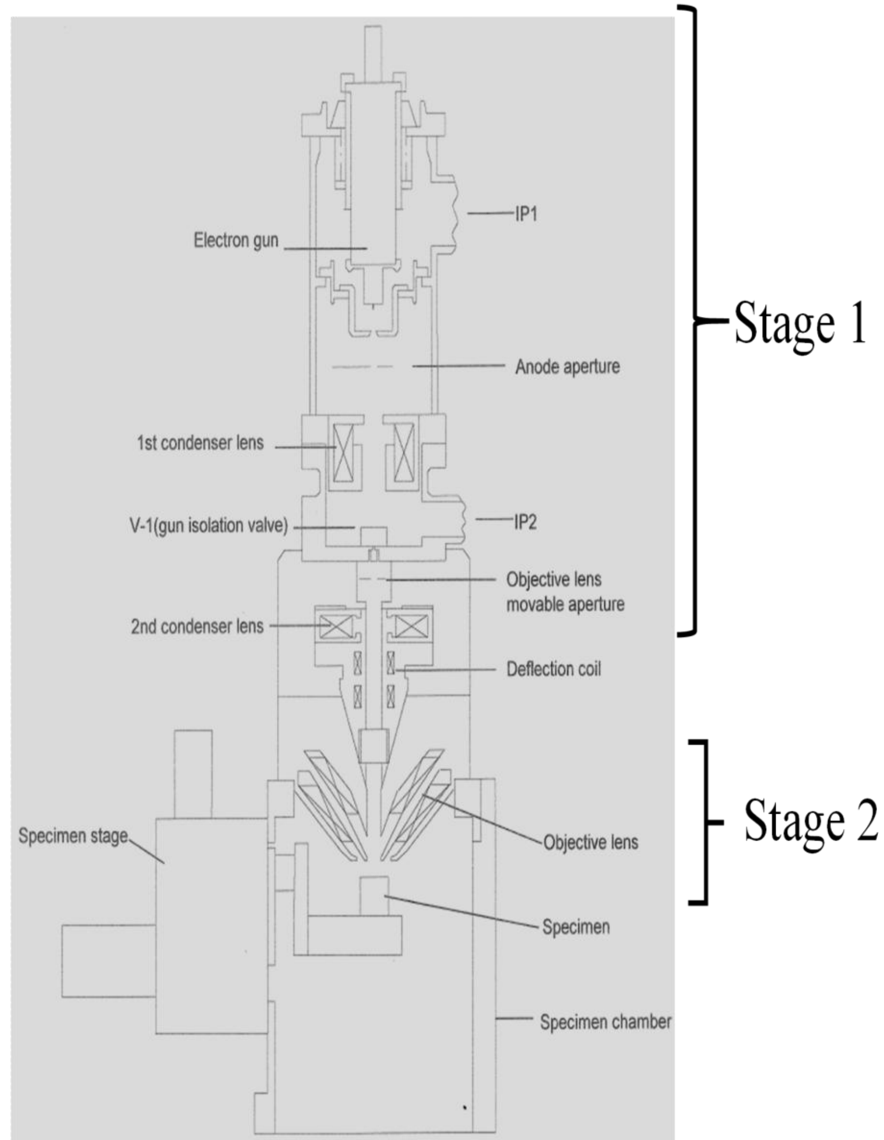

Figure 3.3: Ray diagram of the electron optical system of a round beam electron beam system. (Courtesy - University of South Florida Nanotechnology Research and Educational Center NREC).

aperture (α) and the diameter of the spot focused on the substrate (*d*). The relationship is expressed as,

$$I = \beta\left(\frac{\pi d^2}{4}\right)\left(\pi\alpha^2\right) \tag{3.2}$$

where β is the brightness of the source.

Fig. 3.4 shows an image of an ultra-high resolution analytical scanning electron microscope used for E-beam lithography. This Hitachi model (SU-70) is used to support of this study. One of the properties of the tool is that it combines the field proven stability, high current and brightness of the Schottky electron source with ultra-high resolution required for analytical application [118]. The tool is designed to reduce specimen charging and entrance compositional contrast as a result of built-in optical configuration. Apart from the tool's capability to perform EBL of nano-structure, it can also be used for Energy Dispersive X-Ray (EDS or EDX) Wavelength Dispersive Spectroscopy (WDS), Electron Backscatter Diffraction (EBSD), Cathode-Luminescence (CL) and Scanning Transmission Electron Microscopy (STEM) simultaneously. Specifications and capabilities include; 1nm resolution 15keV at 4mm working distance, 800K times magnification, thermal field emission source, remote Control Capability, and 3D Rendering and Metrology.

Figure 3.4: The Hitachi SU-70 analytical field emission SEM. A field-emission SEM designed to perforn ultra-high resolution imaging together with various analytical functions. (Courtesy –NREC).

E-beam lithography process performed to fabricate the nano-device in this dissertation was done with the JEOL9300 shown in Fig. 3.5. The tool is housed at the Center for Nanoscale Materials (CNM) at Argonne National Laboratory where the nano devices were fabricated. It is a 100keV electron lithography system that is capable of (re)producing feature sizes below 30nm. Additionally, it is also a proper tool for multilayer EBL with less than 20nm overlay accuracy on a wide variety of substrates. Five inch (5”) masks and wafer sizes of 3”, 4”, 6”, 8", and 12” diameters, as well as smaller pieces, can be accommodated for exposure with this tool.

Figure 3.5: JEOL JBX-9300FS electron beam lithography system. (Courtesy Georgia Institute of Technology Nanotechnology Research Center (TNRC))

The tool’s capability and features include [119, 120]:

- 4nm diameter Gaussian spot electron beam
- 50kV/100kV accelerating voltage
- 20-bit pattern generator

- 50pA –100nA current range
- 50MHz scan speed or pattern generated speed
- 1nm address grid or field size
- +/-100um vertical range automatic focus
- +/-2mm vertical range manual focus
- ZrO/W thermal field emission source
- vector scan for beam deflection
- max 300mm (12") wafers with 9" of writing area
- < 20nm line width writing at 100kV
- < 20nm field stitching accuracy at 100kV
- < 25nm overlay accuracy at 100kV

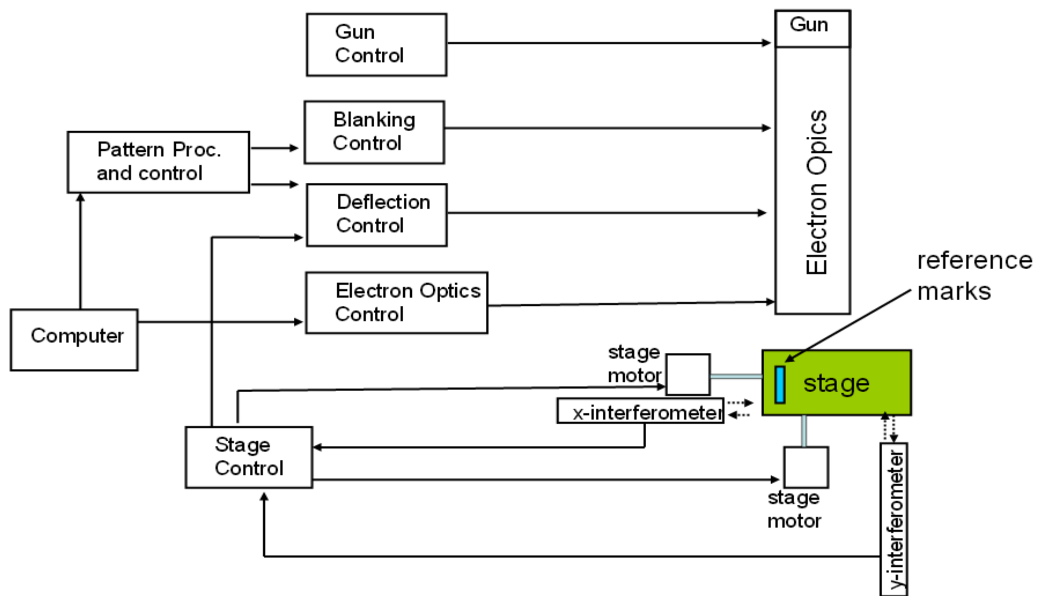

Figure 3.6: Generic block diagram for electron beam (E-beam) generation. (Courtesy – NTRC)

The JEOL9300 optical column configuration is similar to the one described in Fig. 3.3. The E-beam generator the generic block diagram is shown in Fig. 3.6. The electron beam is generated by thermal field emission (TFE) cathode gun incorporating a Zr/O/W emitter and 4 accelerating electrodes. The electron accelerating between 50 -100KV toward the anode passes through double blanking electrodes that prevent beam radiation from the sample. The function of the condenser lens is to control the direction of the e-beam. The beam focusing is done by the objective lens while the sub-deflector, stigma electrode and main deflector incorporated with electron optics control are used to reduce the imperfection in the construction in the e-beam column [121, 122].

JEOL 9300 chamber can handle up to 300 mm wafer, although the maximum writing area is 230nm × 230nm. Wafer transfer to the exposure chamber is done automatically. This means that no human intervention is necessary after the wafer has been placed in the cassette. The cassette has different wafer size slots; a cassette for a 4” wafer can take up to 4 wafers. Furthermore, the system is capable of continuously writing patterns. Different automation is involved in pattern writing to improve its accuracy: a) the height and position of local alignment is measured before writing any pattern; b) the correction parameters of position are calculated for each pattern; and c) the bean positions are corrected along (X,Y) and for the focus of each pattern to be written.

3.3 Thin Film Deposition

Different methods of deposition of thin film layer have been employed to manufacture integrated circuits. Thin film process is applicable to epitaxial layers, thermal oxides, dielectric layers, polycrystalline silicon, and metal film [123]. The commonly used techniques are divided into two main groups: physical vapor deposition (PVD) and chemical vapor deposition (CVD).

However, there are other methods involved in growing thin film layers in micro and nano-fabrication. These methods include oxidation, spin coating, plating, and atomic layer deposition (ALD).

The applicable deposition technique for a process is determined by the following characteristics:

- Deposition rate
- Film uniformity
  - Uniformity across the wafer
  - Repeatability of sequential run
- Deposition system material compatibility
  - Semiconductor
  - Alloy
  - Metal
  - Dielectric
  - Polymer
- Thin film properties
  - Adhesion
  - Stress
  - Film density
  - Pinhole density
  - Impurity level
  - Grain size, orientation and boundary properties
- Directionality

- Directional: lift-off and trench filling applicability
- Non-directional: step coverage applicability

- Deposition system cost and operation.

This study employed the use of physical vapor deposition techniques (PVD) for metal deposition and atomic layer deposition (ALD) for deposition of metal oxide. Both techniques will be discussed in the next section.

3.3.1 Atomic Layer Deposition (ALD)

Atomic layer deposition (ALD) is a chemical gas phase thin film deposition process. The deposition is based on sequential self-terminating gas-solid reactions [124-128]. The film grown is based on sequential saturated surface reactions of two or more precursors pulsed into the reactor alternatively. The purging and evacuation take place one at a time during the reactor operation. This process is a chemical vapor deposition technique that has the capability of growing material with thickness as small as a fraction of monolayer. In this work, ALD is employed to deposit the thin films of the oxide layer ranging between 2nm and 4nm. In MIM diodes, the tunnel layer should consist of an ultra-thin dielectric film while maintaining uniform insulator coverage over the entire contact area [85, 129]. One of the critical requirements for a reproducible MIM diode with great performance is the ability to have a depositable high quality tunnel layer(s) thin film. Because of this insulator characteristic, the ALD deposition process is considered to achieve satisfactory fabrication yield and repeatability with ultra-thin and uniform tunneling layers [130].

The ALD system grows oxide layer(s) in a cyclical manner. In one ALD cycle, there are four constituent steps involved for growth of an oxide monolayer to take place, including a) a self-terminating reaction of the first metallic oxide precursor; b) purging to remove the residual

reactant and the by-product; c) self-terminating reaction of the second reactant (typically an oxidizer, such as water steam or oxygen); and 4) another purging step. The temperature and time of each step play a significant role in determining the quality of the film [131]. The significance of the sequences of the process gives ALD an edge over other methods of depositing thin film.

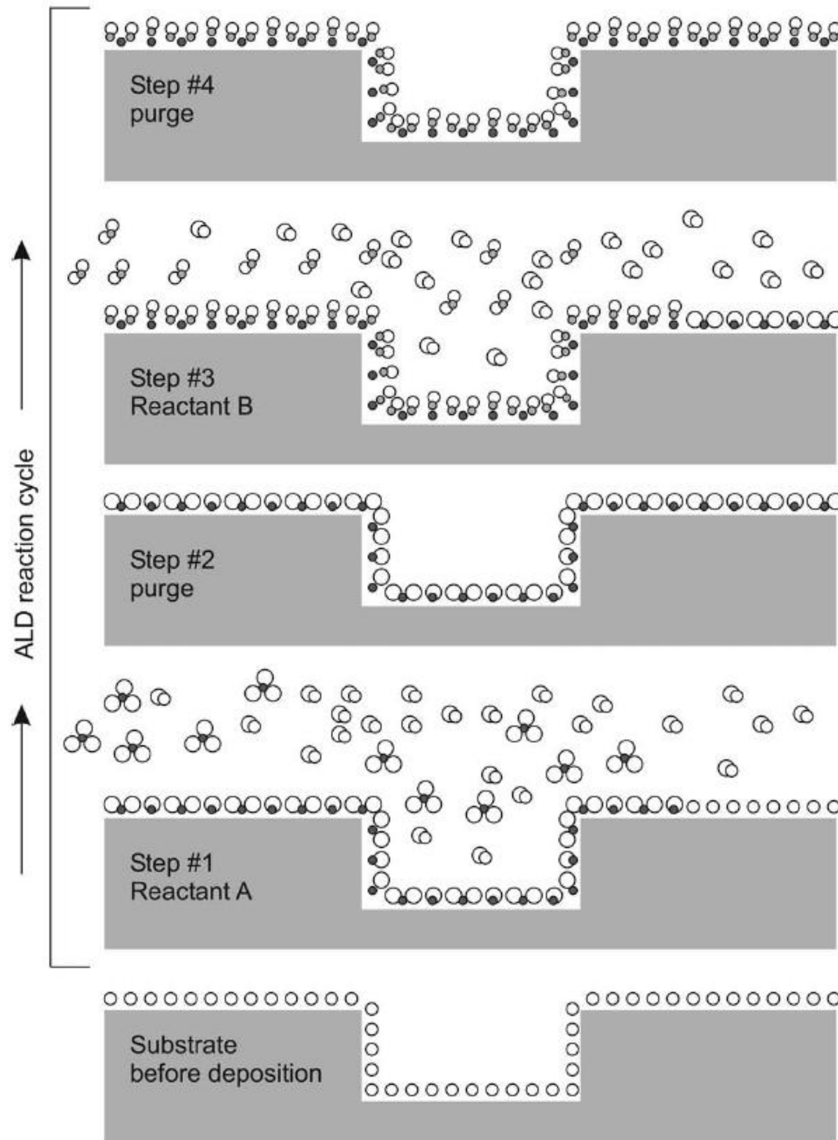

Figure 3.7: A complete one cycle schematic description of atomic layer deposition [124].

Both ALD and chemical vapor deposition (CVD) processes involve binary reaction. The difference is that for CVD, all the process reactants are present at the same time and will continuously form the product on the sample substrate. However, for ALD, the reactants are separately in contact with the substrate and there is individual exposure of the substrate to the reactant to form the product in a stepwise and digital fashion [127]. A schematic diagram of the stepwise process of ALD deposition is shown in Fig. 3.7.

One of the advantages of ALD is precise film thickness control down to the level of Angstrom. This is based on the number of the deposition cycles. Another advantage is the self-limiting growth capability of the system. This leads to large area coverage, batch scalability, good reproducibility and excellent coverage conformity on a high aspect ratio structure. For ALD deposition, nanolaminates and superlattices can be easily deposited due to atomic level control material composition. The pulsing of the reactants in ALD eliminates gas phase reactions. Thereby, the system enables short cycle time and effective precursor's usage. As a result of these characteristics, materials with high quality can be obtained at low temperature. Another advantage of the ALD system lies in continuous deposition of multilayer's of different materials due to wide windows of processing temperatures.

As discussed earlier, often the material properties dictate the deposition method that is applicable.. As shown in Table 3.1, the different deposition methods used in micro-fabrication are listed, including thermal evaporation, electron beam evaporation, sputtering, PECVD, LPCVD, and ALD. Different methods are compared based on the material, degree of uniformity, level of impurity, the grain size, film density, deposition rate, deposition temperature, and the cost.

Table 3.1: Summary of the characteristics of different material depositions used in micro and nano fabrication

Proc.	Mat.	Uniformity	Impurity	Grain Size (nm)	Film Density	Dep. Rate A/s	Temp. ^{o}C	Cost
Thermal evaporation	Metal & Low melting point materials	Poor	High	10-100	Poor	1-20	50-100	Very low
E-beam evaporation	Metal and Oxides	Poor	Low	10-100	Poor	10-100	50-100	High
Sputter	Metal and Oxides	Very Good	Low	~10	Good	1-100	~200	High
PECVD	Oxides	Good	Very Low	10-100	Good	1-100	200-300	High
LPCVD	Oxides	Very Good	Very Low	1-10	Good	10-100	600~1200	High
ALD	Metal and Oxides	Very Good	Very low	~0.3A	Very Good	0.3A	150-300	High

3.4 Etching

In micro or nano fabrication processes, etching is one of the fundamental processes [132, 133]. The etching process is carried out to transfer a mask pattern to the underlying layer on the substrate. Through etching step, part of the underlying thin film layer(s) is removed by chemical reaction simply referred to as an etchant [114, 134]. One of the germane factors considered in the etching process is the chemical reaction selectivity between material(s) to be etched and the mask or other exposed material.

The process is categorized into two main categories: wet etching and dry plasma etching. Wet etchants are liquid chemical mixtures that react with selective material(s) with effort to dissolve the materials. Wet etch can have high selectivity and the etching rate can be very high as well. On the other hand, dry etching employs the plasma gas to etch material. The materials are removed by the bombardment of ions. The fabrication work done in this study employed both

wet and dry etching techniques pattern metal oxides. The choice of the method used depends on the critical dimension to be formed. For the micro devices, wet etching was used and for nano devices, dry plasma etching was employed.

3.5 Device Fabrication and Metrology

3.5.1 Device Fabrication Process

In order for MIM diodes to operate with a faster response time and have high sensitivity at high frequencies, the size of the contact area has to be small. As discussed in Section 2.3, the material's physical characteristics, such as metal(s) work function, tunnel layer electron affinity and thickness, and the junction areas, determine the performance of the diode. Therefore, one of the MIM diode design objectives is to keep the device contact area as small as possible. The second objective is to select electrode materials (metals) with large work function differences in order to improve on the nonlinearity of the MIM diode [32, 88, 135]. The selection is done by compromising the conductivity to obtain large offsets in work functions between the metals. Thirdly, the tunneling material is carefully chosen based on its dielectric constant, electron affinity, and band gap. Also, methods of depositing an ultra-thin tunnel layer should be able to maintain uniform insulator coverage over the entire contact area [85, 129]. This is the most critical issue in the manufacturing of MIM diodes. The smaller the contact area, the more uniform the dielectric tunnel layer, and the better the tunneling characteristics are atomic layer deposition (ALD) process is used to achieve satisfactory fabrication yield and repeatability for depositing ultra-thin and uniform tunneling layers [130], because of the low tolerance for non-uniformity and pin-hole. ALD was discussed extensively in Section 3.3.1.

In this study, effort was devoted to fabricate micro and nano junction size devices. An ultraviolet photolithography process was employed to fabricate micro-sized devices, while an e-beam lithography process was used for nano junction sized devices. In both processes, the devices were fabricated on similar substrates, bottom and top electrodes were kept the save, and the same tunnel layer was explored.

3.5.1.1 Substrates

A high resistivity silicon wafer was used throughout the experiments performed in this work. A <100> double-sided polished silicon wafer substrate of 100mm in diameter was used. The substrate dielectric constant was about 11.7, the dielectric strength was approximately varied between 100 – 700 V/mil, the loss tangent was 0.005 @ 1GHz a. The high resistivity silicon wafer was used to provide good device-to-device isolation.

The RCA cleaning procedure was employed. The cleaning fell into primarily three categories: a) removal of gross contaminants, including oily layer; b) removal of organic contaminants; and c) removal of light and heavy metallic ion contaminants. The chemicals used included hydrofluoric acid (HF), hydrochloric acid (HCL), hydrogen peroxide (H_2O_2), ammonium hydroxide (NH_4OH) and de-ionized water (DI). The organic contaminants and metals on the new substrates were removed by RCA1 solution, which consisted of a ratio of DI: H_2O_2: NH_4OH at 6:1:1 by volume. The oxide layer was removed with RCA2 solution, which is composed of the chemical DI: H_2O_2: HCl at 6:1:1 ratio by volume.

The cleaning procedure was done on the wet bench designated for cleaning new wafers only. The procedure was as follows:

- The wet bench area was cleaned with DI water and dried with a clean room wipe.

- Each 2 fused quartz containers designated for RCA1 and RCA2 were filled with 2 liters of DI water. The heater was turned on. The temperature on both containers was set to 80^oC.
- When the temperature of the water reached 65^oC, 330ml of H_2O_2 (30%) and 330ml of NH_4OH was added to the RCA1container and to RCA2, 330ml of H_2O_2 (30%) and 330ml of HCl was added.
- The new wafers were dipped into a quartz container filled with HF (50: 1), agitating for 20 sec up/down.
  - The wafer(s) were transferred directly for 2 cycles of rinse.
  - The wafer(s) were submerged into RCA1 solution for 10 minutes.
  - Transferred directly for 2 cycles of rinse.
  - Dipped in HF for 20 seconds and then rinsed.
  - Transferred directly for 2 cycles of rinse.
- The SC1 hotplate was turned off and solution was covered to prevent NH_4Cl or NH_4F formation in bench area.
- Wafers were submerged in RCA2 solution for 10 minutes.
  - Wafers were rinsed in DI water and the RCA2 hotplate turned off.
  - The wafers were dipped in HF for 20 seconds.
  - Wafers were rinsed.
  - Wafers were spin-dried the in the spinner.
- RCA1 solution was poured in middle of the wet bench sink and followed with rinse for 3-4 minutes. Next the same was repeated with the RCA2 solution.

- The wafers were removed and hotplates put away. Quartz containers were rinsed out and returned to shelf.
- All wet bench surfaces were sprayed down with DI water and squeegee used to wipe off excess water.

3.5.1.2 Metal Selection

The material choice of metal electrodes is of significant importance in determining the characteristics of the tunneling metal-insulator-metal (MIM) diode. While metals' electrical properties, such as work function, are critical factors to the diode performance, the metals' mechanical properties are other factors that play critical roles in the fabrication process. Mechanical properties such as toughness, brittleness, ductility, malleability, and corrosion resistance determine the methods of thin film growth system compatible, as with any material. For example, as shown in Table 3.2 below, gold (Au) and copper (Cu) have high work functions and they offer great corrosion resistant, malleable, and ductile properties but can easily contaminate the fabrication tools. Therefore, they are not the top choice metal, when etching or other processing steps/equipment is required.

Additionally, selection of electrode materials (metals) for fabrication is of great concern because it contributes to the nonlinearity of MIM diodes [32, 88, 135]. The selection is done by compromising the conductivity to obtain large offset in work functions between the metals. The work function, conductivity, melting point and density of different metals are listed in Table 3.2. As discussed in chapter 2, the barrier height, at the interface of contact between the metal and the tunneling layer, contributes to the energy band diagram, which influences the electron tunneling.

Heat conductivity and the melting point are factors of deposition dependency that can affect the heat transfer of the structure. For this study, Titanium (Ti) with work function of

4.33eV and platinum (Pt) with work function of 5.66eV were used. This is a result of the high degree of difference in their work function values.

Table 3.2: The comparison of metal properties showing the metal work function, the metal heat conductivity, electrical conductivity, melting point and bulk density.

	Work Function (eV)	Heat Conductivity (W/mK) @ ^{o}C	Electrical Conductivity (10^{-8} Ωm) ^{o}C	Melting Point (^{o}C)	Bulk Density (g/cm^{3})
Aluminum (Al)	4.28	2.5	236	660	2700
Antimony (Sb)	4.08	25.5	39	630	6.62
Barium (Ba)	2.49		36	710	3.51
Bismuth (Bi)	4.4	8.2	107	271	9.80
Calcium (Ca)	2.8		3.2	840	1.55
Chromium (Cr)	4.5	96.5	12.7	1860	7.19
Copper (Cu)	4.4	1.55	403	1084	8.94
Gallium (Ga)	3.96	41	13.6	30	5.91
Gold (Au)	5.1	319	2.05	1064	19.32
Iron (Fe)	4.31	83.5	8.9	1540	7.87
Magnesium (Mg)	3.64	157	3.94	650	1.74
Manganese (Mn)	3.83	8	138	1250	7.39
Mercury (Hg)	4.52	7.8	94.1	-39	13.55
Molybdenum (Mo)	4.6	139	5	2620	10.22
Nickel (Ni)	5.15	94	6.2	1455	8.91
Niobium (Nb)	3.99	53	15.2	2425	8.57
Platinum (Pt)	5.65	72	9.81	1772	21.45
Silver (Ag)	4.26	428	1.47	961	10.49
Titanium (Ti)	4.33	22	39	1670	4.50
Tungsten (W)	4.55	177	4.9	3387	19.3
Zinc (Zn)	4.24	117	5.5	419	7.14

3.5.1.3 Micro Device Mask Design

Micro scale MIM diodes were fabricated using UV photolithography. The process involved manufacturing of photo mask, which is very critical to the process. Photo mask is a transparent plate with desired pattern that is employed to transfer a pattern to the substrate when UV radiation travels through it. The common ones are made of soda lime glass with a physical size of 5” × 5” × 0.09” and are coated the approximately 70nm thick of chrome layer.

The micro-scale device mask was designed with three objectives:

- To fabricate a device with operational frequency at the GHz frequencies.
- To run fabricate devices with a wide range of junction sizes, in order to study the effect of the junction size on the operation and performance of the diode.
- To study and verify the effect of the tunnel layer thickness on performance characteristics, especially the nonlinearity of the diode.

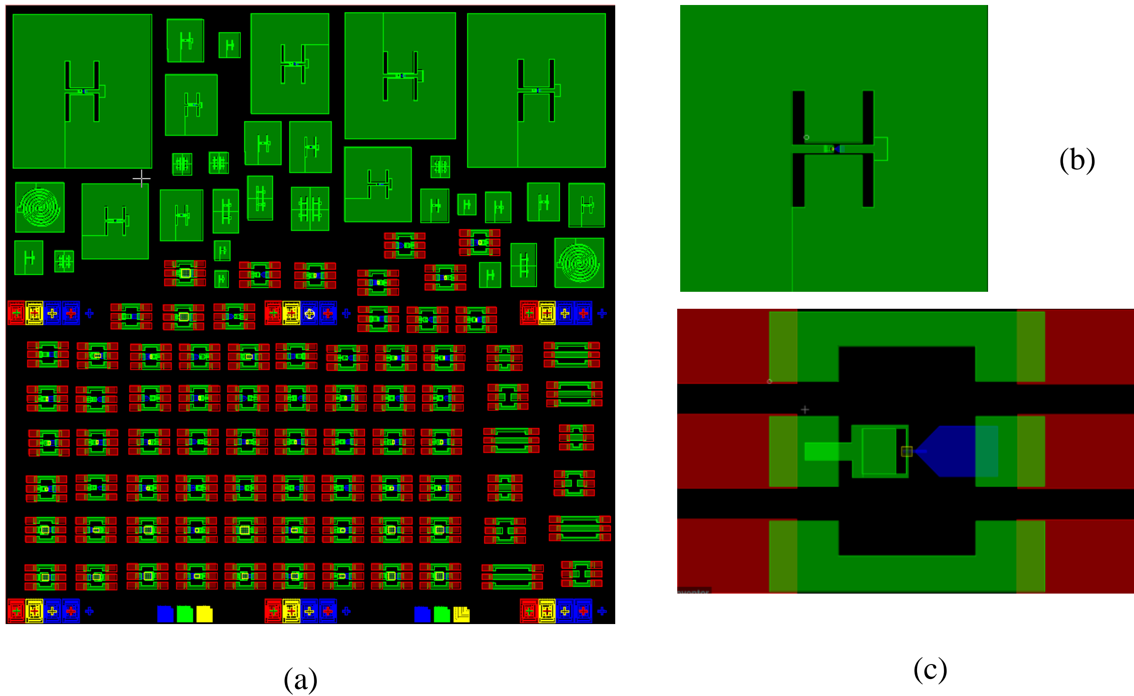

Figure 3.8: The mask CAD design image. a) Zoom-out view of the entire 4-layer masks showing layer of different devices; b) slot antenna with coupled diode; and c) the MIM tunneling junction diode in zoom-in view.

Two CAD software - CoventorWare and Ledit [136] were employed to conduce design and layout to create the photo mask. The initial layout design was done with CoventorWare due

to its superb user friendly interface. The layout design was then transferred to Ledit via the graphic data system (GDS) format.

L-Edit is the standard CAD software that is used by the Nanotechnology Research and Education Center at the University of South Florida. Its design output file is compatible with the mask making tool available at the center. It is also a great tool to create polygon, arcs, circles, pie slices, spirals and lettering. In addition, with L-Edit, pattern designs can be modularized into cells.

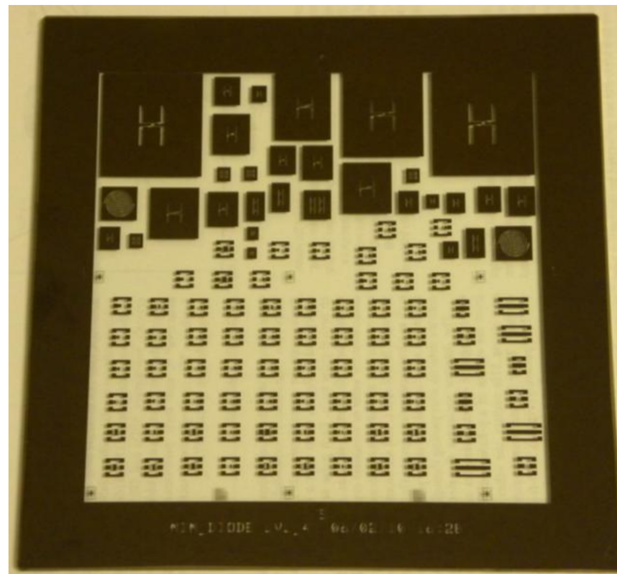

Figure 3.9: A top-view photo of the first layer photolithography mask plate.

Four layer masks were designed, fabricated for development of MIM diodes. The diode junction sizes ranged from 1μm×1μm to 100μm×100μm. Fig. 3.9 shows the photo of the first photo mask for the four-mask fabrication process. The photo mask was divided into two portions; the lower part had a variety of diode designs with different junction sizes and the upper part had slot and spiral antennas directly coupled with the diode. As shown in the figure, the double slot antennas were designed with 50Ω impedance for the initial test of the miniaturized

antennas. The antenna design employed herein was comprised of double slot dipoles connected to a diode.

3.5.1.4 Metal Oxide

ALD metal oxides were employed as tunnel layers for MIM diodes studies by this work. As discussed in Chapter 2, for an electron to tunnel through a barrier at a low voltage, the tunnel layer is required to be no more than a few nanometers thick. For that reason, metallic oxides were deposited by ALD process to offer a great physical thickness and dielectric properties that improved the junction capacitance and reduced the leakage current [137-139]. Junction capacitance for instance, is mathematically expressed as;

$$C = \kappa \varepsilon_o A / t$$

where A is the contact area of the junction, κ is the dielectric constant, ε_o is the permittivity of the free space, and t is the thickness of the tunnel layer.

Apart from the dielectric characteristics of the materials under consideration, other factors that needed to be considered include: a) good thermal stability to prevent formation of interfacial layers; b) low density of intrinsic defect at the interface; c) a sufficiently large band gap to provide a high energy barrier (barrier height) at the metal/oxide interface; and d) the material should be compatible with the CMOS IC processing techniques. Table 3.3 shows the list of some materials, including their key properties, such as dielectric constant and band gap.

Table 3.3: Key properties of candidates materials considered for as plausible tunneling layer [140-142].

Material	Dielectric Constant (ε_r)	Band Gap (E_G) (eV)	Electron Affinity (eV)
Si_4N_4	3.8	5.3	2.1
Al_2O_3	9	8.7	1.35
Y_2O_3	15	5.6	1.85
La_2O_3	22	5.6	2.5
Ta_2O_5	26	4.5	3.75
TiO_2	80	3.5	2.95
HfO_2	25	5.7	2.65
ZrO_2	25	5.8	2.75
Gd_2O_3	4.8	5.8	3.5
Yb_2O_5	15	5.6	1.85
Dy_2O_3	14	4.8	1.75
Nb_2O_5	50	4.35	1.7

3.5.1.5 Fabrication

The fabrication processes involved a four-mask UV photolithography process as shown in Fig.3.10. First, high-resistivity silicon wafers were cleaned following standard procedures known as an RCA clean. Thereafter, negative photoresist (NR9-3000PY from Futurrex Inc.) was used for patterning the bottom Pt electrode by a liftoff process. The photoresist was applied by spin coating at 3000rpm for 40s followed by soft baking for 60s at 150°C. Post-exposure bake was done at 100°C for 60s after exposing to UV light with 365nm wavelength. A layer of Platinum (Pt) was deposited by e-beam evaporation to form the bottom electrode through a standard liftoff process. The same photolithography procedures were also carried out for the second and fourth layer. For the third layer, positive photoresist Shipley 1813 was used for patterning. At first, the hexamethyldisiloxane (HDMS) was spun at 3300rpm for 40 seconds, after which the resist was spun at the same rate and soft baked at 90°C for 3 minutes. The resist was exposed for 4 seconds, and then developed for 90 seconds in MF 319 developer.

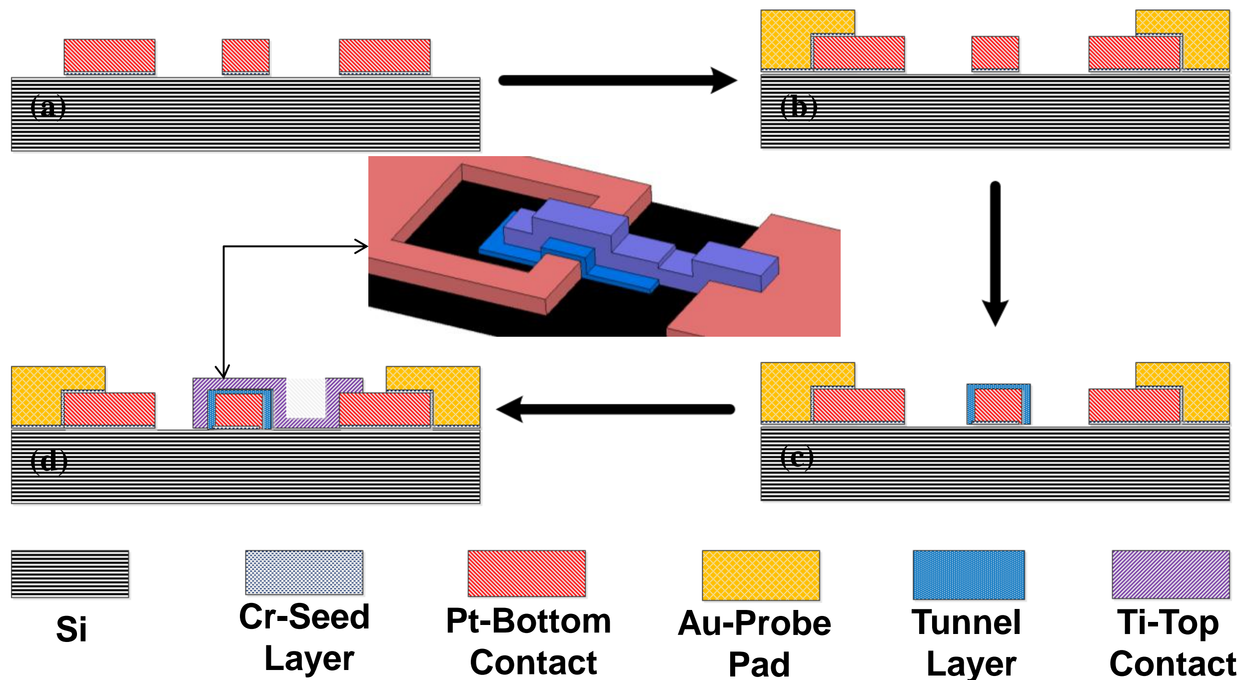

Figure 3.10: Step-by-step illustration of the four-mask UV photolithography fabrication process, including the deposition and patterning. (a) the first (bottom) electrode; (b) gold probe pads; (c) ultra-thin ALD tunnel layer; and (d) the second (top) electrode.

1µm-thick-gold contact electrode was introduced in order to facilitate a better contact for on-wafer probing measurements. Subsequently, the metal oxide layer (the third layer) was deposited via atomic layer deposition. The oxide layer was then wet etched using 10:1 diluted buffered oxide etchant (BOE) solution for 5 minutes. This ALD process was followed by the final metallization step to define the Ti top electrodes of the MIM devices.

Titanium (Ti) and platinum (Pt) with work function of 4.33eV and 5.6eV respectively were employed as metal materials for the junction. The step-by-step process flow is illustrated in Figure 3.9. The metal deposition processes were carried out by e-beam evaporation. Atomic Layer Deposition (ALD) was employed for depositing the tunnel junction layer(s). ALD

deposition has the unique capability of producing a digitally controlled, extremely uniform and conformal tunnel layer of an ultra-thin thickness in the range of a few nanometers [143].

3.5.2 Metrology

The sample SEM image of a fabricated MIM device is shown in Fig. 3.11. The image was taken using JEOL SU-70 (Fig. 3.4) housed in the NREC at USF. High yield and repeatability of the MIM diode fabrication were observed. This can be ascribed to the great control of the thickness and the uniformity of the tunnel layers. Fig. 3.12 presents a Transmission Electron Microscopy (TEM) image showing the tunnel oxide layer of HfO_2 in between Pt bottom electrode and Ti top electrode. Generally speaking, the ALD process can be described as a thin film deposition method that is based on sequentially pulsed self-terminating precursors [131]. Figure 3.13 show the energy dispersive x-ray (EDX) scan result to reveal and verify the composition of the materials.

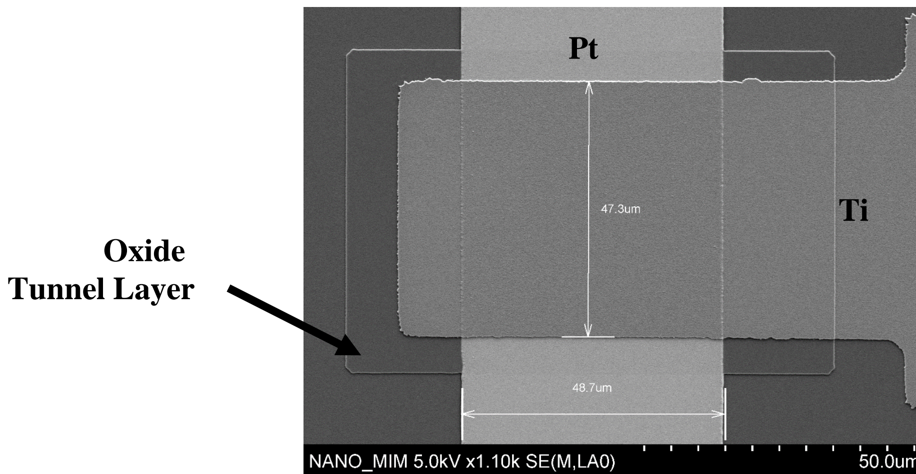

Figure 3.11: SEM images of the fabricated MIM diode device showing 50µm×50µm junction size

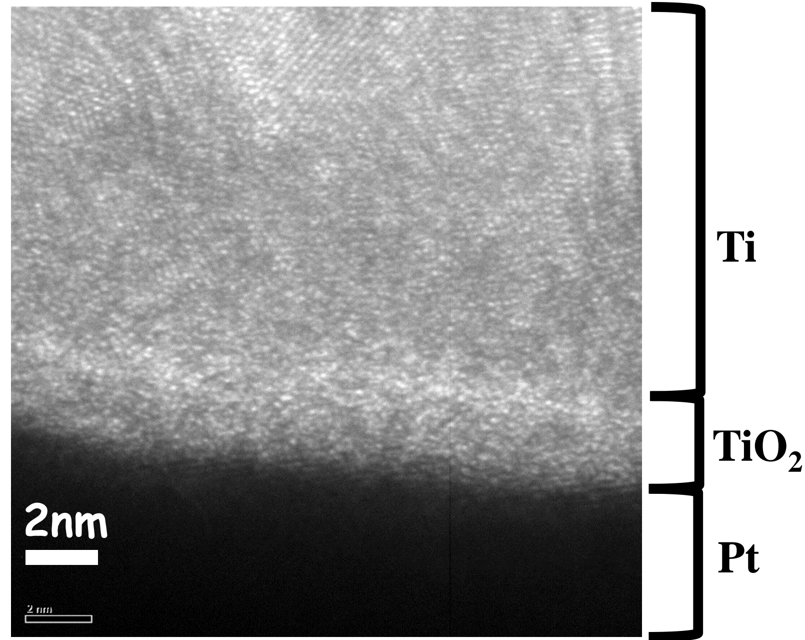

Figure 3.12: TEM cross-sectional image of MIM junction showing interfacial layers of TiO2 in between Ti (top) and Pt (bottom) electrodes

By employing the atomic layer deposition (ALD) process, we have successfully fabricated MIM diodes with a variety of junction areas ranging from 3μm×3μm to 100μm×100μm. The ALD technique offers a superb uniformity, low defect density, and precise thickness control of the tunneling insulator layer. Hence, several ultra-thin insulator materials (e.g., Al_2O_3, TiO_2 and HfO_2) with varied thicknesses have been concurrently explored. The systematic investigation of the measured *I*-*V* characteristics of these MIM devices clearly demonstrated that their performances can be greatly enhanced by optimizing the junction properties as compared to similar devices reported previously. In some MIM devices built with 3nm-thick tunneling junctions, junction resistances in the range of 50Ω or less have been demonstrated, while exhibiting a great promise for achieving enhanced responsivity.

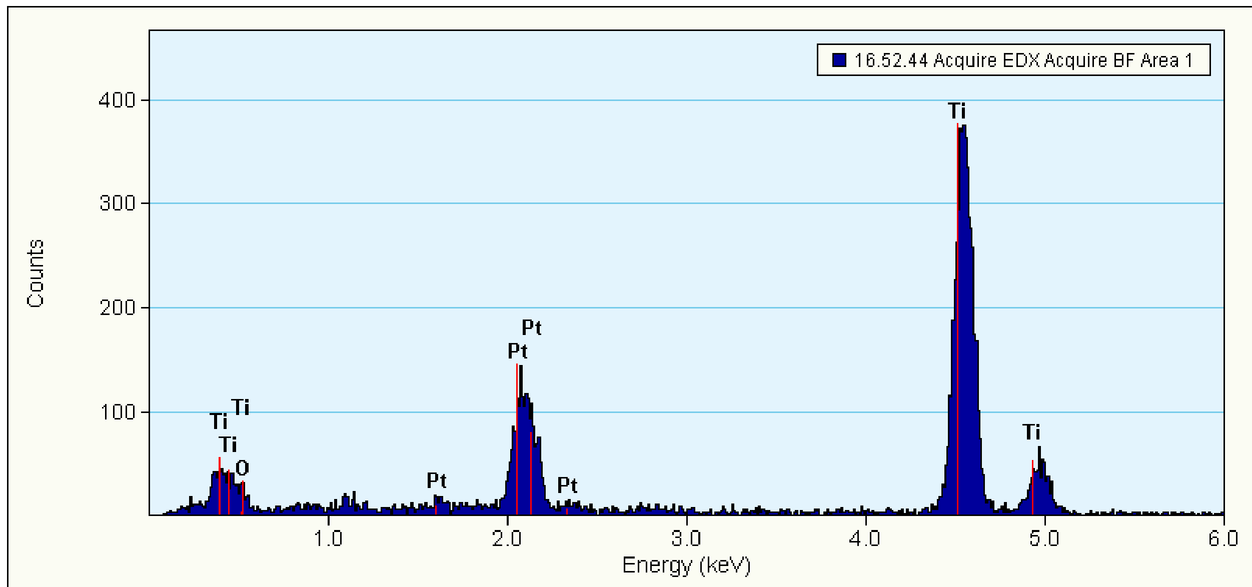

Figure 3.13: The metrology analysis of the fabricated device showing a TEM cross-sectional image of MIM junction showing the TiO_2 interfacial layer in between Ti (top) and Pt (bottom) electrodes.

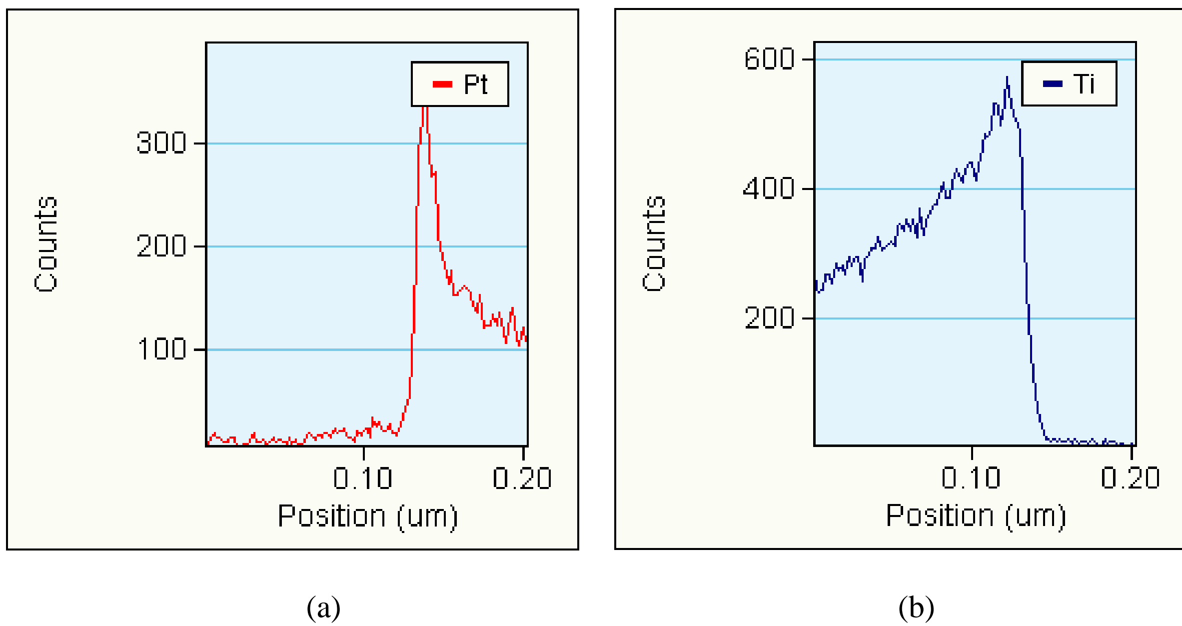

Figure 3.14: The metrology analysis of the fabricated device showing an EDX spectrum verifying the composition of the (Pt-TiO_2-Ti) MIM tunnel junction.

3.6 Summary

In this chapter, the tools used to fabricate the MIM diode are described in detail. In addition, the general fabrication process and material consideration was also discussed. The UV lithography process discussed in section 3.1.1 was used to fabricate the micro sized devices. The sub-micro (nano-size) devices were fabricated by the e-beam process discussed in section 3.1.1.2. Atomic layer deposition (ALD) detailed in section 3.1.3.2 was used to deposit thin film of metal oxides as tunnel layer while sputtering and electron beam evaporation was used to deposit metal thin films for electrodes. By employing the atomic layer deposition (ALD) process, MIM diodes with a variety of junction areas ranging from 3μm×3μm to 100μm×100μm were successfully fabricated. The ALD technique offers a superb uniformity, low defect density, and precise thickness control of the tunneling insulator layer. Hence, several ultra-thin insulator materials (e.g., Al_2O_3, TiO_2 and HfO_2) with varied thicknesses have been concurrently explored.

Also in this chapter, the device fabrication process and the metrology techniques was described in detail. The substrate cleaning procedure, which is a necessary step to remove the organic and inorganic contaminant was also discussed. Such contaminants include oily layer, organic layer(s), and light and heavy metallic ion layer. In section 3.2.1.3 the mask design layout and manufacturing was detailed. The step-by-step process flow and fabrication procedures were discussed in section 3.2.1.5. The thickness of the thin-film tunnel layer and the fabricated diodes sizes were verified by the metrology analysis, which was discussed in section 3.2.2.

CHAPTER 4: DC CHARACTERIZATION

The DC characteristic of a MIM tunneling diode is its essential performance metric. A DC measurement is conducted primarily to obtain the current (I) vs. voltage (V) or resistance vs. voltage characteristics by providing a voltage or current stimulus and measuring current or voltage reaction. It is a basic electric measurement and a fundamental way to discover behavior and characterize microelectronics devices. In this study, DC characterization was used to determine the operational voltage and functionalities of the device after fabrication. Firstly, the measurement setup will be discussed. Thereafter, the *I-V* and other MIM diode performance parameters that were extracted from the measured *I-V* responses will be discussed, including; differential resistance versus voltage, responsivity versus voltage, asymmetry and nonlinearity versus voltage plots.

4.1 DC Experimental Setup

DC *I-V* characterization was performed on the fabricated MIM diode using the HP4145 semiconductor parameter analyzer along with a probe station. Fig. 4.1 shows the characterization setup. The device's DC characterization was performed under this two-part scheme.

HP4145 is an extremely useful tool for characterizing semiconductor devices. The MIM diodes were characterized to evaluate their characteristics such as *I-V* responses. A Hewlett Packard 4145 was connected in series with a micromanipulator probe station for preliminary characterization of the selected devices. The testing setup consists of a collection of high-precision current and voltage sources and meters, along with software to drive the whole

operation. At the completion of the sweep measurement, the HP plotter displays the result on the control computer monitor. The measurement tool was connected to the computer through a General Purpose Interface Board (GPIB). The *I-V* responses of the diodes were obtained by sweeping the voltage in both positive and negative polarities.

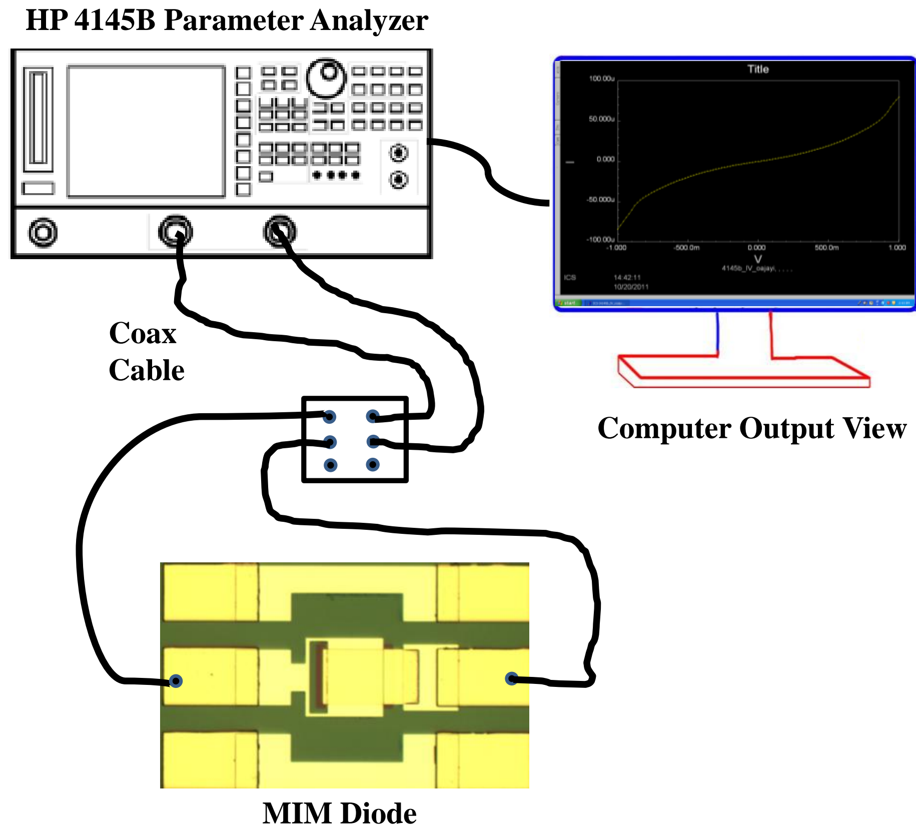

Figure 4.1: A simplified schematic illustration of DC characterization scheme with a HP4145B semiconductor parametric analyzer

The DC measurement was performed on batch fabricated MIM diodes with various junction areas ranging from 5μm × 5μm to 100μm × 100μm. The *I-V* measurements were performed at room temperature.

4.1.1 Characteristics of Pt-HfO_2-Ti MIM Diodes with 2nm-thick Tunnel Layer

I-V characteristic plots of the various micro-fabricated Pt-HfO_2-Ti MIM diodes with 10μm × 10μm to 30μm × 30μm junction areas are shown in Fig. 4.2 (a). The responses were obtained when devices were biased with a sweep voltage of ±0.8V. The devices with smaller junction sizes demonstrated slightly lower current amplitude as compared to that of the bigger devices. These diodes with a single layer of 2nm-thick HfO_2 tunnel material exhibited a limited degree of nonlinearity and asymmetry peaked around +0.4V and -0.5V, respectively. The asymmetry is a result of the usage of different metal electrodes materials. Fig. 4.2 (b) – (d) present the measured and extracted DC characteristics of various junctions including the differential resistance, the nonlinearity, and the asymmetry. These parameters as shown in Table 4.1, show the key performance aspects of the diodes. Fig. 4.2 (b) shows that smaller MIM devices have higher differential resistance along with higher responsivity, as compared to larger devices. To a certain extent, the nonlinearity shown in Fig. 4.2(c) for these devices show area dependence, and asymmetry as seen in Fig. 4.2(d) reveal similar trends for all sizes.

Table 4.1: The definittion of the key performance parameters for evaluating MIM diodes.

Asymmetr y	Nonlinearit y	Curvature Coefficient [93, 95, 144]
$\eta = \left(\frac{I_p}{I_n}\right)$	$\chi = \left(\frac{dI}{dV}\right) / \frac{1}{V}$	$\gamma = \left(\frac{d^2I}{dV^2}\right) / \frac{dI}{dV}$

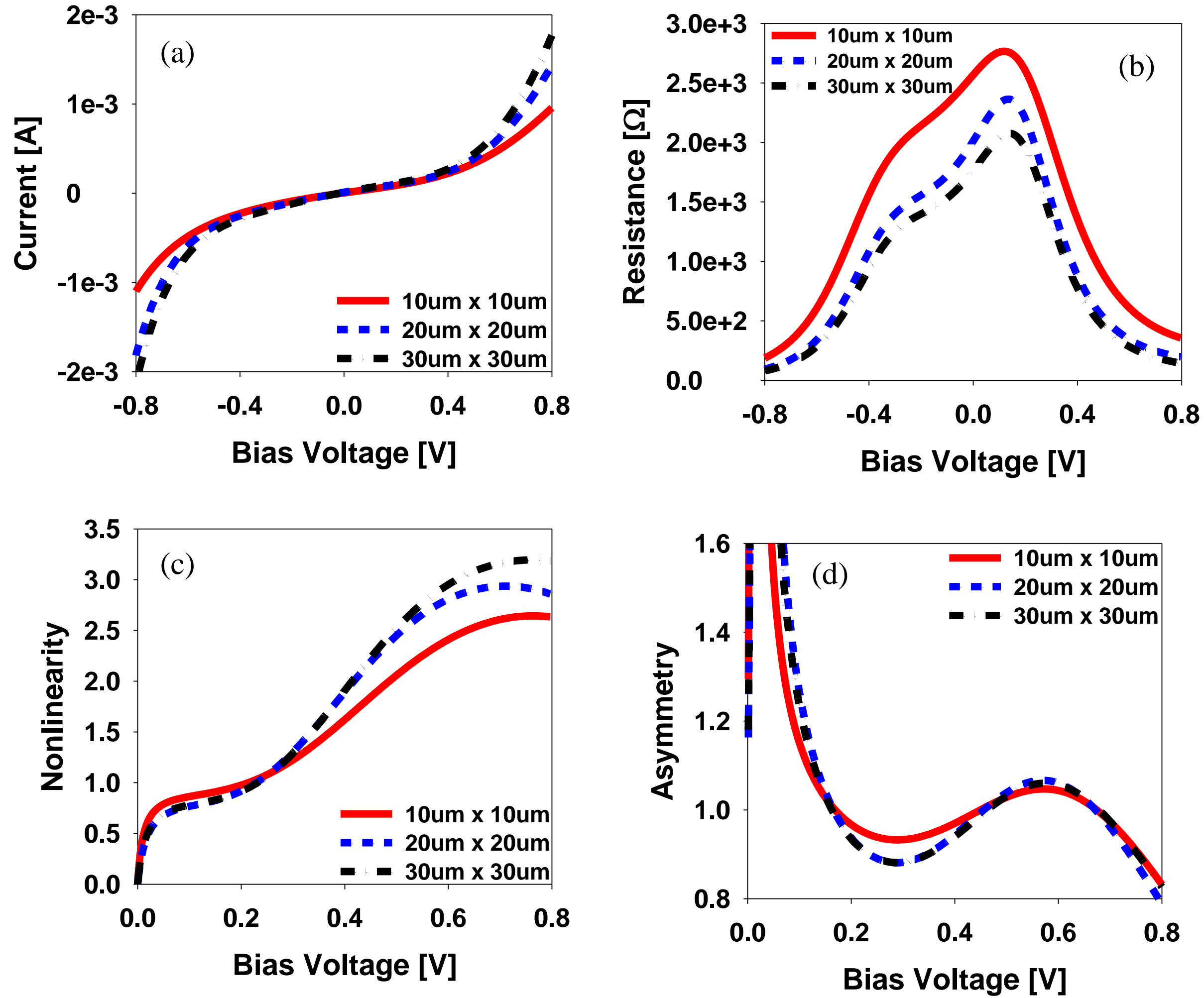

Figure 4.2: Measured DC *I-V* characteristics of Pt-HfO_2-Ti MIM diodes with 2nm-thick tunnel layer and different junction area. (a) Current vs. Voltage relationships, (b) Differential resistance vs. Voltage; (c) Nonlinearity vs. Voltage; and (d) Asymmetry vs. Voltage relationships.

Table 4.2: A summary of measured characteristics of Pt-HfO_2-Ti MIM diodes with 2nm-thick HfO_2 tunnel layer and different junction sizes ranging from 10μm×10μm to 30μm×30μm.

Junction Area Configuration	Zero-Bias Diff. Resistance	Calculated Peak Responsivity
10μm × 10μm	2800 Ω	4900 V/W
20μm × 20μm	2500 Ω	4000 V/W
30μm × 30μm	1800 Ω	3500 V/W

4.1.2 Characteristics of Pt-HfO_2-Ti MIM Diodes with 3nm-thick HfO_2 Tunnel Layer

In this work, Pt-HfO_2-Ti MIM diodes with a 3nm-thick HfO_2 tunnel layer were fabricated, measured and characterized. From the *I-V* measurement, the current densities vs. voltage responses for devices with different junction sizes varying from 10μm × 10μm to 30μm × 30μm contact areas are shown in Fig. 4.3(a). The nonlinearities of these devices was observed in between the bias voltage of ±0.5V.

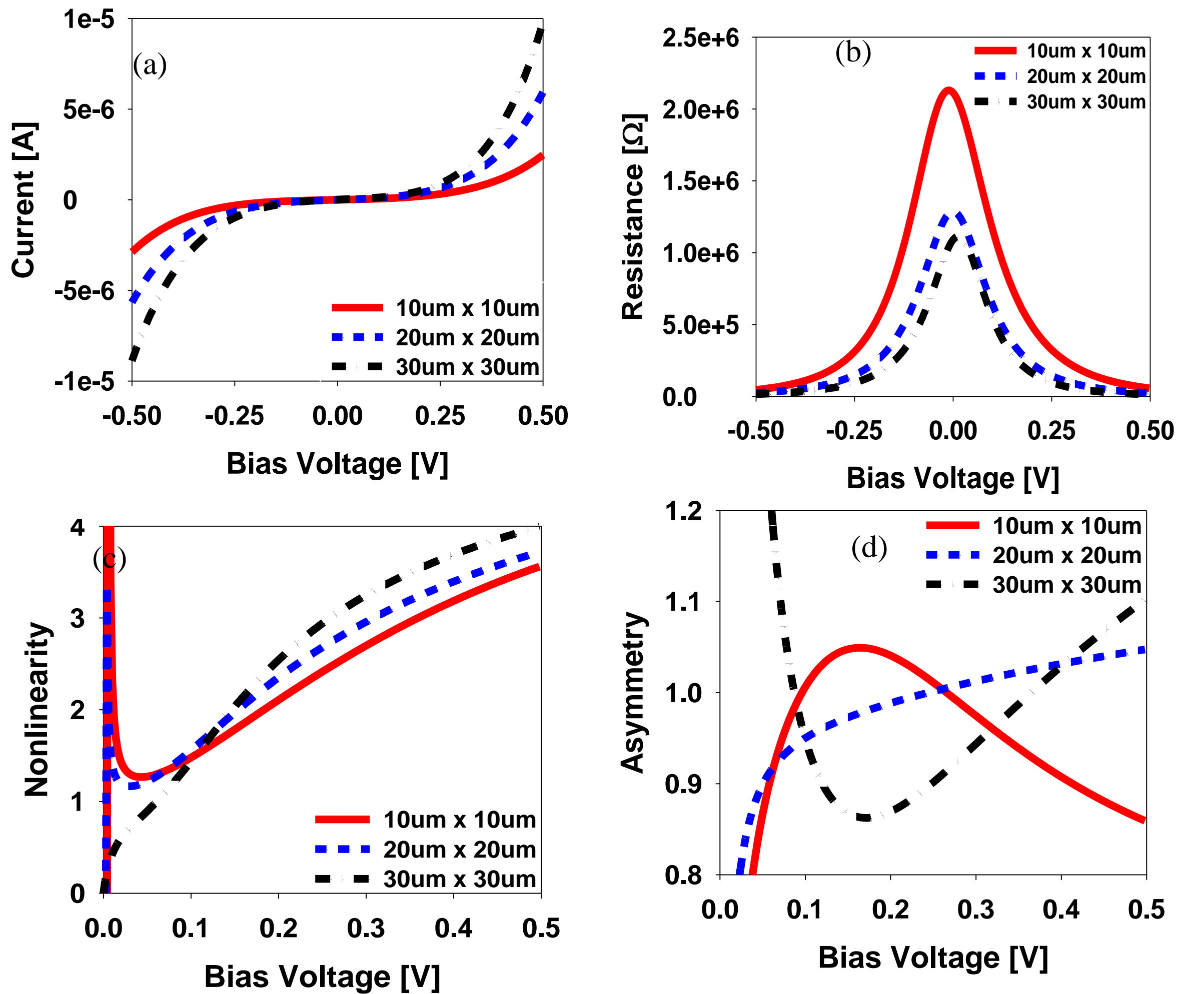

Figure 4.3: Measured DC *I-V* characteristics of Pt-HfO_2-Ti MIM diodes with 3nm-thick tunnel layer but different junction sizes. (a) Current vs. Voltage; (b) Differential resistance vs. Voltage; (c) Nonlinearity vs. Voltage; and (d) Asymmetry vs. Voltage relationships.

The reverse and forward currents in the range of tens of 10^{-7}A/µm^2 were measured. Fig. 4.3(b) – (c) present the key figure of merit of these diodes as defined by differential resistance, asymmetry, and nonlinearity. It was observed that these devices exhibited higher differential resistance as compared to that of the devices with a 2nm tunnel layer discussed in the previous section. Also, these devices exhibited a pattern of area dependency in its nonlinearity and limited asymmetry probably due to the usage of different electrode materials.

Table 4.3: A summary of measured characteristics of Pt-HfO_2-Ti MIM diodes with 3nm-thick HfO_2 tunnel layer and different junction sizes ranging from 10µm×10µm to 30µm×30µm.

Junction Area Configuration	**Zero-Bias Diff. Resistance (MΩ)**	**Responsivity (V/W)**
10µm × 10µm	2.15	8×10^6
20µm × 20µm	1.2	5×10^6
30µm × 30µm	1.10	1.3×10^6

4.1.3 Characteristics of Pt-TiO_2-Ti MIM Diodes with 3nm-thick TiO_2 Tunnel Layer

Another thin film material that is also studied and used as a tunnel layer in the fabrication of the MIM diode is TiO_2. This high-*k* material has been actively studied. As a result, it was viewed as a major candidate for some memory capacitors and transistors [145, 146]. The TiO_2 (dielectric constant ε_r =80, band gap E_G=3.5eV) employed in the fabrication of these diodes is discussed in this section. According to Wilk et al. [141]. TiO_2 exhibits electrical properties that are different from other metal oxide in group IV. The soft phonons formed from the Ti ions result in the material's high permittivity. Thus, the Ti–O bond creates a carrier trap and high leakage paths [141]. These properties of TiO_2 contribute to the characteristic difference of the devices manufactured with HfO_2 and TiO_2. Fig. 4.4 presents the *I-V* characteristics for devices

with 10μm × 10μm to 30μm × 30μm contact areas. The devices were measured by sweeping the bias voltage between ±0.3V. A minimal degree of nonlinearity and asymmetry was observed for these devices. Fig. 4(b) – (d) presents differential resistance, asymmetry and nonlinearity curves extracted from the *I-V* data. Table 4.4 summarizes the value of the differential resistance with the calculated responsivities.

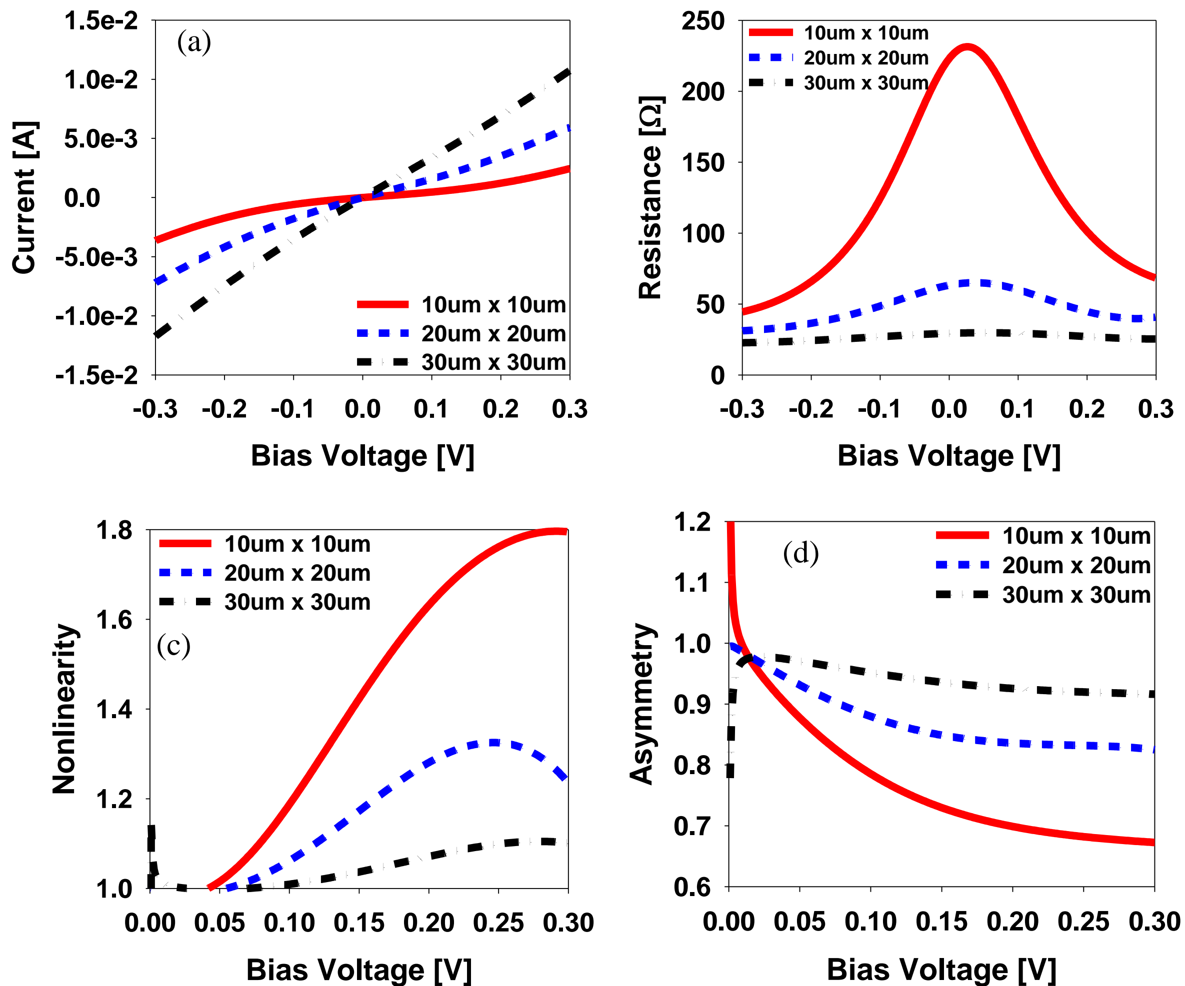

Figure 4.4: Measured DC characteristics of Pt-TiO_2-Ti MIM diodes with 3nm-thick tunnel layer but different junction sizes. (a) Current vs. Voltage relationship; (b) differential resistance vs. voltage relationship; (c) nonlinearity vs. voltage relationship; and (d) asymmetry vs. voltage relationship

Table 4.4: A summary of measured characteristics of Pt-TiO_2-Ti MIM diodes with 3nm-thick TiO_2 tunnel layer and different junction sizes ranging from 10μm×10μm to 30μm×30μm.

Junction Area	**Zero-Bias Differential Resistance**	**Peak Responsivity**
10μm×10μm	230 **Ω**	3000 V/W
20μm×20μm	65 **Ω**	300 V/W
30μm×30μm	29 **Ω**	40 /W

4.1.4 Characteristics of Pt-TiO_2-Ti MIM Diodes with 4nm-thick Tunnel Layer

Another batch of MIM diodes was fabricated with 4nm-thick TiO_2. Fig. 4.8 shows the current density versus voltage, while Fig. 4.9 presents the differential resistance, responsivity, asymmetry, and the nonlinearity plot versus voltage.

Table 4.5: A summary of measured characteristics of Pt-TiO_2-Ti MIM diodes with 4nm-thick TiO_2 tunnel layer and different junction sizes ranging from 10μm×10μm to 30μm×30μm.

Junction Area	**Zero-Bias Differential Resistance**	**Peak Responsivity**
10μm×10μm	700 Ω	500 V/W
20μm×20μm	300 Ω	250 V/W
30μm×30μm	122 Ω	150 V/W

In summary, the following was observed for devices with a single tunnel layer:

- The MIM diode with a smaller junction size has higher junction resistance in comparison to devices with larger junction sizes.
- The tunnel layer thickness reduction drastically lowers the value of the MIM diode junction resistance.

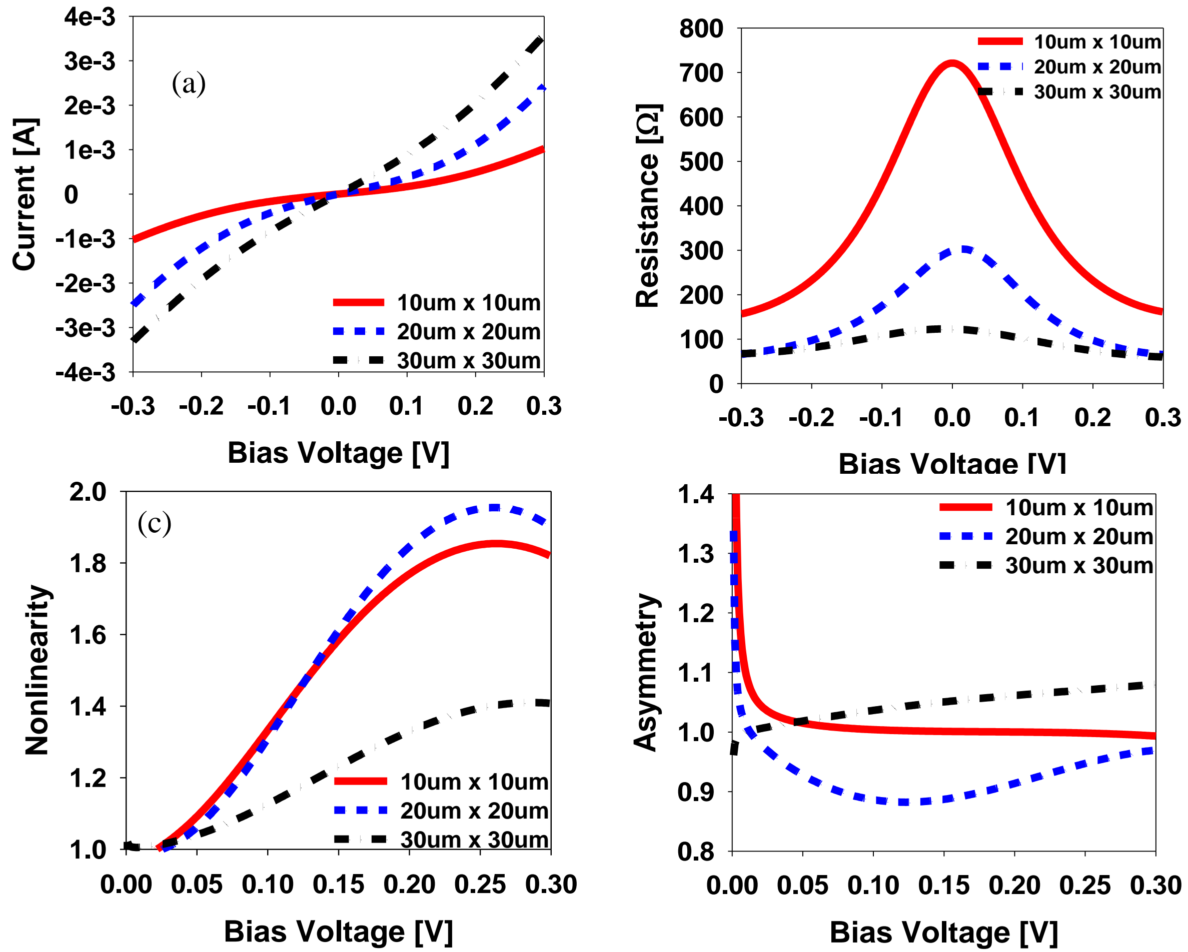

Figure 4.5: Measured DC characteristics of Pt-TiO_2-Ti MIM diodes with 4nm-thick tunnel layer but different junction sizes. (a) Current vs. Bias Voltage, (b) differential resistance vs. Bias Voltage; (c) nonlinearity vs. Bias Voltage; and (d) asymmetry vs. Bias Voltage.

- The rate of change in the nonlinearity is strongly impacted by the barrier height [147].
- As shown in Figure 4.3 and Figure 4.4, it is evident that the composition of the tunnel layer material contributes to the tunneling behavior.
- As compared to devices with TiO_2 tunnels layer of the same thickness, the identically sized devices with HfO_2 tunnel layers exhibit more pronounced nonlinearity.

- It was observed that the normalization plots of current density vs voltage (J-V) were different for the MIM diodes with respect to the area, this could be a result of imperfection in the fabrication process that need to be investigated in the future work.

Several prior works [144, 148] have explored the employment of dissimilar metal electrodes with disparate work functions in an MIM diode, to achieve strong nonlinearity and asymmetry. The experimental results in this work clearly indicate that other factors, such as MIM junction areas, the tunnel layer thickness and tunnel material composition also play a strong role. In addition, other physical properties such as permittivity, barrier height [149], thermal stability, interface quality, device geometry, and film morphology [150] can be exploited to influence the performance of an MIM diode, as evidenced by the results shown in Figures 4.2-4.5.

The *I-V* curves of the Pt-oxide-Ti MIM diodes are shown in Figures 4.2(a), 4.3(a), 4.4(a) and 4.5(a) for 2nm HfO_2, 3nm of HfO_2, 3nm of TiO_2, and 4nm of TiO_2, respectively. By comparing devices with 10µm×10µm, 20µm×20µm, and 30µm×30µm junction areas, the strong correlation between the junction area and the operation current was observed. It is clear that as the junction area increases, so too does the current from the *I-V* measurements. The tunneling layer's thickness and the electrical properties contribute to the variation in magnitude of the current amongst devices [151]. For example, the MIM diodes for both 2nm and 3nm HfO_2 and 3nm and 4nm TiO_2 tunneling layers exhibited a lower current as thickness increased. A three-order magnitude difference in current was observed for devices with different tunnel layers of the same 3nm thickness as shown in Figures 4.3(a)-4.4(a). In part, this can likely be attributed to the different electrical properties of the oxide materials, such as the bandgap or permittivity.

Likewise, the value of the extracted junction impedance is strongly correlated with the thickness and material of the tunneling layer. The first derivative of the measured *I-V* response reveals the junction resistance of the diode, which is plotted accordingly in Figures 4.2(b), 4.3(b), 4.4(b), and 4.5(b). For instance, the zero-bias junction resistances of MIM diodes of identically sized junction of 30μm×30μm with 2nm-HfO_2, 3nm-HfO_2, 3nm-TiO_2, and 4nm-TiO_2 tunneling layers are 1.8kΩ, 1.1MΩ, 29Ω, and 122Ω, respectively. The direct comparison between different oxide materials of the same thickness reveals that the electrical properties, such as permittivity and bandgap, of the material are factors that contribute to tunneling in MIM diode. The drastic performance variation of devices with a 1nm difference in tunneling layer thickness can be attributed to the unique physical properties of TiO_2 as compared to other insulators [141]. TiO_2 (permittivity ε_r=80 and bandgap E_G=3.5eV) and HfO_2 (ε_r=25, E_G=5.7eV) are group IV metal oxide [152],[153]. However, TiO_2 typically exhibits different electrical properties from other materials from the group IV according to Wilk et al. [141]. This is due to the effect of soft phonons, which leads to a high permittivity. This phenomenon contributes to the distinct difference in characteristics of devices with TiO_2 and HfO_2 tunneling layers. As seen in Figures 4.3-4.4, the devices with 3nm-thick TiO_2 layer are more susceptible to electron tunneling due to the effective barrier height and the Fermi energy, which results in enhanced electron affinity and the reduced bandgap [154].

In practice, the MIM diode’s performance is often quantified by its responsivity and sensitivity as a key metric for diode rectification performance [29]. Responsivity and sensitivity are determined by the diode’s degree of nonlinearity, which is strongly influenced by the choice of tunneling layer material and its thickness [25, 155]. The nonlinearity performance of the fabricated MIM diodes with HfO_2 and TiO_2 are shown in Figures 4.2(c), 4.3(c), 4.4(c) and 4.5(c).

Though the MIM diode exhibits limited nonlinearity, the peak nonlinearity performance of the HfO_2 (~4) is better than that of the TiO_2 (~2), which shows a quasi-linear response. This can be attributed to the relationship between electron tunneling and the medium bandgap as discussed in [156], as a contributor to the electron mobility in the barrier [151]. Additionally, the MIM diodes with larger junction areas exhibit noticeably less asymmetry around unity over the entire DC bias voltage range as compared to those with smaller junction areas. To improve the performance of diode detector, a higher degree of nonlinearity and asymmetry is necessary.

4.2 Characteristics of Multi-layer MIIM Diode (Pt-HfO_2-TiO_2-Ti)

To improve the nonlinearity of the MIM diode, a multi-layer tunneling structure was introduced. Metal-insulator-insulator-metal diode (MIIM) for example introduces an extra barrier at the interfaces of the two insulators due to their differences in material properties specifically their electron affinities. This led to enhanced asymmetry and nonlinearity properties, hence its responsivity also improved. The tunnel barrier for MIIM diode was designed and tailored by formation of two cascaded barriers with HfO_2 (Ea=2.5eV, ε_r=25, E_G = 5.7eV) and TiO_2 (Ea=3.9eV, ε_r =80, band gap E_G=3.5eV).

The use of different metal electrodes with large work function differences between them assisted in achieving more pronounced asymmetrical response. A high degree of nonlinearity is achieved by the barrier height as a result of the Schottky limit created from the metal-semiconductor contact [140]. The barrier height of the electron (φ_n) tunneling through a Schottky barrier is defined as the difference between the metal work function (Φ_M) and the electron affinity of the insulator (χ_s) (φ_n = . Φ_M - χ_s). Fig. 4.10 shows a simplified cross-sectional schematic of the Pt-HfO_2-TiO_2-Ti MIIM diode and its corresponding energy band diagram, respectively. φ_1, φ_2 and φ_3 represent the barrier heights at the interfaces between stacked

dissimilar materials such as M_1/I_1, I_1/I_2 and I_2/M_2 correspondingly. The MIIM junction is composed of a 150nm of Pt, a 1.5nm of HfO_2, a 1.5nm of TiO_2 and 150nm of Ti stacked layers. With the introduction of another tunnel layer to a MIM device, one extra potential barrier is introduced. Represented in Fig. 4.6(b), shows a double layer MIIM diode a three energy barriers defining the effective tunnel junction. Because of this additional barrier, the nonlinearity of the diode also improved. The MIIM diodes with double insulator layers and different junction areas have been characterized.

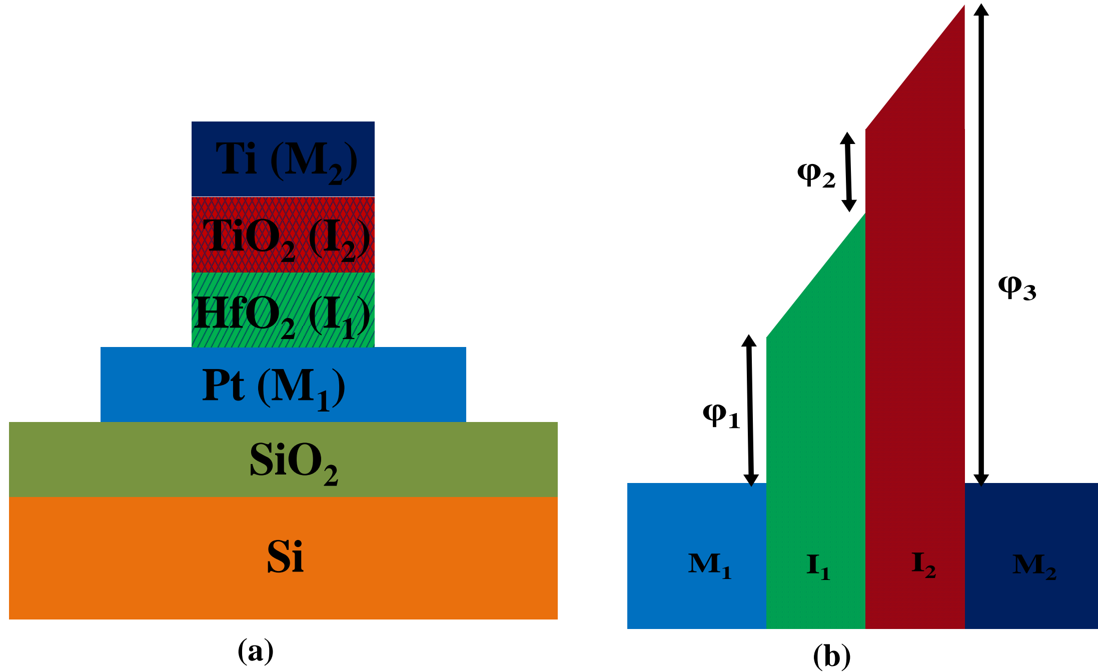

Figure 4.6: (a) A schematic diagram of a MIIM diode; (b) Energy band diagram of a MIIM diode having a cascaded barrier.

The process of fabricating a multi-layer MIM diode is similar to the fabrication process discussed earlier in Chapter 3. The extra step is to deposit multiple ALD layers consecutively under vacuum. The DC characteristics for Pt-HfO_2-TiO_2-Ti MIIM diodes with 20µm×20µm,

10μm×10μm and 5μm×5μm junction areas are shown in Fig. 4.7, Fig. 4.8, and Fig. 4.9, respectively.

Fig. 4.10 presents measured DC characteristics versus bias voltage for more than a dozen of the Pt/HfO_2/TiO_2/Ti MIIM diodes, including current, current density, junction resistance, responsivity, nonlinearity, and asymmetry. Multiple devices were fabricated using the same materials under the same procedures. The DC analysis was performed on all of the devices, and the error and standard deviations were calculated. The measured results from more than 15 devices with 20μm×20μm junction area have been included in Fig. 4.10, thus revealing a fairly small device-to-device variation. This shows that the fabrication procedure employed is very much repeatable and the fabrication is also quite good.

By comparing the measured results of MIM and MIIM diodes, it was observed that the amplitude of the forward-bias and the reverse bias currents of a MIM diode (nA range) is generally greater than the current of a MIIM diode (μA range). The differential resistance of a MIIM diode is higher than that of a MIM diode with the same tunnel layer thickness. While the asymmetry is not noticeable in MIM devices, the MIIM shows much more pronounced levels of asymmetry. The asymmetry in a MIIM diode is more than 10 times greater than that of a typical MIM diode. The nonlinearity is likewise much more pronounced in MIIM diodes. This indicates that MIIM diodes are far superior, in terms of their rectification efficiencies, as compared to the best MIM diodes.

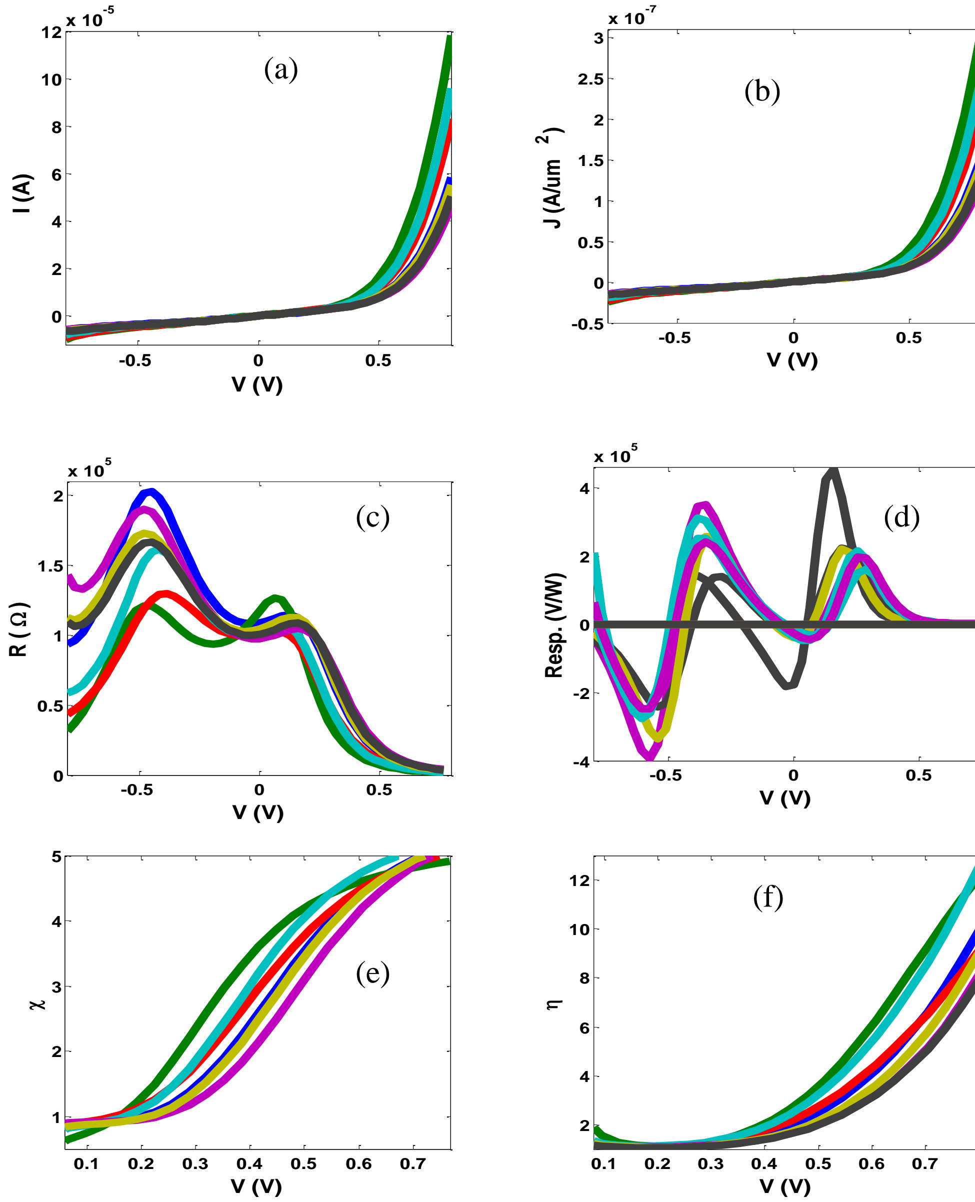

Figure 4.7: Measured DC characteristics of several Pt-HfO_2-TiO_2-Ti MIIM diodes with 20µm×20µm junction area composed of two stacked 1.5nm-thick tunnel layers. (a) Current, (b) current density, (c) the differential resistance, (d) responsivity, (e) nonlinearity, and (f) asymmetry versus bias voltage.

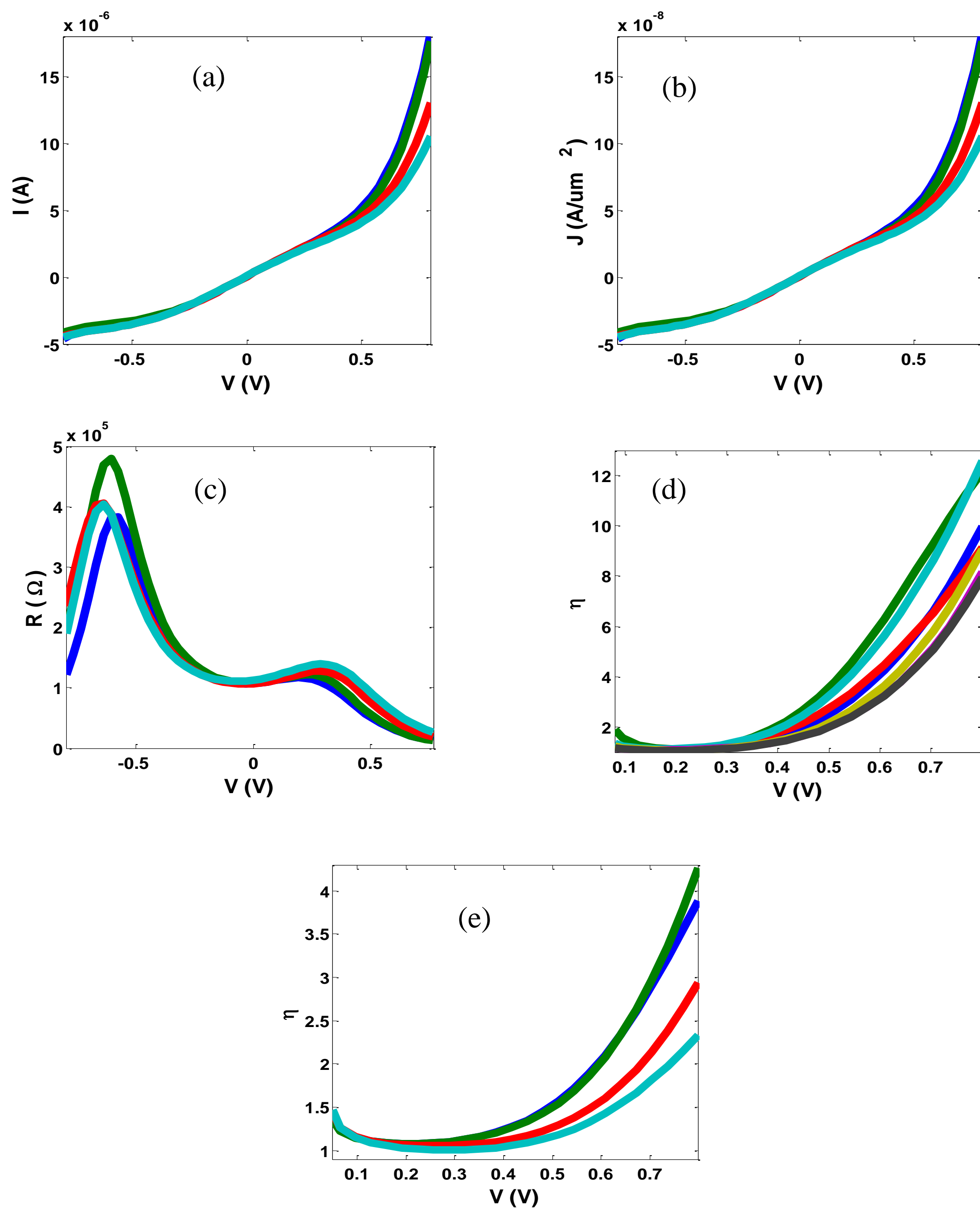

Figure 4.8: Measured DC characteristics for several Pt-HfO_2-TiO_2-Ti MIIM diodes with 10μm×10μm junction areas composed of two stacked 1.5nm-thick tunnel layers. (a) Current, (b) current density, (c) the differential resistance, (d) nonlinearity, and (e) asymmetry versus bias voltage.

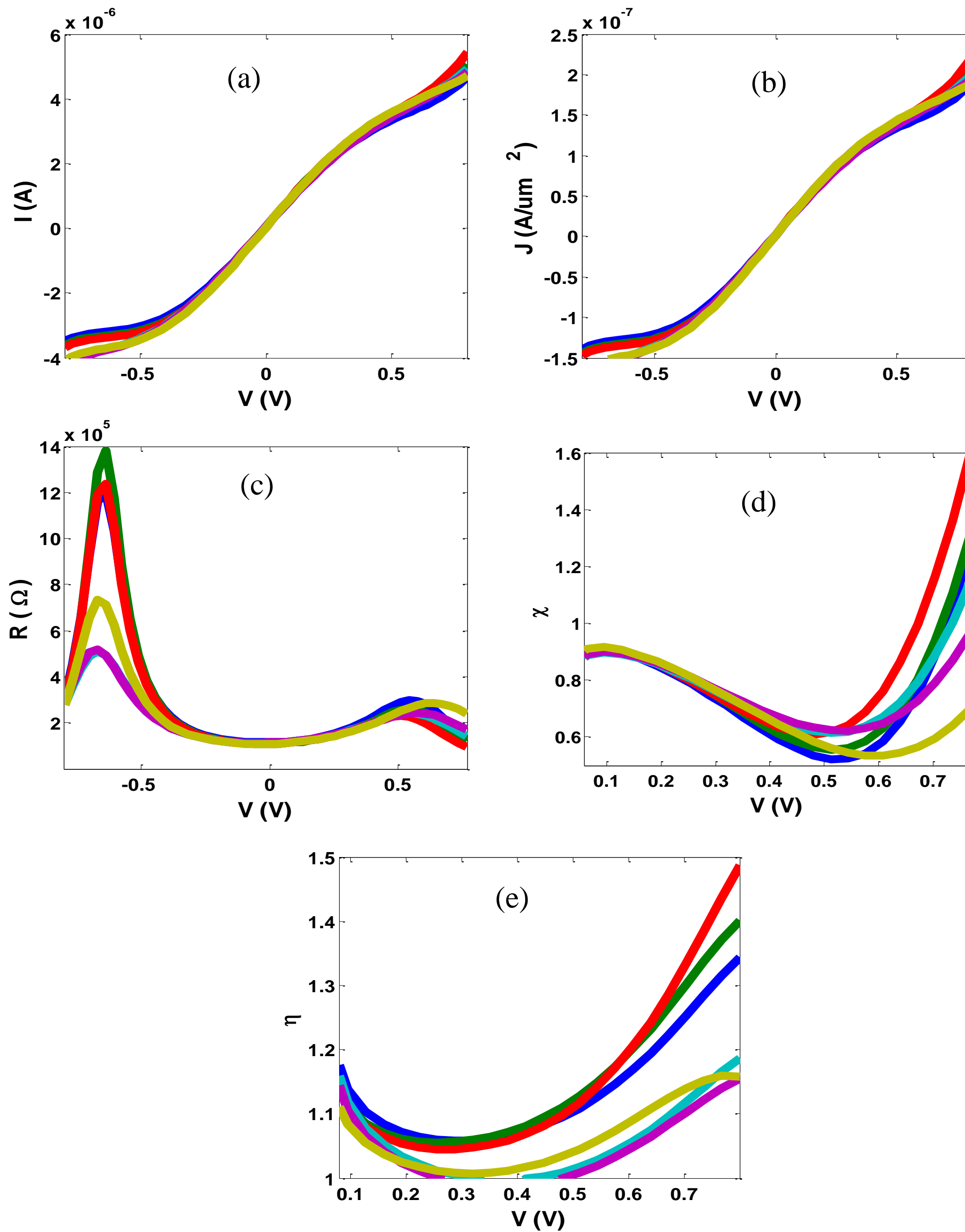

Figure 4.9: Measured DC characteristics for several Pt-HfO_2-TiO_2-Ti MIIM diodes with 5μm×5μm junction areas composed of two stacked 1.5nm-thick tunnel layers. (a) Current, (b) current density, (c) the differential resistance, (d) responsivity, (e) nonlinearity, and (d) asymmetry versus bias voltage.

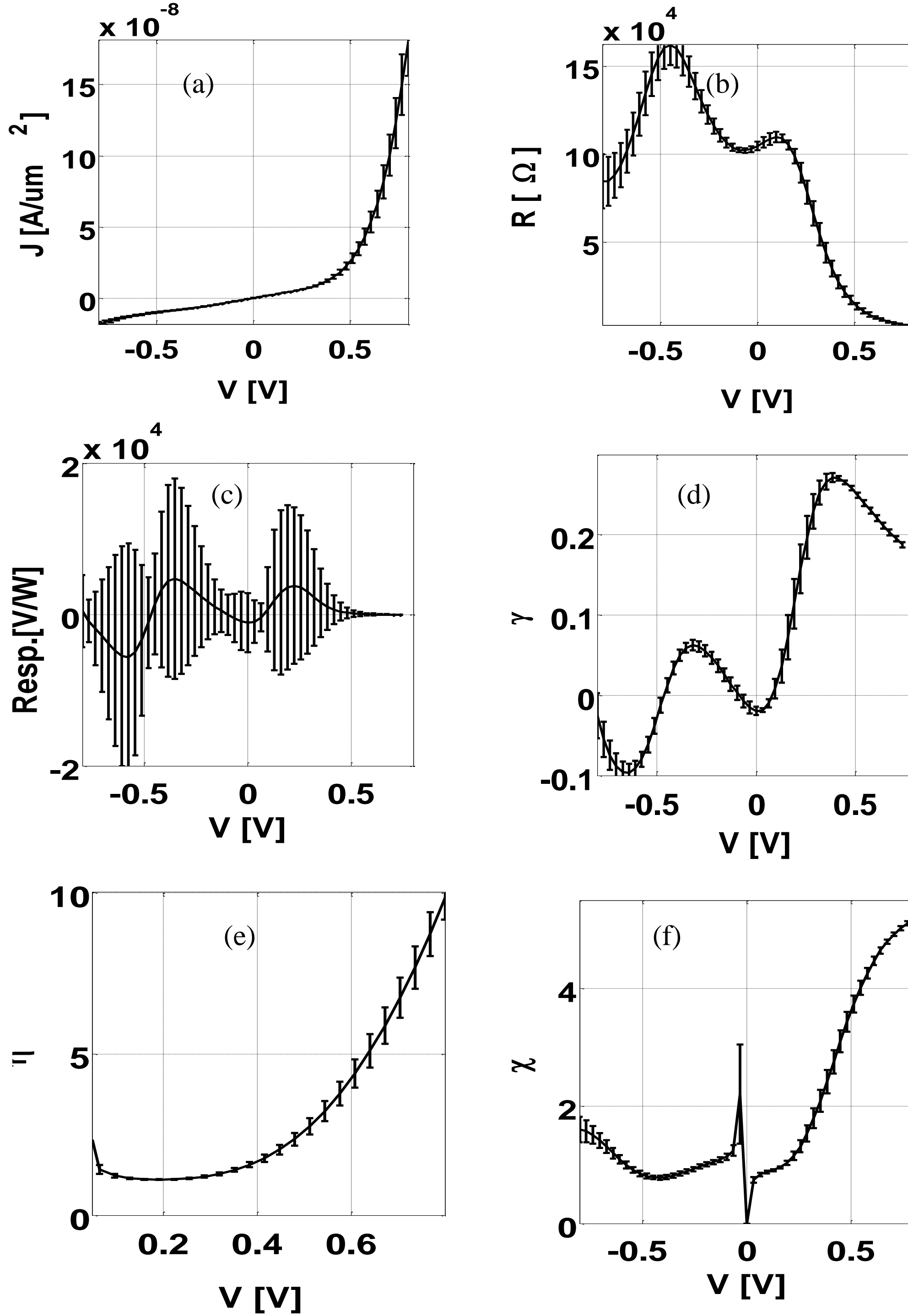

Figure 4.10: Comparison of the measured DC characteristics of 15 Pt-HfO_2-TiO_2-Ti MIIM diodes with 20µm×20µm junction areas composed of two stacked 1.5nm-thick tunnel layers. (a) Current, (b) current density, (c) the differential resistance (d) responsivity, (e) nonlinearity, and (d) asymmetry versus bias voltage

4.3 Barrier Height Extraction

At the metal-insulator interfaces in a MIM diode structure, a change in the equilibrium state occurs that allows electrons to tunnel from one metal to the other when there is enough applied potential to overcome the potential barrier [76, 88, 94]. The current density (*J*) of the MIM arrangement is proportional to the mean barrier height [76, 157]. By accurately extracting the barrier heights, the electron affinity and thickness properties of the tunneling layer can be determined.

An analytical formula reported by Simmons [76] and Meservey [12] for MIM devices, with dissimilar electrodes, was used to model the tunneling mechanism of the diode. The current density of the MIM diode as a function of the bias voltage is calculated by Eq. (4.1). The model predicts tunneling current in the forward and the reverse directions with a trapezoidal barrier of a single tunneling layer [158]. A numerical expression for current density in MIM diode operating in the intermediate bias voltage (i.e., $eV < \phi$) [12] is given by:

$$J = \alpha (V + \gamma V^3) \tag{4.1}$$

where,

$$\alpha = \frac{3}{2}\left(\frac{e}{h}\right)^2 \frac{(2m\phi)^{1/2}}{s} \exp\left(-D\phi^{1/2}\right) \tag{4.2}$$

$$\gamma = \left[\frac{(De)^2}{96\phi}\right] - \left[\frac{De^2}{32\phi^{3/2}}\right] \tag{4.3}$$

$$D = 4\pi S \frac{(2m)^{1/2}}{h} \tag{4.4}$$

The effective mean barrier height is given by:

$$\phi = (\phi_1 + \phi_2 - eV)/2 \tag{4.5}$$

where m, e, h, and S represent electron mass, the charge of an electron, Planck's constant, and the thickness of the insulating film, respectively. The asymmetric barrier heights, ϕ_1 and ϕ_2, are the asymmetric barrier heights at the interfaces between the electrodes and the tunneling layer. A numerical model based on Eq. 4.1 was developed with the aid of MATLAB and optimized to fit the model prediction to the measured MIM diode results. The effective mean barrier height with the best fitted characteristics was then extracted.

Fig. 4.11 presents the comparison between measured and the modeled predicted results for an MIM diode with the same 20μm×20μm junction area. For each device, the model was accurately fitted against the experimental data to extract the mean barrier height. From this approach, 2.85eV, 1.68eV, 1.04eV and 0.60eV were extracted as the mean barrier heights for the MIM devices with 2nm-thick HfO2, 3nm-thick HfO_2, 3nm-thick TiO_2 and 4nm-thick TiO_2, respectively. Table 4.6 summarizes the key extracted parameters for the MIM diodes with different insulator materials and thicknesses. In particular, it was observed that the mean barrier heights are inversely dependent on the tunneling layer thickness.

Unlike the bulk material properties that have been used to calculate the barrier height (difference between the metal work function and the electron affinity of the insulator [12, 93, 140]) of MIM diode, the approach presented in this work gives an accurate value based on the device measurement. Because of the relationship between the barrier height and the tunneling layer's electron affinity, it was also observed that the thickness of the insulator directly affected the electron affinity, as reported by Tien et al [159].

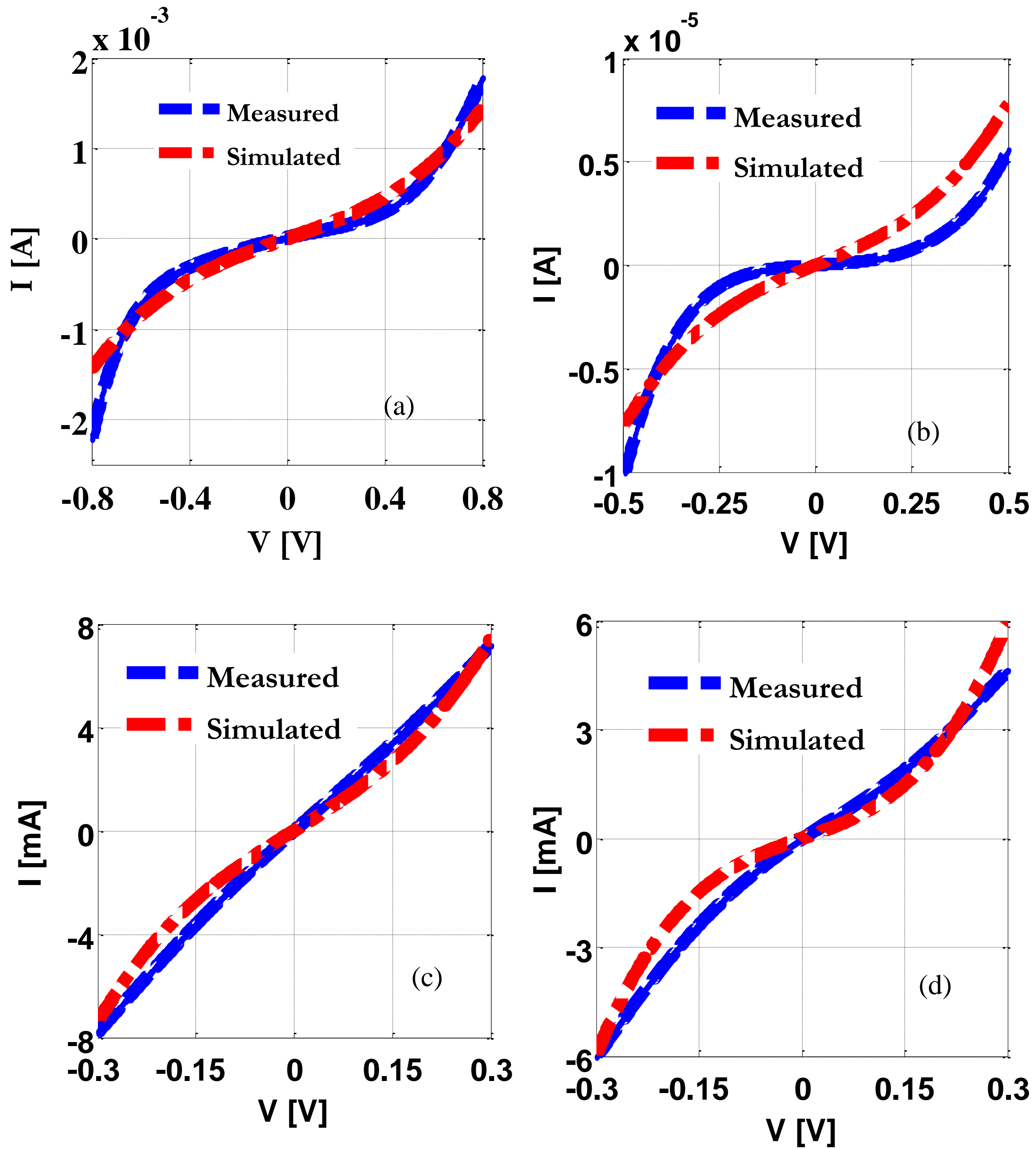

Figure 4.11: Measured MIM diode results vs. modeled predicted I-V responses. (a) Pt-HfO_2-Ti MIM diode with 2nm-thick HfO_2; (b) Pt-HfO_2-Ti MIM diode with 3nm-thick HfO_2; (c) Pt-TiO_2-Ti MIM diode with 3nm-thick TiO_2; (d) Pt-TiO_2-Ti MIM diode with 4nm-thick TiO_2.

Table 4.6: Comparison of parameters extracted from the modeled to measured data.

Junction Material	S(nm)	$\bar{\phi}$ (eV)	R (KΩ)	Reps.(R) (V/W)
Pt-HfO_2-Ti	3±0.2	1.68±0.23	900	~5,000,000
Pt-HfO_2-Ti	2±0.2	2.85±0.58	1.6	~6000
Pt-TiO_2-Ti	4±0.3	0.60±0.09	0.09	230
Pt-TiO_2-Ti	3±0.2	1.04±0.14	0.04	50

4.4 Summary

The current -voltage (*I-V*) characteristics of a variety of microfabricated MIM diode devices were analyzed. Fig. 4.2 showed the DC characteristics of the Pt-HfO_2-Ti MIM diode with 2nm-thin tunnel layer with different junction areas ranging from 10μm×10μm to 30μm×30μm. Fig. 4.3 presented measured *I-V* characteristics for Pt-HfO_2-Ti MIM diode with 3nm-thick tunneling layers for areas ranging from 10μm×10μm to 30μm×30μm. The DC analysis of resistance, asymmetry and nonlinearity was presented in Fig. 4.3 (b), (c) and (d). Tables 4.2 and Table 4.3 summarized the DC characteristics calculated from different junction areas of the 2nm and 3nm tunnel layer thicknesses respectively for Pt-HfO_2-Ti MIM diodes. Fig. 4.4 presented the measured *I-V DC* responses for Pt-TiO_2-Ti MIM diodes with 3nm-thick tunneling layers for devices with 10μm×10μm to 30μm×30μm junction areas. Also, DC characteristics of Pt-TiO_2-Ti MIM diodes with 4nm-thin tunneling layers were presented in Fig. 4.5 for various areas ranging from 10μm×10μm to 30μm×30μm. Tables 4.4 and 4.5 showed the differential resistance and responsivity of the TiO_2 enhanced MIM diode with 3nm-thick and 4nm-thick oxide layers, respectively.

The effects of tunneling layer thickness, bandgap, and permittivity on MIM diode behavior have been examined with respect to its measured DC characteristics. By comparing devices with 30μm×30μm and 10μm×10μm junction areas, it was observed that the current density decreased as the junction area increased. Likewise, the value of the extracted junction impedance strongly correlated with the thickness of the tunneling layer. For instance, the zero-bias junction resistances of MIM diodes of identically sized junctions of 30μm×30μm with 2nm-HfO_2, 3nm-HfO_2, 3nm-TiO_2, and 4nm-TiO_2 tunneling layers were 1800Ω, 1.1MΩ, 29Ω, and 122Ω, respectively.

The asymmetry and nonlinearity was improved by the introduction of multiple stacked tunnel layers. A metal-insulator-insulator-metal (MIIM) diode introduced an extra barrier at the interface between the two stacked tunneling layers due to their different electron affinities. Fig. 4.7, 4.8 and 4.9 presented the measured characteristics for more than 5 Pt-HfO_2-TiO_2-Ti MIIM diodes with the same 20μm×20μm junction area, including current density, junction resistance, nonlinearity, and asymmetry. A minimal device-to-device variation was observed. Fig. 4.10 presented the variations of measured DC characteristics of several devices with the same 20μm×20μm junction area, showing great fabrication toleration and minimum variation.

A comparison of devices with the same 20μm×20μm junction area and 3nm-thick overall tunneling layer thicknesses was presented in Table 4.7. By comparing the measured DC characteristics of MIM and MIIM diodes, it was evident that the amplitude of the current under the same level of forward and reverse bias for MIM diode is greater than that of the MIIM diode. The difference in measured current can be ascribed to the additional barrier height at the insulator-insulator interface. In general, the extracted differential resistance for the MIIM diode is higher than that of MIM diode with an identical total tunnel layer thickness. The superiority of

an MIIM diode over MIM diode lies in its rectification efficiency due to strong nonlinearity and asymmetry. The asymmetry in MIIM diode is more than 10 times greater than that of a typical MIM diode with a single tunneling layer made of TiO_2 or HfO_2. The nonlinearity of MIIM diode is also much more pronounced than that of MIM counterpart.

Table 4.7: Comparison between DC characteristics of MIM and MIIM diodes.

Junction Configuration 3nm-thin	**Zero-Bias Differential Resistance**	**Calculated Peak Responsivity (V/W)**	**Asymmetry**	**Nonlinearity**
Pt-HfO_2-Ti	1 **M**	5×10^6	~2	~1
Pt-TiO_2-Ti	45	40	~0.75	0.95
Pt-HfO_2-TiO_2-Ti	0.1 **M**	~2×10^4	10	5.5

CHAPTER 5: FABRICATION AND CHARACTERIZATION OF MIM/MIIM DIODES WITH NANOSCALE JUNCTIONS

Batches of MIM/MIIM diodes with junction areas as small as 200nm×200nm have been successfully fabricated to operate at millimeters wave and sub-millimeter wave tendencies. The nano fabrication work was carried out by using the e-beam lithography tool of the Center for Nanoscale Materials at Argonne National Laboratory. The MIM/MIIM diodes were batch fabricated on a 4-inch high resistivity silicon wafer by a combination of conventional UV lithography and e-beam lithography.

5.1 Electron Beam

Like the micro-scale devices discussed in chapter 4, the development of the nano-scale devices was designed with four lithography processes. The first three layers were done with electron beam (E-Beam) lithography process, while the last and the fourth layer was patterned by photolithography. The choice of the design, structure, and the dimensions of the MIM tunneling diode discussed in this chapter was carefully done to operate at terahertz frequency. There are four different designs of overlay structure with 200nm×200nm junction presented. The desired pattern was pre-designed using L-Edit CAD layout software. Apart from the last layer, no UV photolithograpy was required for this process. Fig. 5.1 shows the CAD mask layout of the MIM diode designs.

Platinum-Oxide-Titanium MIM diode was fabricated from this process. The first lithography process established the pattern for the platinum (Pt) bottom electrode. Basically,

Methyl-methacrylate (MMA) and poly-MMA (PMMA) were employed to form a double-layer resist, which provided expected deep undercut after development for metal deposition and lift-off. The MMA EL9 was spun on high resistivity silicon at 4000rpm for 45seconds, and baked at 180°C for 180secs. Thereafter, PMMA-A4 was spun also at 4000rpm for 45seconds and baked at 180°C for 180 seconds.

5.1.1 E-Beam Exposure Process

The resist coated wafer was placed into a 100mm customized wafer cassette for JEOL-9300 stage. The cassette was loaded into the system stage. The stage has Faraday cup, absorption electron (AE) detection (for beam size and beam position), and backscattered electron (BE) detection (for mark position detection slot of scanning electron microscope processes). Several system subroutines were carried out for different purposes. Examples of such subroutine included:

- PDEFBE and SUBDEFBE – proper local alignment detection
- DISTBE – field distortion correction
- HEIMAP – height detection.

The L-Edit CAD file was converted to a graphical database system GDSII format. This file was converted to a JBXFILER file by the system, and thereafter was converted to a JOEL52 v3.0 file for pattern writing purposes. The execution files were three types: a) job deck file (.jdf), schedule file (.sdf), and writing schedule-magazine file (.mgn). Table 5.1 summarizes the function of the pattern writing files used by JEOL 9300.

Table 5.1: Description of specific pattern preparation and pattern writing files used by JEOL 9300.

JOB DECK File (.jdf)	**SCHEDULE File (.sdf)**
Connect the tool to the JEOL52 v3.0 pattern file	Specify the wafer cassette window
Set the tool to writing pattern on the wafer	Indicate the calibration file
Set the shot modulation	Specify the base dose
Set the tool to the type of calibration	Direct the tool to job deck file(s) to implement
Indicate the parameter for beam current	Specify the shot pitch

The resist coated wafer was exposed to e-beam radiation at 1000μC/cm^2 for PMMA and 250μC/cm^2 at 100keV. The wafer was thereafter developed by immersing it into a 4-Methyl-2-pentanone mix with isopropanol at 1:3 ratio for 60 seconds. Oxygen descuum was performed on the substrate (160mTorr, 24sccm of O_2 under 20W for 15 seconds). Titanium-7nm/Platinum-80nm was sputtered, followed by a lift-off procedure as follow:

- 1165 remover (n-methyl pyrrolidinone) was heated to 70°C on hot a plate.
- The sample was placed in the heated 1165 remover for more than 3hrs.
- The sample was placed in ultrasonic for 15 seconds.
- The sample was rinsed with acetone, methanol, and isopropanol.

The second layer involved depositing the metallic high-k oxide(s). ALD metal oxides, such as TiO_2, Al_2O_3 and HfO_2, were employed individually for MIM diodes or utilized together to build MIIM or MIIIM tunnel diodes. The table-top atomic layer deposition system manufactured by GEMSTAR-8 housed at CNM was used. The Al_2O_3 layer was deposited at 1Å/cycle nominal rate at 200°C, HfO_2 at 0.9 Å/cycle at 200°C , and TiO_2 at 0.4 Å/cycle at 225°C. For the multi-layer MIM diode, the only extra step was to form the stacked multi-layer tunnel junction through consecutive depositions under vacuum. The sample was then prepared for

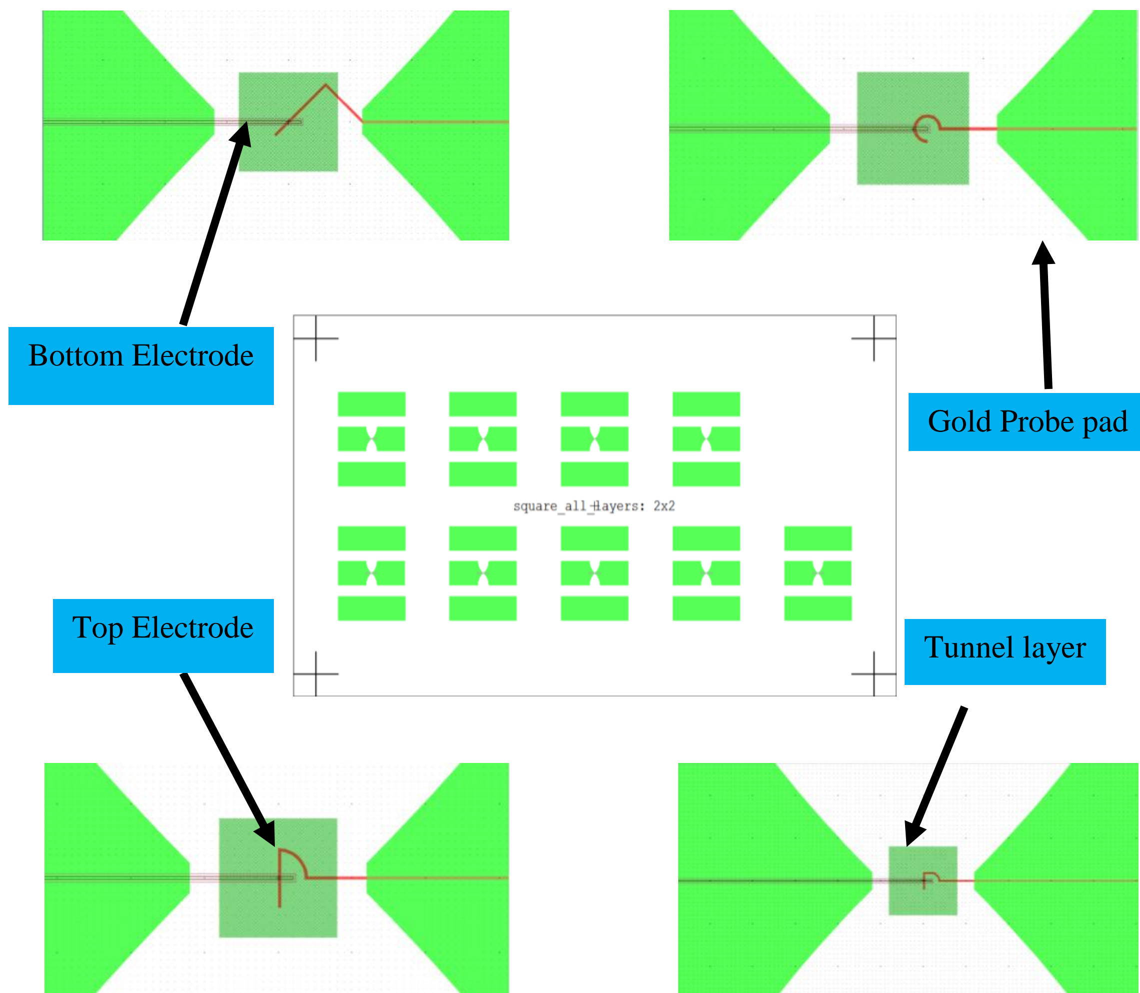

Figure 5.1: Mask layout representation of different design of 200nm×200nm MIM diode

patterning. The process included:

- The substrate was spin coated with ma-N 2403 resist at 3000rpm for 45seconds, to reach a thickness of about 350nm.
- Baked at 95°C for 45 seconds on a hotplate.
- It was later exposed to e-beam radiation at dose of 1000µC/cm^{2}.
- The exposed substrate was developed by immersion in MA-D332-S for 15 seconds.

- The substrate was then rinse in DI water by immersing it in an overflowing, bubbling beaker of DI water for 5 minutes.
- Descuum was subsequently performed on the substrate.

The oxide layer(s) was dry etched in a Plasmalab system 100 manufactured by Oxford Instruments. The recipe included 5sccm of argon (Ar), 10sccm of chlorine (Cl_2), and 10sccm of boron tricloride (BCl_3). The pressure was set to be 5mTorr, along with a temperature of 20°C, ICP power at 500watts, and RF power at 150watts, and a process time of 15 seconds. The residual ma-N 2403 resist after etching was removed with 1165 solvent heated to 70°C on a hotplate.

The top electrode of (Ti/Pt, 60/30) was patterned with a process similar to that of the bottom electrode. The fourth step for defining the gold probe pad layer was done with UV photolithography. The reason for this decision was due to the estimated time to complete pattern writing with direct-write E-Beam lithography, as shown by Equation 5.1 as follow

$$Job\ Time\ Estimate\ (t) = \frac{D \times A}{I} \tag{5.1}$$

where D is the dose (μC/cm^2), I represents the current (A), and A represents the exposure area (cm^2). From this equation, it was clear that it would take more than 48hr to expose one 4” wafer at 200 μC/cm^2. Thus, standard UV lithography is chosen for formation of the probe pads.

The device wafer was spin coated at 3000rpm for 30 seconds with a negative photo resist AZ nLOF 2070 supplied by MicroChemical with 2.5:1 concentration. The coated substrate was soft baked for 60secs at 100°C and exposed with Karl Suss MA6 mask aligner at a 180mJ/cm^2 for 6 seconds. A post-exposure bake was done for 80 seconds at 100°C. It was then developed in CD-26 developer for 120 seconds. 1μm-thick gold layer was evaporated using an e-beam evaporator. The metal liftoff was done by soaking the wafer in acetone.

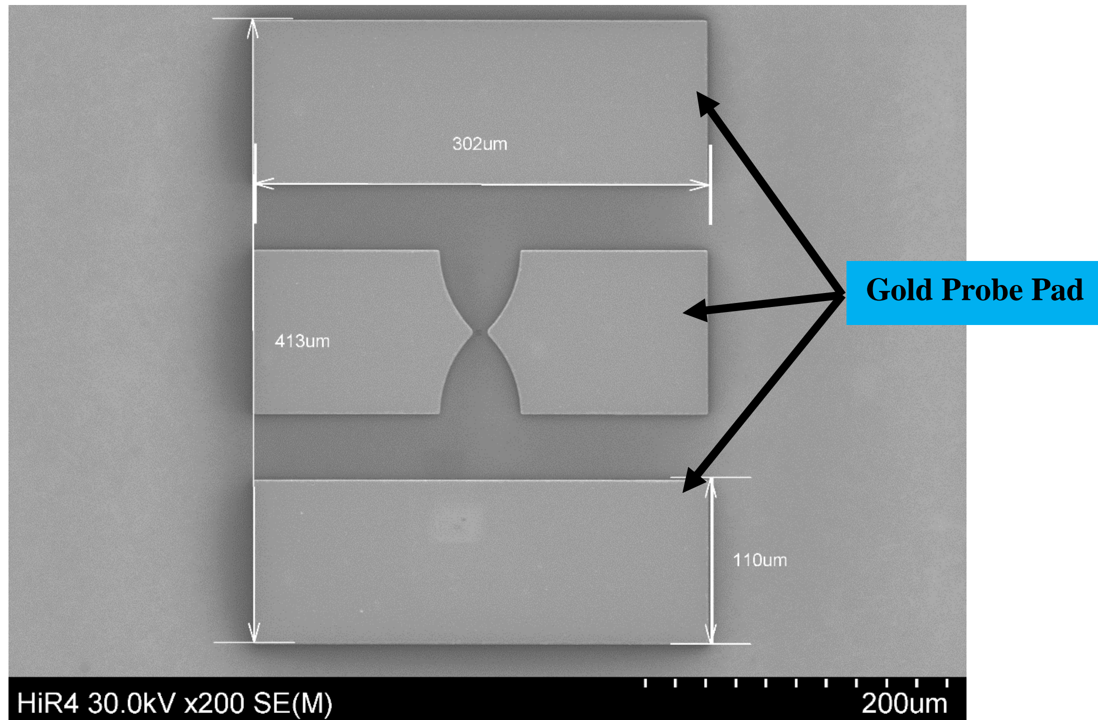

Figure 5.2: Top-view SEM image of a nano-fabricated MIM diode showing large coplanar pads patterned by regular UN lithography for measurement purposes.

5.1.2 Fabrication and Metrology

The surface morphology of the bottom electrode was investigated using an atomic force microscopy (AFM) system. The surface roughness of the patterned platinum bottom electrode is shown in Fig. 5.3. Fig. 5.3(a) and Fig. 5.3(b) show morphology images of the global alignment mark with bigger metal area. The analysis of the AFM scan image shows a mean roughness of 26nm. The degree of roughness was of a concern, especially with the possibility of creating a short circuit as a result of bottom electrode materials penetrating through the thin ALD tunnel junction layer that would be sandwiched between the bottom and top electrodes. The roughness was improved on by depositing the Ti/Pt material under an ultra high vacuum of approximately 10^{-7}Torr at a relatively low deposition rate. The average roughness was improved to 11.7nm

across a 180μm^2 area. The improvement on the material deposition roughness has greatly increased the device fabrication yield and its repeatability.

Devices with different shapes, geometry and dimensions in sub-micron region have been designed and fabricated, as shown in Fig. 5.4. With the cross-finger device structure, MIM diodes with single, double and multiple insulation tunnel layers were fabricated. The fabrication process was similar in all the cases, the only difference being that multiple tunnel layers were deposited concurrently one after the other in MIIM and MIIIM diodes. Several MIM/MIIM devices with single and multiple tunnel layers were fabricated with an identical design.

MIM diodes with Al_2O_3 and HfO_2 as single tunnel layers were successfully fabricated. Also, MIIM junction diodes composed of Pt-Al_2O_3-TiO_2-Ti heterojunction were fabricated. The tunnel layers were made of 1.5nm-thick Al_2O_3 and TiO_2 layer to result in total thickness of 3nm. In the same fashion, the MIIIM diode was comprised of Pt-Al_2O_3-HfO_2-TiO_2-Ti, with 1.5nm-thick of Al_2O_3, HfO_2, and TiO_2 forming a stack of 4.5nm of total tunnel layer thickness. The multiple tunnel layer MIM diode was designed to achieve an electronic band structure base on the electron affinity of the material. The material parameters used in this design are consistent with what has been reported for similar thin films [140, 141]. Al_2O_3 thin film has the electron affinity (χ) of 1.3eV, band-gap (E_G) of 8.8eV, and dielectric constant (κ) of 9; HfO_2 has the electron affinity (χ) of 2.5eV, band-gap (E_G) of 5.7eV, and dielectric constant (κ) of 25. And TiO_2 thin film has the electron affinity (χ) of 3.9eV, band-gap (E_G) of 3.5eV, and dielectric constant (κ) of 80.

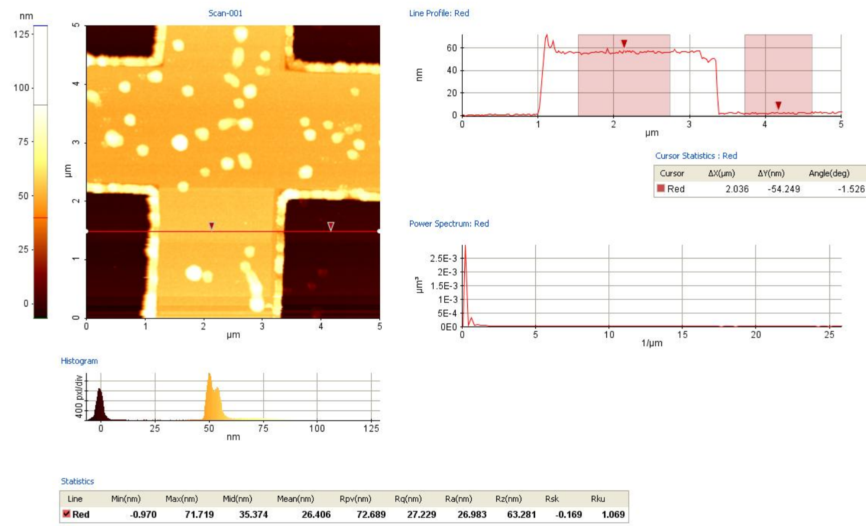

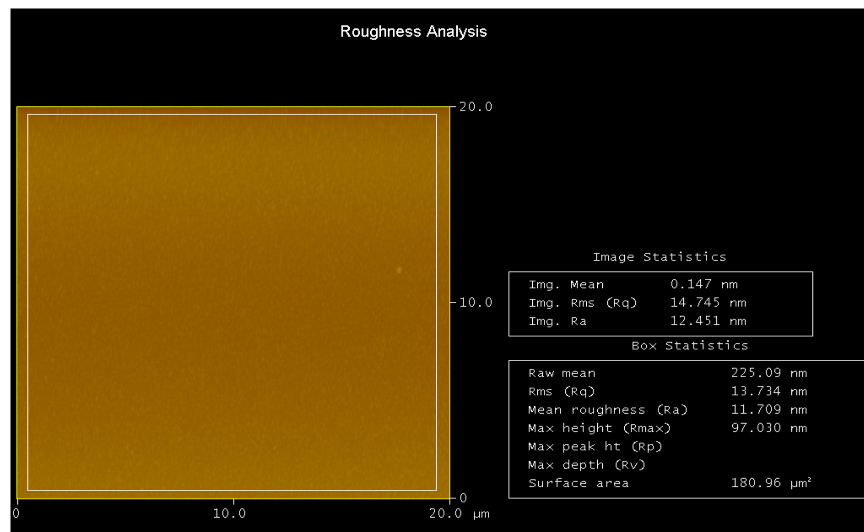

Figure 5.3: To characterize the surface morphology of the bottom electrode, the material roughness measurement was done using a atomic force microscopy (AFM) system.

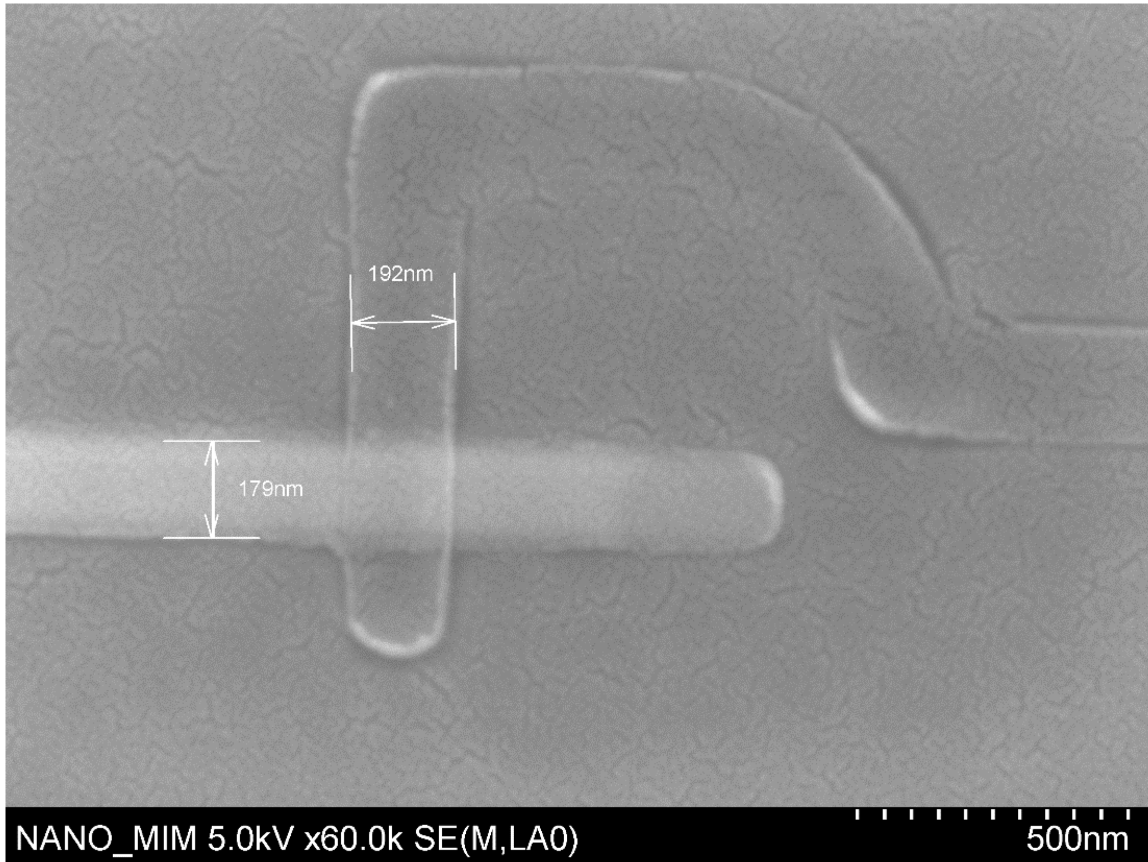

Figure 5.4: The SEM image of the cross-finger structure of the fabricated MIM diodes with nano-scale junctions. As shown, the junction area defined by the overlap of top and bottom electrodes is roughly 200nm×200nm.

5.1.3 DC Characteristics

The measured *I-V* responses of some of MIM/MIIM diodes with 200nm×200nm junction areas were presented in Fig. 5.5 to Fig. 5.10. The DC characteristics of MIM diodes with a single tunnel layer of 3nm-thick alumina (Al_2O_3) is shown in Fig. 5.5 and a device with a hafnia (HfO_2) tunnel layer of 3nm in thickness is shown in Fig. 5.6. The plots include measure current, differential resistances, responsivity, asymmetry, and nonlinearity across the entire range of the bias voltage. It was observed that the key figures of merits (i.e asymmetry and nonlinearity) in

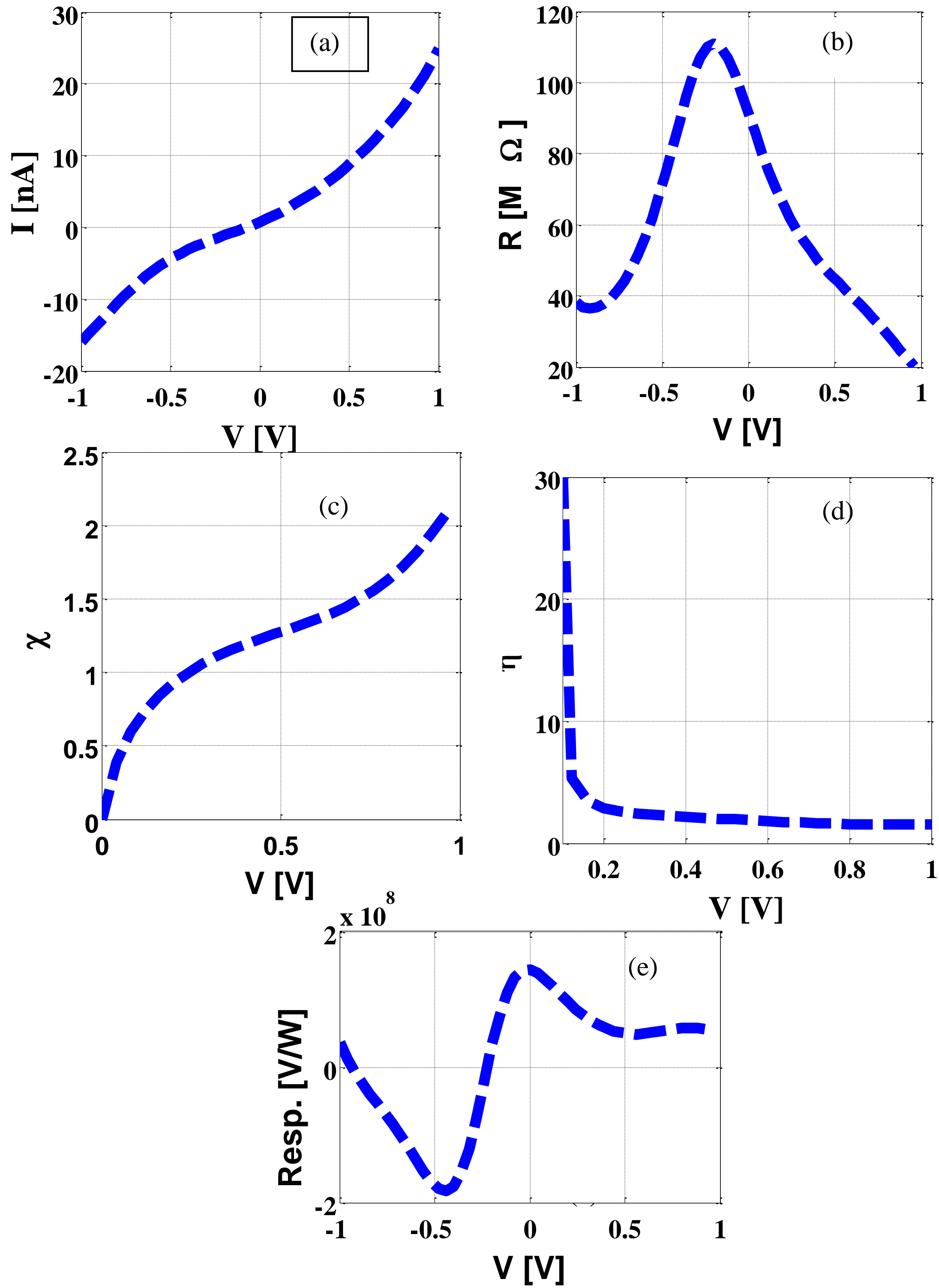

Figure 5.5: Measured DC characteristics of Pt-Al_2O_3-Ti MIM diodes with 3nm-thick tunnel layer of junction size of 200nm×200nm. (a) Current versus bias voltage; (b) differential resistance; (c) nonlinearity; (d) asymmetry; and (e) responsivity

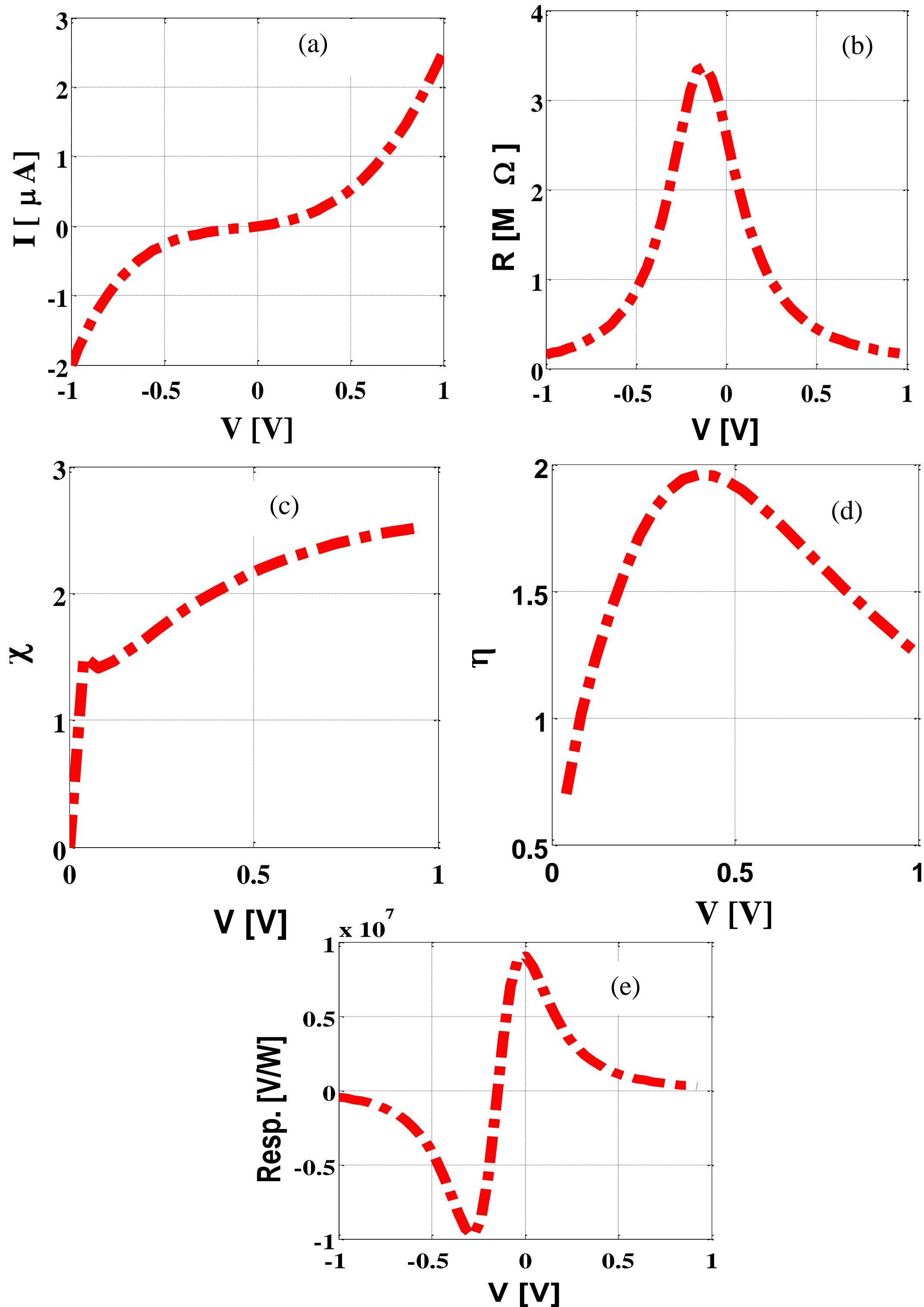

Figure 5.6: Measured DC characteristics of Pt-HfO_2-Ti MIM diodes with 3nm-thick tunnel layer of junction sizes of 200nm×200nm. (a) Current versus bias voltage; (b) differential resistance; (c) nonlinearity; (d) asymmetry; and (e) responsivity.

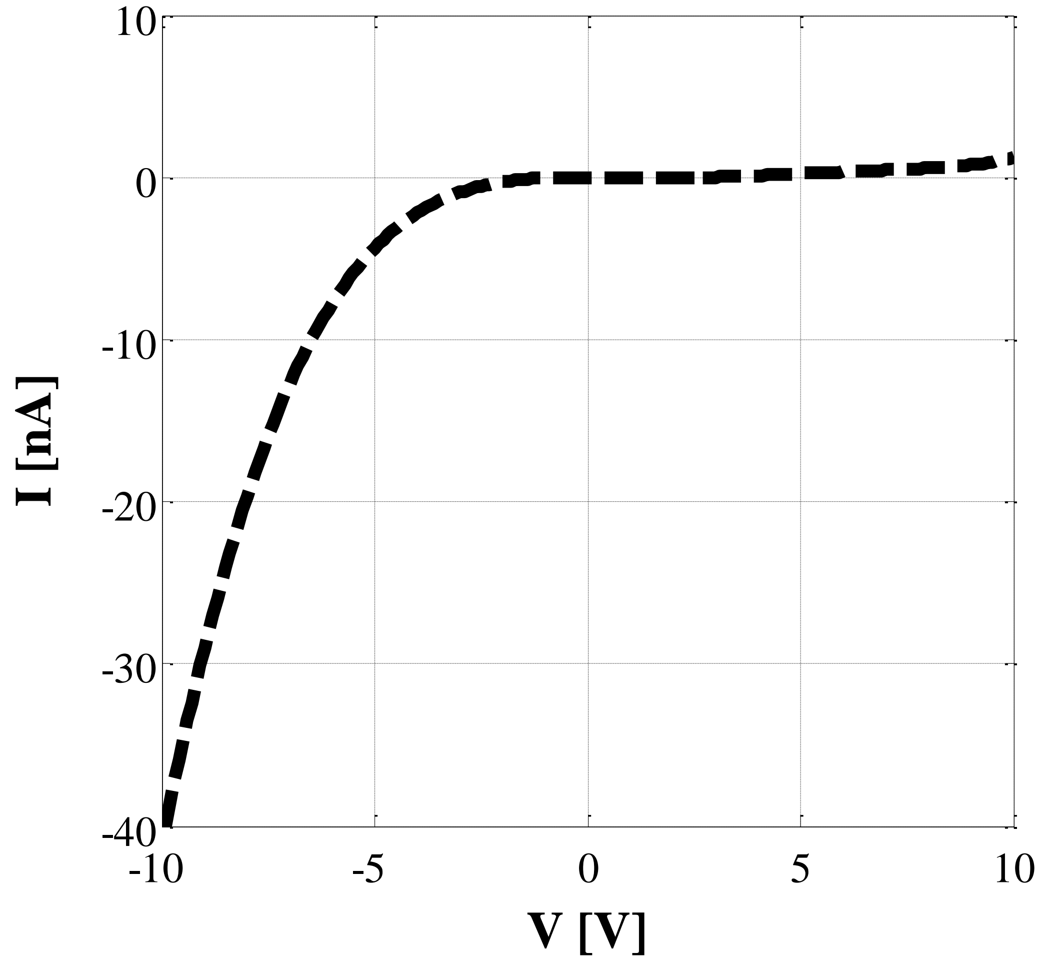

Figure 5.7: Measured DCIV characteristics of Pt-Al_2O_3-TiO_2-Ti MIM diodes with 1.5nm-thick constituent tunnel layers and junction sizes of 200nm×200nm.

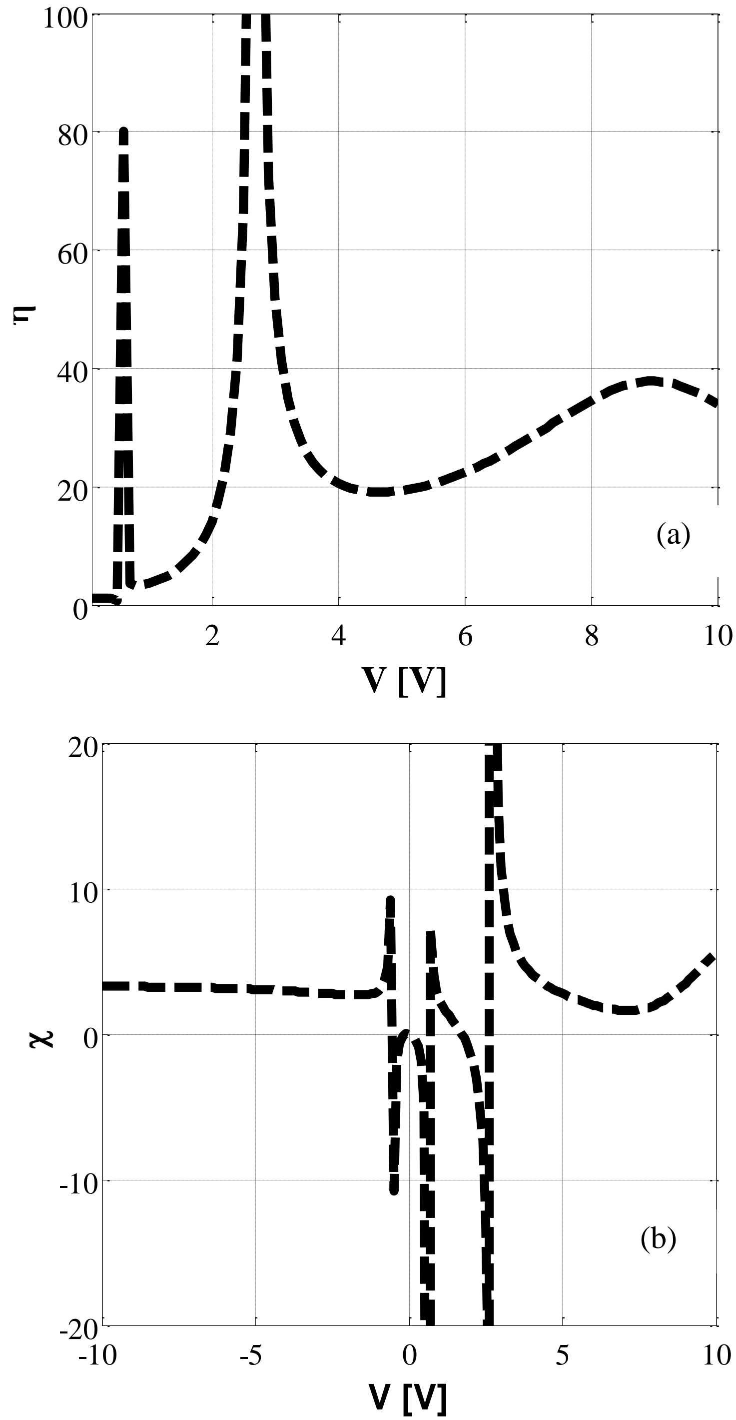

Figure 5.8: Measured DC characteristics of Pt-Al_2O_3-TiO_2-Ti MIM diodes with 1.5nm-thick constituent tunnel layers junction sizes of 200nm×200nm. (a) asymmetry; and (b) nonlinearity versus bias voltage.

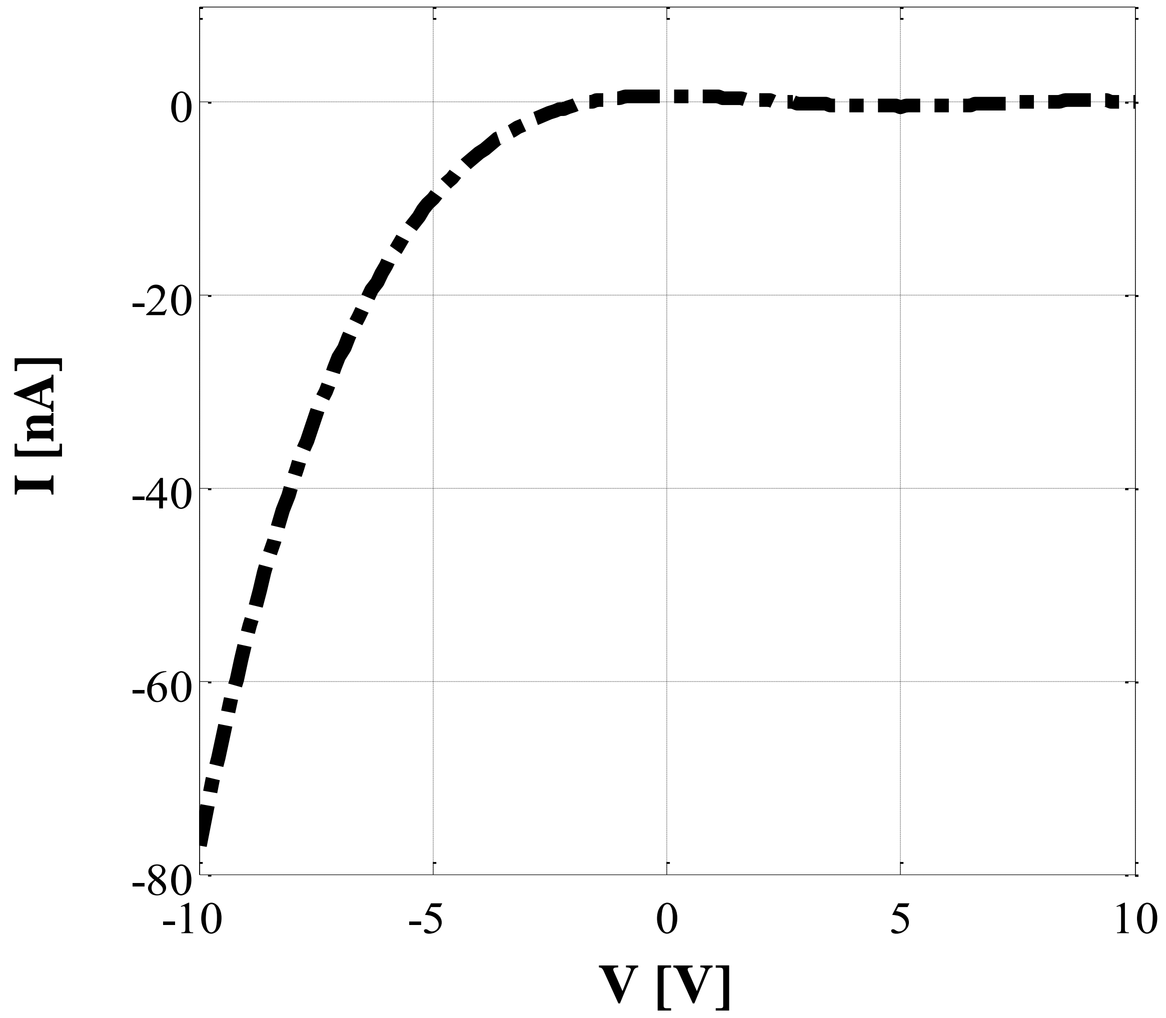

Figure 5.9: Measured DC IV characteristics of Pt-Al_2O_3-HfO_2-TiO_2-Ti MIM diodes with 1.5nm-thick constituent tunnel layers for junction sizes of 200nm×200nm.

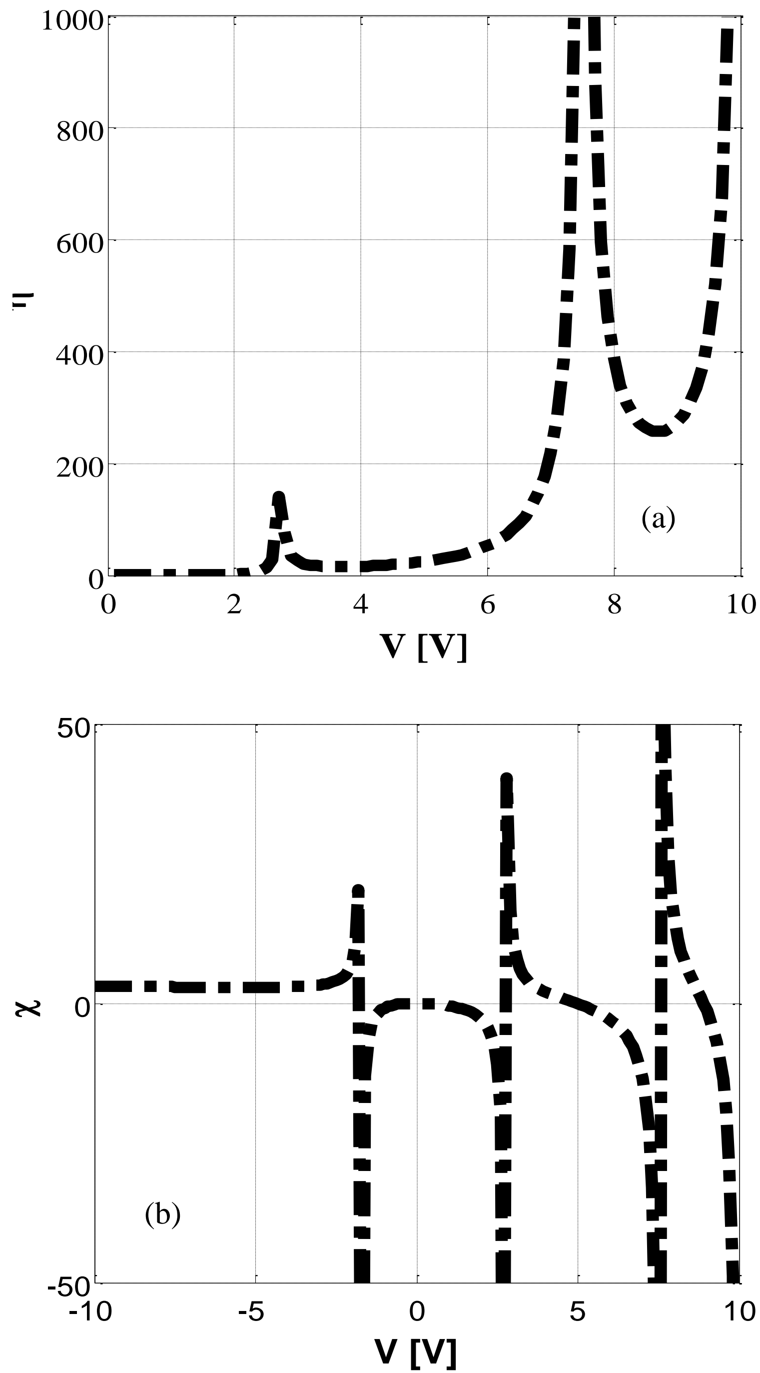

Figure 5.10: Measured DC characteristics of Pt-Al_2O_3-HfO_2-TiO_2-Ti MIM diodes with 1.5nm-thick constituent the tunnels layers and junction sizes of 200nm×200nm. (a) asymmetry; and (b) nonlinearity versus bias voltage.

DC characteristics of these single layer devices are fairly similar. Both types of devices have exhibited limited nonlinearity and the asymmetry around one. However, there is disparity in the range of operational current; thus leading to difference in the junction differential resistance.

The DC behavior of the MIM devices with multiple insulator tunnel layers was measured and the results are shown in Fig. 5.7 to Fig. 5.10. Fig. 5.7 and Fig. 5.8 show the DC characteristics of a MIIM diode, while Fig.5.9 and Fig. 5.10 present the DC characteristics of a MIIIM diode. The current was measured by biasing the diode from -10V to +10V. As shown in Fig. 5.7, for the MIIM diode under -10V of the bias voltage, the current reaches -4nA whereas the current is approximately 0.5nA under +10V by bias voltage. The same pattern was observed for MIIIM diode; -70nA was measured when the device is under reverse bias voltage of -10V, whereas almost no current was measured at +10V. All the measurements were done at room temperature.

5.2 Engineering Effective Barrier Height of Multi-Tunnel-Layer MIM Diodes

Fig. 5.5 and Fig. 5.6 show the responses that include (a) current versus voltage; (b) differential resistance versus voltage; (c) nonlinearity;(χ) versus voltage; (d) asymmetry (η) versus voltage; and (e) responsivity versus voltage for Pt-oxide-Ti MIM diodes with 3nm-thick Al_2O_3 and HfO_2 tunnel layers, respectively. Fig. 5.7 and Fig. 5.9 present the current versus voltage relationship for a Pt-Al_2O_3-TiO_2-Ti MIIM diode and a Pt-Al_2O_3-HfO_2-TiO_2-Ti MIIIM diode, respectively. The asymmetry and nonlinearity of the multi-tunnel-layer devices were shown in Fig. 5.8 and Fig. 5.10 for MIIM and MIIIM diodes correspondingly. The plot shown is for diode design structured of 200nm×200nm junction size.

It was observed that despite the usage of metal electrodes with different work functions, the devices with a single tunnel layer have exhibited limited asymmetry and nonlinearity,

compared to the devices with multiple tunnel layers. It was reported recently that great asymmetry performance of MIM diodes is not primarily limited by the difference in work function of the different metal electrodes [93, 157]. Implementation of the device with multiple tunnel layers improves the asymmetry as well as the nonlinearity. It is evident in the results presented in this work that the asymmetry was high for the Pt-Al_2O_3-TiO_2-Ti MIM diode. This was a consequence of the employment of a stacked dual layer of oxides as the tunnel layer. From the *I-V* plot, it was observed that the MIIM/MIIIM devices are turned on under reverse bias. Also, the analysis of Pt-Al_2O_3-HfO_2-TiO_2-Ti MIIIM diode showed a similar response as that of the MIIM. However, the MIIIM device exhibited superior asymmetry and nonlinearity compared to a dual tunnel layer MIIM diode. This was a result of the thickness of the tunnel junction as well as the use of an extra tunnel layer with asymmetrical barrier height.

5.2.1 Pt-Al_2O_3-Ti and Pt-HfO_2-Ti MIM Diode

The purpose of this study was to design and fabricate a nano-scale "zero bias" MIM tunneling diode for mixing and rectifying high frequency signals. As discussed in Chapter 4, junction size, material composition and thickness of the tunnel layer are the primary factors that determine the diode performance. In addition, the electronics structure of the junction materials plays a crucial role in determining the tunneling characteristics of the devices. Specifically, the electron tunneling probability through a tunnel barrier is determined by the barrier height. The barrier height is affected by the tunnel layer's electron affinity that is determined by the oxide thickness.

The rectifying performance of a MIM diode can mathematically predicted by its barrier height as shown by this research. That is the reason why greater effort has been devoted to engineering the barrier height of the device. The asymmetry and the nonlinearity of the MIM

diode is the consequence of the Schottky barrier height formed at the interface of metal/insulator. For example, to determine the turn-on voltage of the MIM diode, Periasamy et al. [160] proposed that "to minimize the turn-on voltage and maximized asymmetry and nonlinearity, the electron affinity of the insulator should be close to one of the metal work function values so as produce low barrier height." The DC rectifying characteristics of a single layer nano-junction MIM diode were shown in Fig. 5.5 and Fig. 5.6. The analysis presented evaluates the DC characteristics of Al_2O_3 and HfO_2, respectively.

The work functions of Pt and Ti were assumed to be 5.3eV and 4.1eV, respectively. Likewise, the electron affinity of Al_2O_3 and HfO_2 was assumed to be 1.3eV and 2.5eV, respectively. Hence, the barrier heights of Pt-Al_2O_3, HfO_2-Ti, Pt-HfO_2, and HfO_2-Ti interfaces were 4eV, 2.8eV, 2.8eV, and 1.6eV, respectively. This implies that the Pt-HfO_2-Ti MIM diode should exhibit better asymmetry and nonlinearity compared as to the Pt-HfO_2-Ti MIM diode. This was evident in the analysis observed in Fig. 5.5) and Fig. 5.6, while devices with HfO_2 tunnel layer have exhibited limited asymmetry and nonlinearity, HfO_2, devices with Al_2O_3 exhibited no asymmetry and nonlinearity.

5.2.2 Pt-Al_2O_3-TiO_2-Ti MIIM Diode

Considering the electronic structure of the Pt-Al_2O_3-TiO_2-Ti MIIM diode, the material interfaces were cascaded to affect the formation of effective barrier height that allowed an easy forward electron tunneling. Three barrier heights were formed with the MIIM diode, one between Pt-Al_2O_3 (ϕ_1), another between Al_2O_3-TiO_2 (ϕ_2), and the third between TiO_2-Ti (ϕ_3). The barrier height between adjacent materials was expressed as the difference between the metal work-function (Φ) and the electron affinity (χ) of the oxide for the metal/oxide barrier [140], or the difference between electron affinities (χ) of two adjacent oxides, for oxide/oxide interface.

Tunnel current through the MIM diode is exponentially dependent on the mean barrier height [76, 88, 94]. The interfaces were engineered so that the barrier height value at one end (representing the valence band) was drastically higher than the other end (corresponding to the conduction band). For a Pt-Al_2O_3-TiO_2-Ti device, the barrier height between Pt-Al_2O_3 interface was approximately 4eV, while the barrier height of the Al_2O_3-TiO_2 and TiO_2-Ti interfaces were 1.3eV and0.3eV respectively. This means that approximately 4eV was needed to bring the Fermi level of the Pt to the conduction level of TiO_2 to allow direct tunneling through the 1.5nm-thick Al_2O_3 tunnel layer. In summary, the effective barrier was formed with cascaded interfaces in a way that $\phi_1 > \phi_2 > \phi_3$, thus the electron was propelled from the valence band of the bottom electrode to the top electrode, which represents the conduction band of the device. With this configuration, as the device was biased by a sweeping voltage the magnitude of the negative current increases more rapidly than that of the positive current. As expected, this caused a negative slope in the nonlinearity versus voltage plot. This was evident in the *I-V* characteristics shown in Fig. 5.7 and nonlinearity seen in Fig. 5.8.

5.2.3 Pt-Al_2O_3-HfO_2-TiO_2-Ti MIIIM Diode

To further the improvement of the performance of MIM diode devices, another Schottky barrier was introduced by adding an extra metallic oxide to the MIIM tunneling diode. An MIIIM tunneling diode was fabricated with a stacked Al_2O_3, HfO_2, and TiO_2 tunnel layers. In the same manner as the MIIM, the oxides were cascaded to form an effective barrier height with $\phi_1 > \phi_2 > \phi_3 > \phi_4$. The Pt-$Al_2O_3$-$HfO_2$-$TiO_2$-Ti MIIIM diode DC rectifying performance was presented in Fig.5.9 and Fig. 5.10. Each of the oxide tunnel layers was 1.5nm-thick, thus leading to a total thickness of 4.5nm. The electron affinities assumed for the oxides were 1.35eV, 2.5eV, and 2.95eV for Al_2O_3, HfO_2, and TiO_2, respectively. In this case, ϕ_1 = 4eV, ϕ_2 = 1.15eV, ϕ_3 = 0.45eV,

and ϕ_4 = 2.05eV. When a negative (forward) bias voltage is applied to the Ti electrode, a higher measured current compared to the reverse voltage is presented in Fig. 5.9. Also, the asymmetry and nonlinearity responses were higher in the MIIIM diode, compared to the MIM and MIIM diodes.

5.3 Summary

Based on the model prediction discussed in chapter 2, electron tunneling in either MIM, MIIM or MIIIM diode is anticipated to demonstrate high level of nonlinearity and asymmetry. Examining the DC characteristics for these four sets of devices, it's observed that the tunneling characteristics of the stacked multiple thin film tunnel layers result in superior performance compared to the devices with single tunnel layer. Fig. 5.5 (a), Fig. 5.6 (a), Fig. 5.7 and Fig. 5.9 displays *I-V* characteristics of the MIM diodes with a single HfO_2, or Al_2O_3, double tunnel layer of Al_2O_3/TiO_2 and triple tunnel layer stack of $Al_2O_3/HfO_2/TiO_2$, respectively. As shown by the measured DC characteristics in Fig. 8 and Fig. 10 due to tailored potential barrier of the stacked layers, there is considerably greater degree of asymmetry (greater than 10^3) and nonlinearity (greater than 20). The asymmetric characteristics of the nano-scale devices with multiple tunnel layers in this work make such a class of MIM diodes excellent choice for mixing high high-frequency signal up to THz.

Fig. 5.7 and Fig. 5.9 show the diodes behaviors under the forward and reverse bias voltages. It seems the forward current is negligibly small and rise monotonically as the voltage increases. At specific voltages (I=-2.2V, II=3.9V, and III=8.9V) in Fig. 5.11, there exists a hallmark for engineering band structure base on the tunneling current, as a result of cascaded potential in the tunneling layers. At the voltage "I", there is enough energy from the bottom electrode (Pt) to surpass that tilted potential barrier of first tunnel layer barrier and matching the

edge of the potential barrier of the second tunnel layer. As the bias voltage increase, the potential barrier height formed by the second tunnel layer decreases. The transportation of electron from one electrode to another through a designed multiple interfaces of potential barrier height has been implemented. As a result, it has been observed oxides layer engineering could be only significant means by which high degree of *I-V* asymmetry and nonlinearity have been achieved.

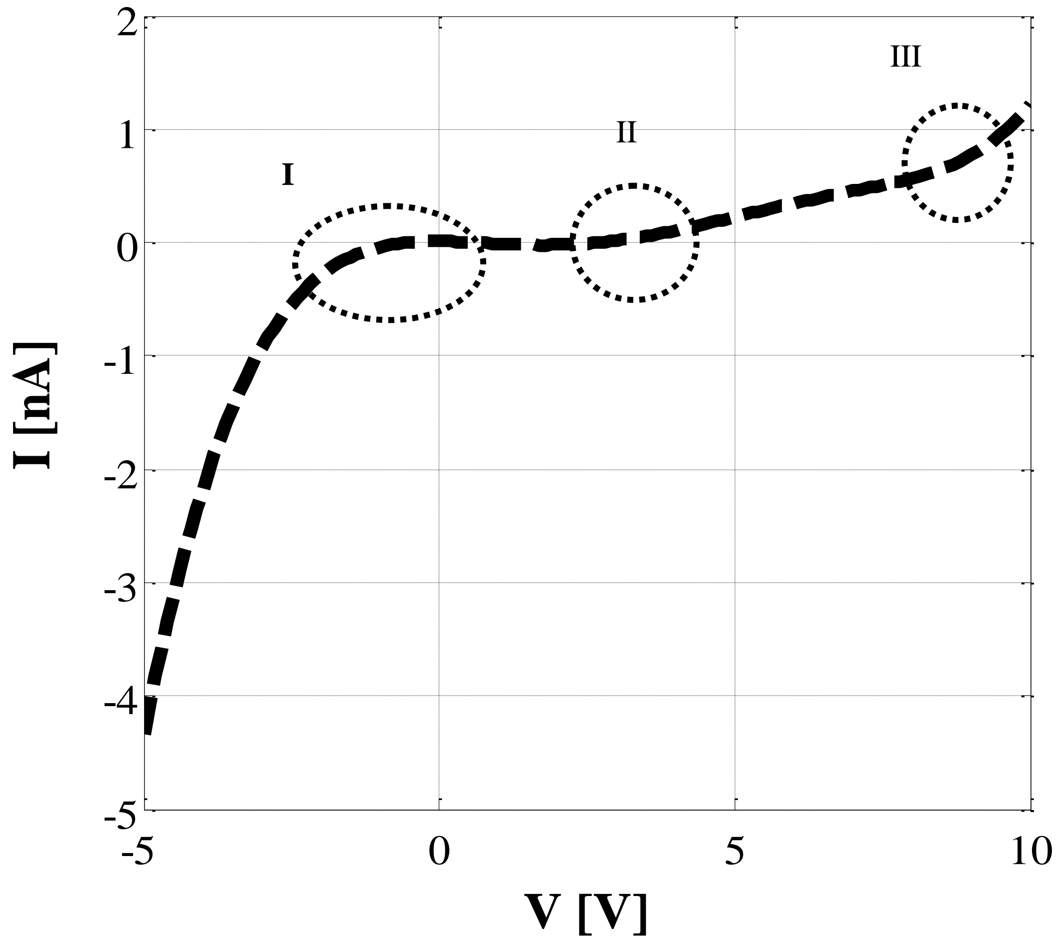

Figure 5.11: DC *I-V* characteristics of a Pt-Al_2O_3-TiO_2-Ti MIIM diode. Showing the forward current behavior with three specific region of formation of potential well between interface.

CHAPTER 6: MIM DIODE RF CHARCTERIZATION

This study develops the equivalent circuit model of the MIM/MIIM diodes based on measured RF performance within 0.01 – 65 GHz. Subsequently, the circuit model is used to study the expected responsivity performance of the diodes.

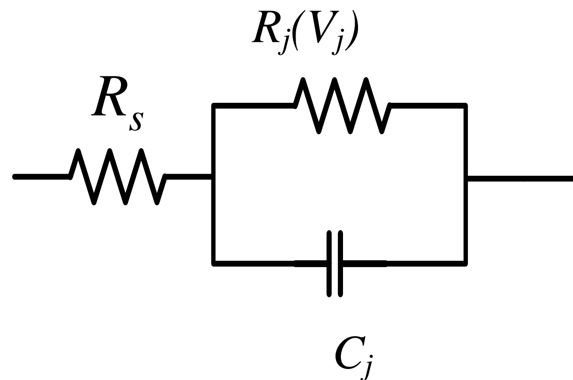

Figure 6.1: The lumped-elements equivalent circuit model for a MIM tunneling diode.

MIM/MIIM diode's equivalent circuit consists of voltage dependent and independent components. As already discussed in Chapters 2 and Chapter 4, the band diagram and associated *I-V* responses can be affected by the bias voltage. This means that the junction resistance of the diode depends on the voltage. On the other hand, capacitance of the diode is directly related to the thickness of the insulator between the metal electrodes. Hence, junction capacitance is fixed and independent of bias voltage. The equivalent circuit of the diode junction has been already

established, and its replica is shown in Fig. 6.1, where $R_j(V_j)$ represent voltage dependent nonlinear junction resistance of the diode, the R_s represents the series resistance and the C_j represents the diode shunt junction capacitance.

6.1 Device Characterization

6.1.1 Schottky Diode Characterization

For a preliminary study, the DC and RF characterizations of off-the-shelf Schottky diodes were carried out to provide a complete understanding of their complex impedance behavior. A surface mounted Schottky diode SKD_INF_ST23 was used to investigate and develop a generic procedure for the parameter extraction. The scattering parameters (S-parameter) of the diode were obtained using the vector network analyzer (VNA) connected to the device via bias Tees (the measurement setup will be discussed later in this chapter). The VNA was calibrated using a customized Thru-Reflect-Line (TRL) calibration (shown in Fig. 6.2). The 50Ω microstrip lines were designed using ADS LineCalc.

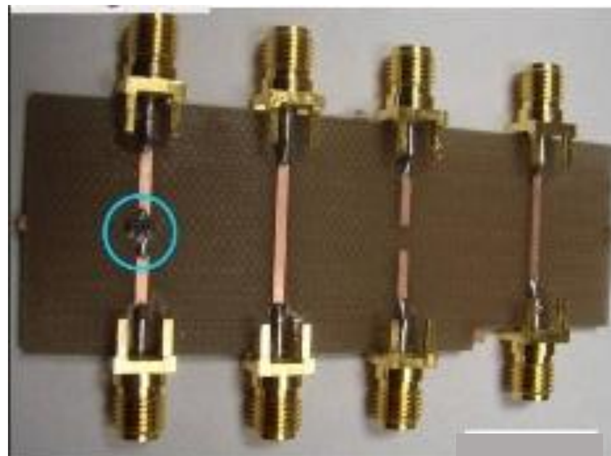

Figure 6.2: A measurement substrate showing device under test (DUT) with custom designed calibration microstrip lines.

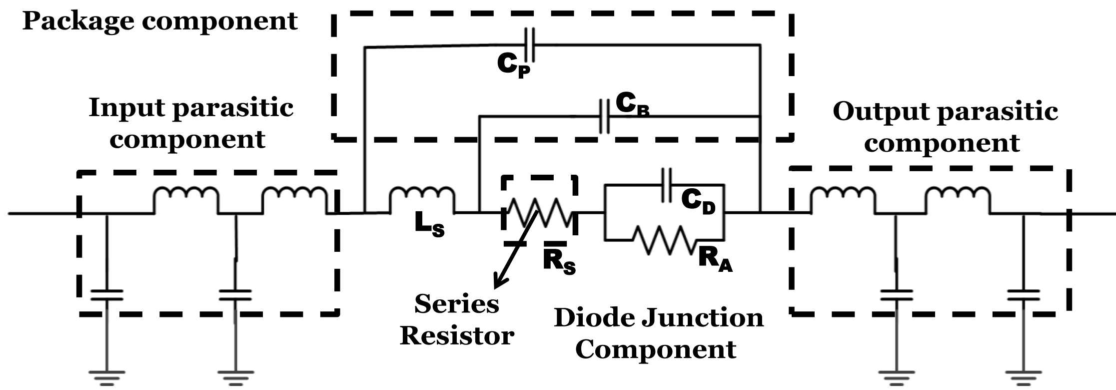

Figure 6.3: Equivalent circuit model used to represent RF behavior of Schottky diodes

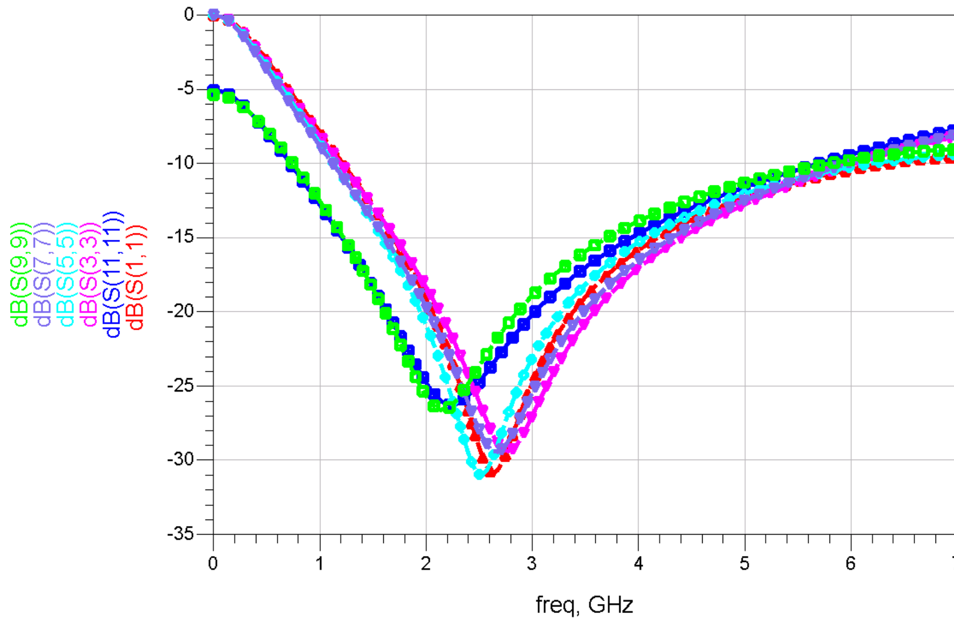

Figure 6.4: S-parameter plots at different bias voltages for 0V, 0.1V and 0.3V. $S_{1,1}$ and $S_{3,3}$ represent measured and equivalent circuit predicted parameters at 0V bias condition, respectively; $S_{5,5}$ and $S_{7,7}$ represent measured and equivalent circuit predicted parameters at 0.1V bias condition, respectively; and $S_{9,9}$ and $S_{11,11}$ represent measured and equivalent circuit predicted parameters at 0.3V bias condition, respectively.

An optimization procedure was carried out to fit the measured scattering parameter values to the model predicted scattering parameters based on the equivalent circuit. This

procedure was implemented in Advanced Design System (ADS) software to extract the package, parasitic, and junction parameters of the diode (see Fig. 6.3) at different bias voltages. As shown in Fig. 6.4 and Fig 6.5, the parameter extraction approach has been successfully developed and validated. A similar approach will be applied to study the nanofabricated MIM/MIIM diodes to extract equivalent circuit models from their measured scattering parameters.

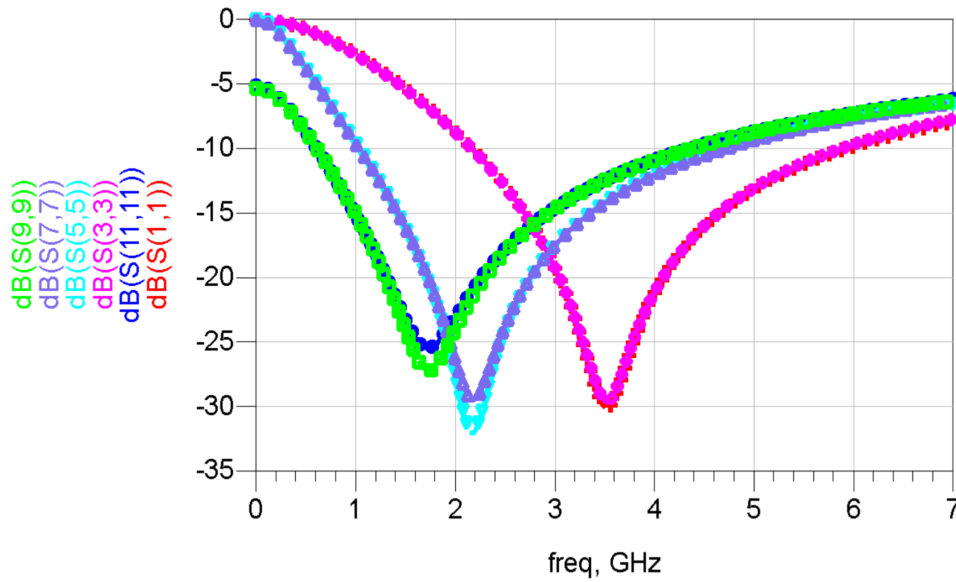

Figure 6.5: S-parameter plots at different bias voltages for -3V, 0.1V and 0.3V. $S_{1,1}$ and $S_{3,3}$ represent measured and equivalent circuit predicted parameters at -3V bias condition, respectively, $S_{5,5}$ and $S_{7,7}$ represent measured and equivalent circuit predicted parameters at 0.1V bias condition, respectively, and $S_{9,9}$ and $S_{11,11}$ represent measured and equivalent circuit predicted parameters at 0.3V bias

6.1.2 MIM Tunneling Diode Characterization

The RF characterization was performed using the *I-V* and two port scattering parameter measurements. The process included:

- Current (I) vs. voltage (V) measurement – Here the preliminary performance of the diode was observed. In addition, the differential resistance ($R_j= dV/dI$) of the diode was calculated from the *I-V* data.
- Device cutoff frequency – The cutoff frequency of the diode was determined from its RC time constant, defined as: $f_c = 1/2\pi R_j C_j$, with $C_j = \varepsilon A/d$, where A is the junction area, d is the junction tunnel layer thickness and ε is the junction tunnel material's dielectric constant.
- S-parameter measurement - A two port frequency dependent S-parameter measurement was carried out at different bias voltages. The data obtained from the vector network analyzer is in Touchtone file format with s2p file extension.
- The measured data and circuit optimization – The proposed circuit voltage dependent junction resistance and other voltage independent components were optimized to be fitted against the response with the measured S-parameters.

The MIM, MIIM and MIIIM diodes used for the modeling process were Pt-Al_2O_3-Ti (with 3nm-thick Al_2O_3), Pt-HfO_2-Ti (with 3nm-thick of HfO_2), Pt-Al_2O_3-TiO_2-Ti (with 1.5nm-thick Al_2O_3 and 1.5nm-thick of TiO_2), and Pt-Al_2O_3- HfO_2-TiO_2-Ti (1.5nm-thick Al_2O_3, 1.5nm-thick of HfO_2, and 1.5nm-thick of TiO_2). The junction areas of all the devices were 200nm×200nm. The fabrication process of these devices was discussed in Chapter 5.

6.1.3 MIM Diode Equivalent Circuit Model

The cross-sectional view of a high frequency planar MIM diode with a single tunnel layer is shown in Fig. 6.6. The MIM junction diode is indicated with the diode symbol. The intrinsic parasitic voltage dependent spreading resistance is depicted showing its connection to the diode.

The parasitic extrinsic lumped elements are from the coplanar waveguide (CPW) feed lines connected to the device. Fig. 6.7 presents the SEM top-view of the device.

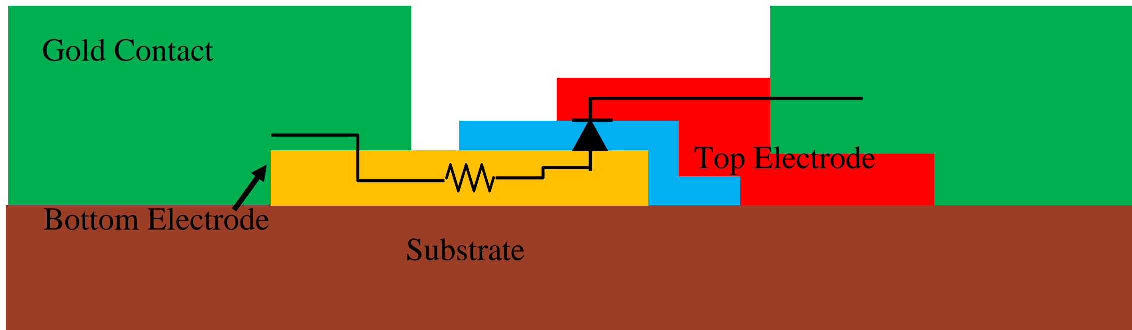

Figure 6.6: Cross-sectional view schematic of a typical MIM diode structure.

6.1.4 Measurement Setup

Figure 6.8 presents the corresponding RF measurement setup used in this work. The E8361A PNA network analyzer (10 MHz to 67 GHz) by Agilent was used for the S-parameter measurement. The PNA was connected to the GGB ground-signal-ground (GSG) probes which have 150µm pitch size. The PNA was connected to the probe through Picosecond Pulse Lab bias Tees; which was used to apply a DC voltage across the device under test (i.e., MIM diode). The Agilent E3631A DC output DC power supply was used as the voltage source.

The S-parameter measurement was performed using a two-port measurement setup. Although the diodes were designed for frequencies well above 100GHz, their RF characteristics were measured from 1GHz to 65GHz due to the available capability. The E8361A PNA network analyzer port attenuation was set to -30dB at port one and port two of the network analyzer to ensure small signal conditions. The PNA was calibrated using the Short-Open-Load-Thru (SOLT) calibration standard on CS5 calibration substrate. The S-parameter of the devices were

measured under different voltages. For the on-wafer measurement, 1μm-thick gold cpw probe pads without backside metallization were employed as shown in Fig. 6.7. Gold was used as the contact pad, with a thickness of 1.0μm.

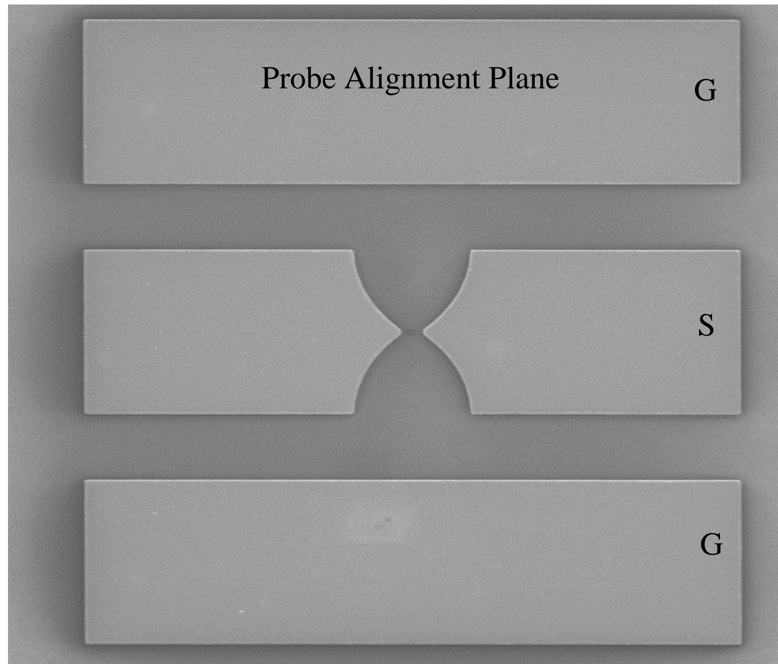

Figure 6.7: SEM image showing the structure of a nano-junction sized MIM diode in the CPW configuration for on wafer measurement.

The parameter extraction using the outlined optimization approach is shown in Fig. 6.8. An ADS gradient based optimization technique was used. The simulation was carried out simultaneously for fitting the equivalent model to the measured responses under 3 different bias conditions. The voltage independent components of all the circuits were kept same under all the bias condition. The results shown in Fig. 6.10 to Fig. 6.13 represent the reflection and transmission responses for the Pt-Al_2O_3-HfO_2-TiO_2-Ti MIIIM diode, Pt-Al_2O_3-TiO_2-Ti MIIM

diode, Pt-HfO_2-Ti MIM diode, and Pt-Al_2O_3-Ti MIM diode, respectively. The MIIIM and MIIM diodes were measured under a bias voltage ranging from -10V to +10V, while the MIM diode was biased between -2V and +2V. The bias voltage was limited by the DC operational voltage of the devices as discussed in Chapter 5. Table 6.1 to Table 6.4 summarizes the intrinsic and extrinsic lumped element optimization values for all the cases. Consistent with the DC analysis presented in Chapter 5, the extracted parameters for junction resistance and capacitance are on par with the calculated values from DC analysis.

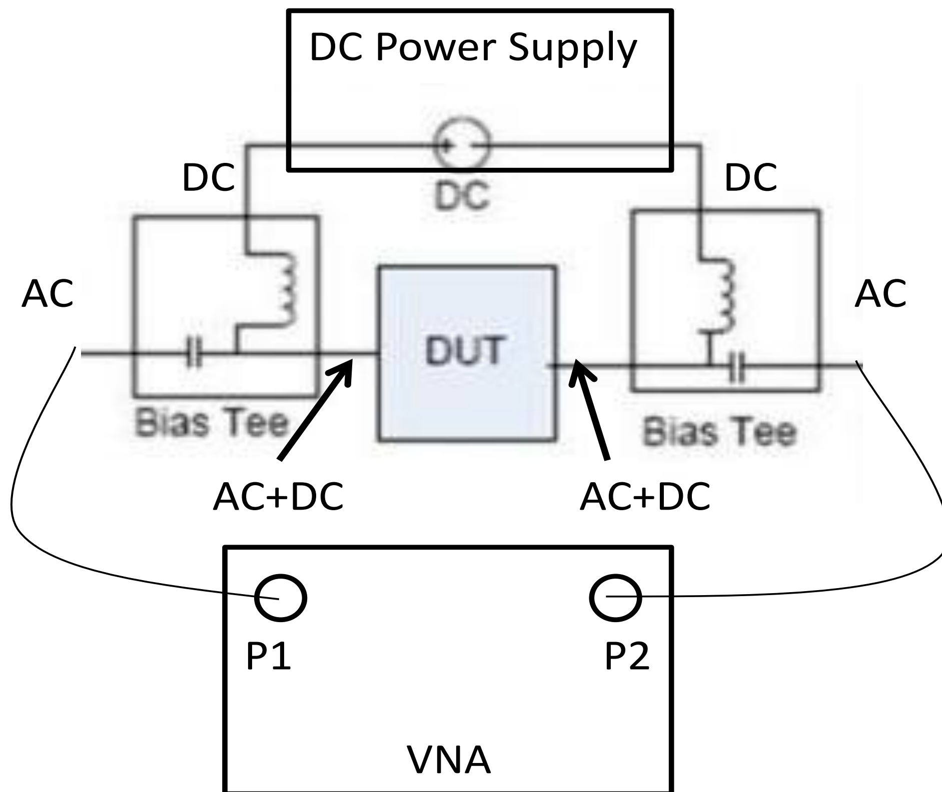

Figure 6.8: RF measurement setup with the device under test (DUT) connected to the VNA and the voltage source via a pair of bias Tees.

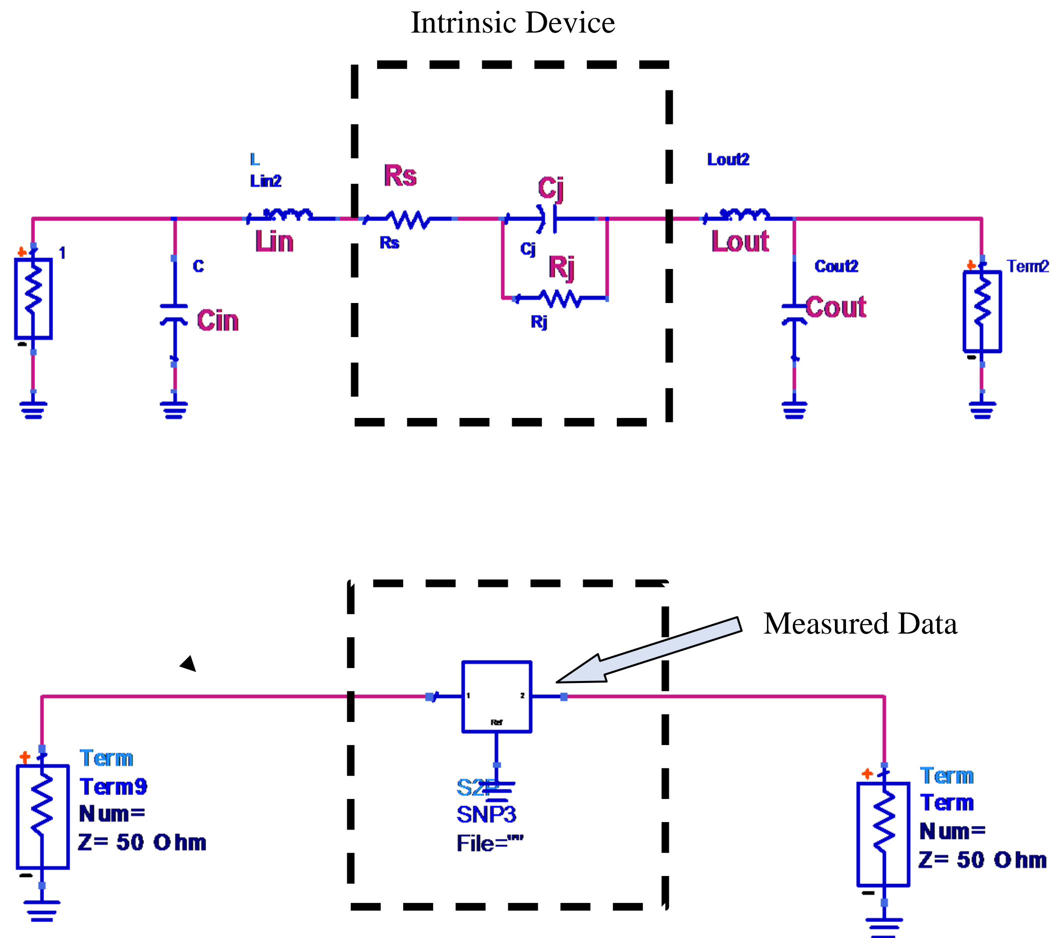

Figure 6.9: For direct comparison between measured responses and the model predicted behavior, both the small-signal equivalent circuit model and the measured s2p data were jointly studied by ADS simulation. Through a model optimization procedure, the fitted model parameters were extracted through comparison.

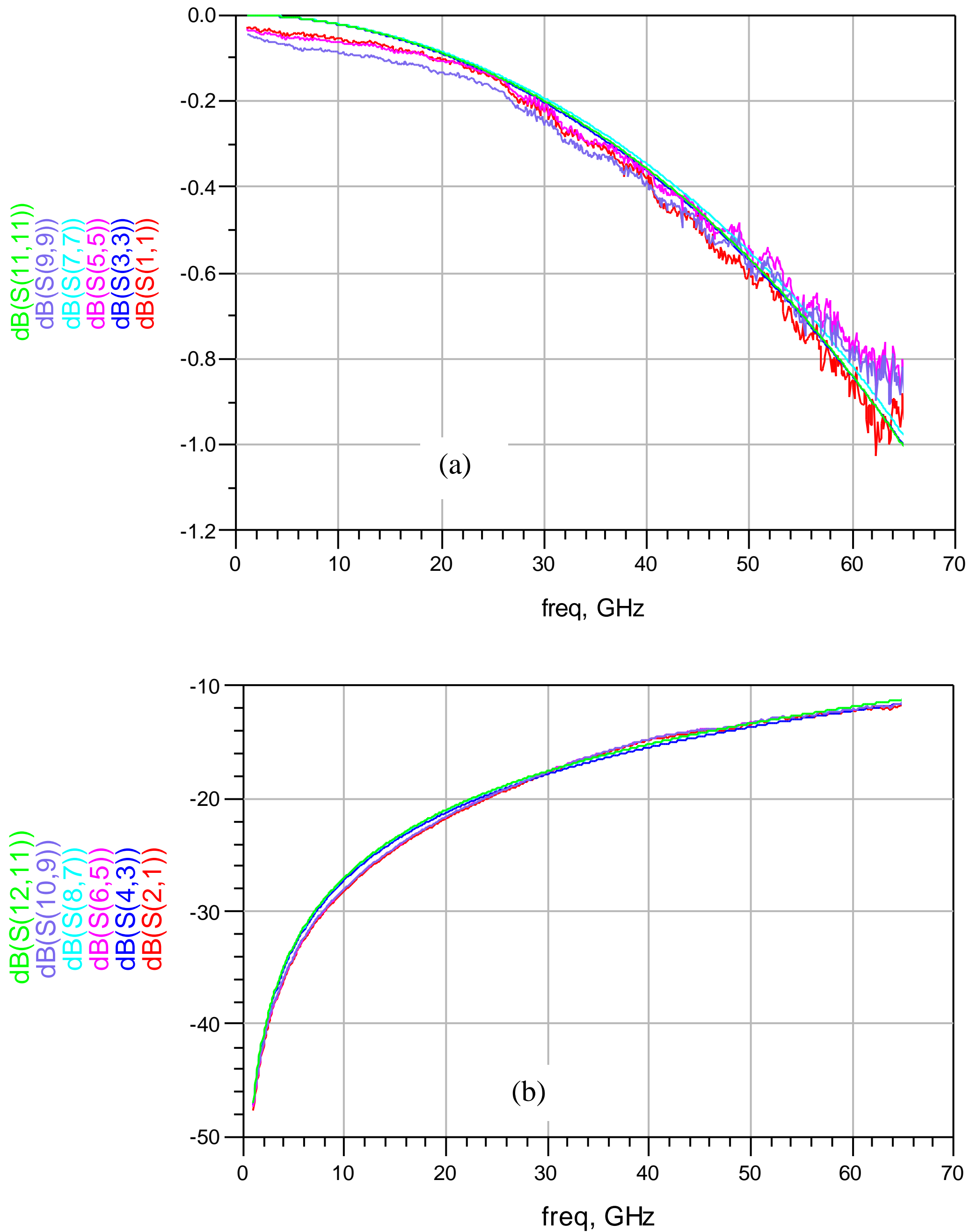

Figure 6.10: The optimization result for the Pt-Al_2O_3-HfO_2-TiO_2-Ti MIIIM diode showing the plots for the measured and modeled S-parameter responses at different bias voltages. $S_{1,1}$, $S_{3,3}$, $S_{2,1}$, and $S_{4,3}$ modeled reflection and transmission characteristics at -10V, $S_{5,5}$, $S_{7,7}$, $S_{6,5}$, and $S_{8,7}$ represent measured and modeled reflection and transmission characteristics at 0V, and $S_{9,9}$, $S_{11,11}$, $S_{10,9}$, and $S_{12,11}$ represent measured and modeled reflection and transmission characteristics at +10V, respectively

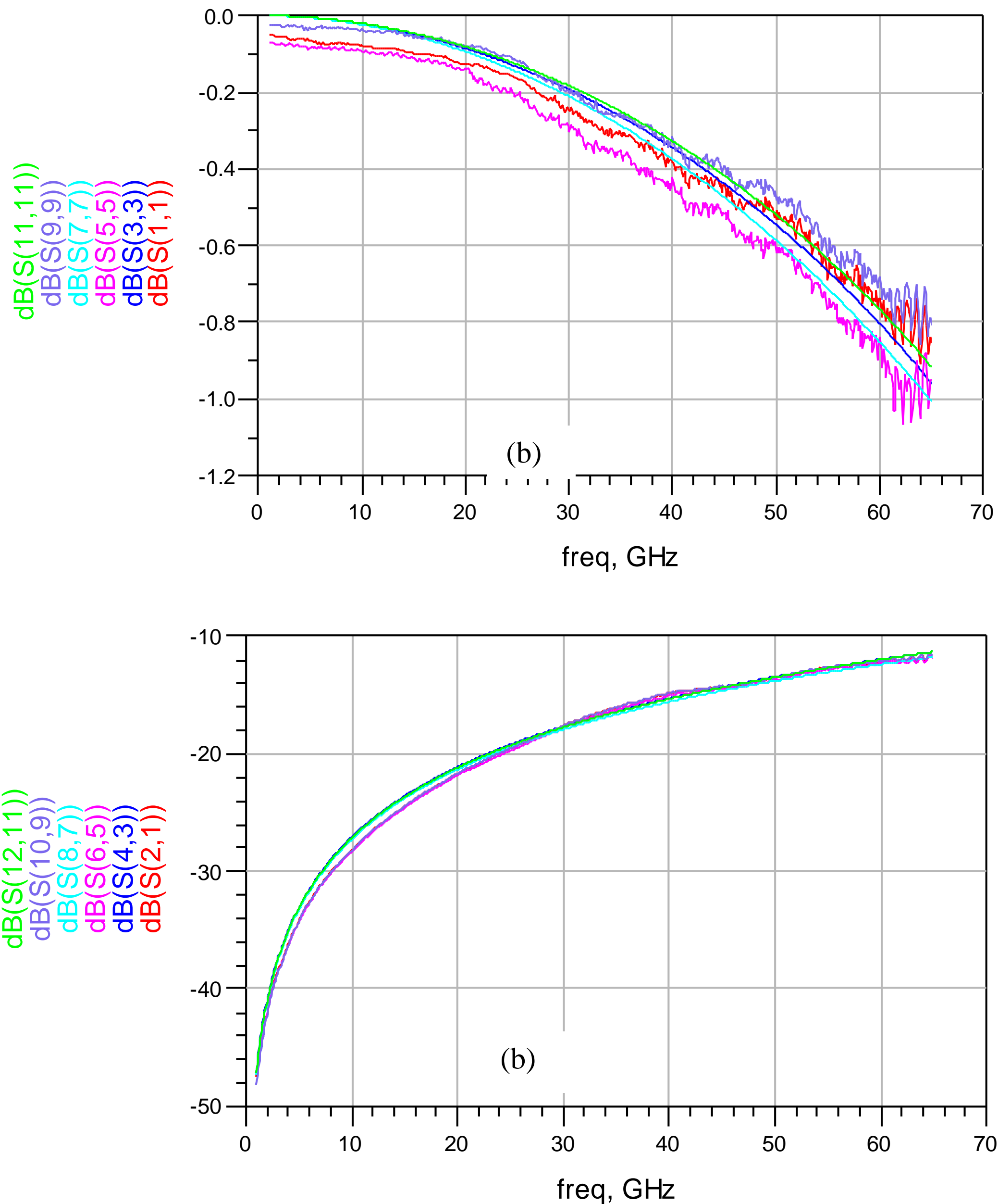

Figure 6.11: The optimization result for the Pt-Al_2O_3-TiO_2-Ti MIIM diode showing the plots of the measured and modeled S-parameter response at different bias voltages. $S_{1,1}$, $S_{3,3}$, $S_{2,1}$, and $S_{4,3}$ represent measured and modeled reflection and transmission characteristics at -10V, $S_{5,5}$, $S_{7,7}$, $S_{6,5}$, and $S_{8,7}$ represents measured and modeled reflection and transmission characteristics at 0V, and $S_{9,9}$ $S_{11,11}$, $S_{10,9}$, and $S_{12,11}$ represents measured and modeled reflection and transmission characteristics at +10V, respectively

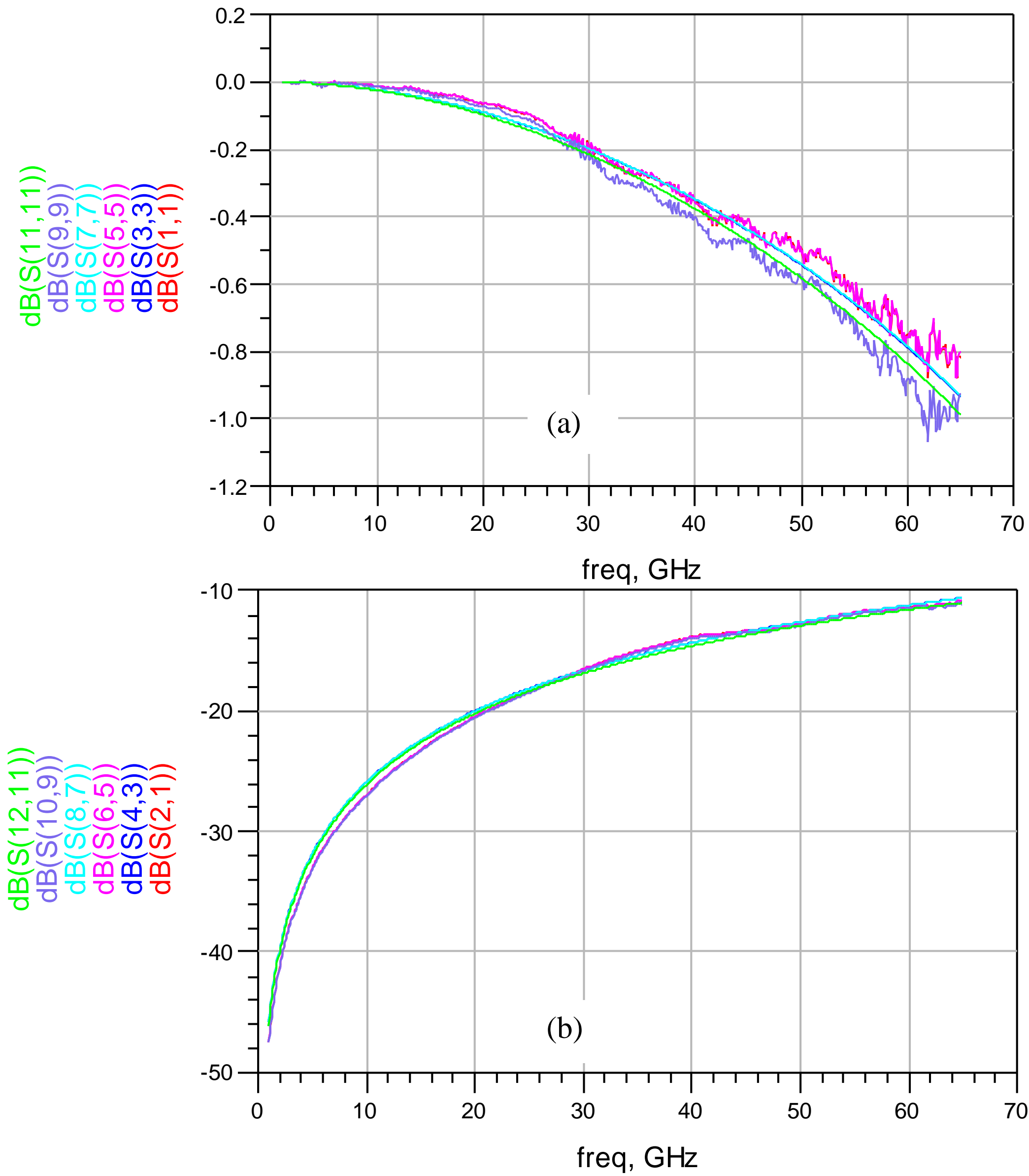

Figure 6.12: The optimization result for the Pt-HfO_2-Ti MIM diode showing the plots of the measured and modeled S-parameter response at different bias voltages. $S_{1,1}$, $S_{3,3}$, $S_{2,1}$, and $S_{4,3}$ represent measured and modeled reflection and transmission characteristics at -2V, $S_{5,5}$, $S_{7,7}$, $S_{6,5}$, and $S_{8,7}$ represents measured and modeled reflection and transmission characteristics at 0V, and $S_{9,9}$ $S_{11,11}$, $S_{10,9}$, and $S_{12,11}$ represents measured and modeled reflection and transmission characteristics at +2V, respectively.

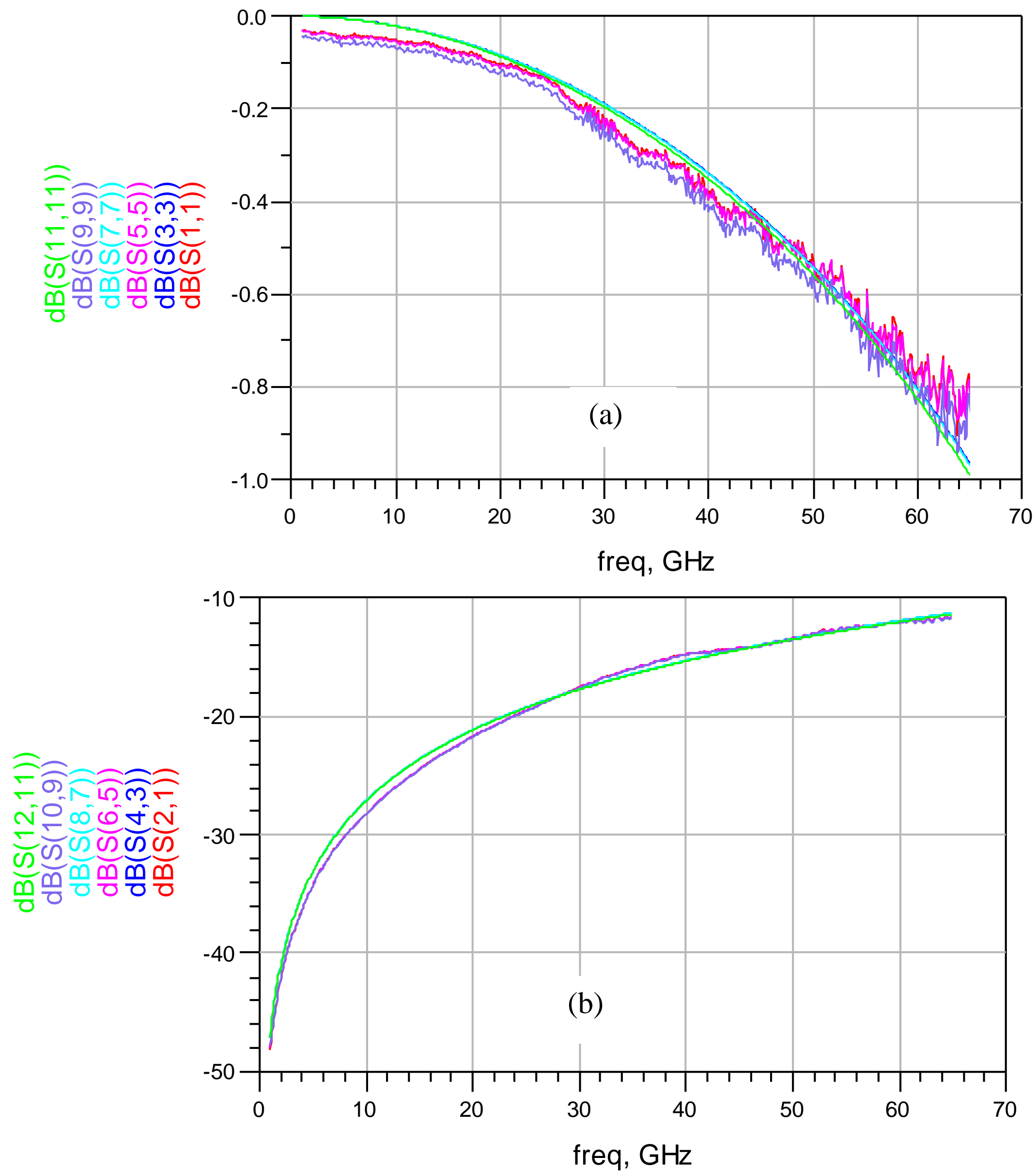

Figure 6.13: The optimization result for the Pt-Al_2O_3-Ti MIM diode showing the plots of the measured and modeled S-parameter response at different bias voltages. $S_{1,1}$, $S_{3,3}$, $S_{2,1}$, and $S_{4,3}$ represents measured and modeled reflection and transmission characteristics at -2V, $S_{5,5}$, $S_{7,7}$, $S_{6,5}$, and $S_{8,7}$ represents measured and modeled reflection and transmission characteristics at 0V, and $S_{9,9}$ $S_{11,11}$, $S_{10,9}$, and $S_{12,11}$ represents measured and modeled reflection and transmission characteristics at +2V, respectively.

Table 6.1: Extracted lumped element values for the equivalent circuit for a Pt-Al_2O_3-HfO_2-TiO_2-Ti diode.

	-10V	**0V**	**10V**
Extracted R_j (GΩ)	6.67	50.5	1.35
Extracted C_j (fF)	7	7	7
L_{in} (pH)	291	291	291
L_{out} (pH)	2.8	2.8	2.8
C_{in} (fF)	23	23	23
C_{out} (fF)	17	17	17
R_s (Ω)	75	84	77

Table 6.2: Extracted lumped element values for the equivalent circuit for Pt-Al_2O_3-TiO_2-Ti diode.

	-10V	**0V**	**10V**
Extracted R_j (GΩ)	1	80.2	8.2
Extracted C_j (fF)	6	6	6
L_{in} (pH)	263	263	263
L_{out} (pH)	3	3	3
C_{in} (fF)	22	22	22
C_{out} (fF)	16	16	16
R_s (Ω)	71	95	76

Table 6.3: Extracted lumped element values for the equivalent circuit for a Pt-HfO_2-Ti diode.

	-2V	**0V**	**2V**
Extracted R_j (GΩ)	6.2	1.15	3.1
Extracted C_j (fF)	7	7	7
L_{in} (pH)	282	282	282
L_{out} (pH)	3.2	3.2	3.2
C_{in} (fF)	23	23	23
C_{out} (fF)	17.87	17.87	17.87
R_s (Ω)	73	73	73

Table 6.4: Extracted lumped element values for the equivalent circuit for Pt- Al_2O_3-Ti diode.

	-2V	**0V**	**2V**
Extracted R_j (GΩ)	9.9	1.9	4.9
Extracted C_j (fF)	8.1	8	7.9
L_{in} (pH)	242.1	242.1	242.1
L_{out} (pH)	3.1	3.1	3.1
C_{in} (fF)	25.1	25.1	25.1
C_{out} (fF)	22.1	22.1	22.1
R_s (Ω)	51.12	50.96	65.40

The intrinsic model parameters extracted from the above optimization procedure are similar to the calculated values obtained from the DC measurements. For example, from the *I-V*

data, the MIIIM junction resistance can be calculated as 6GΩ, 50GΩ, and 1GΩ at -10V, 0V, and +10V biases, respectively. As shown in Table. 6.1, the extracted junction resistance values are fairly consistent.

6.2 Rectification Performance of the Diodes

To determine the rectification efficiency of the MIM/MIIM/MIIIM diodes, a detector circuit simulation was performed. In practice, the major application of the MIM tunneling diode described in the work is mainly for rectifying signal to generate DC output. As discussed earlier, the key applications of the devices are non-linear signal processing in term of rectification, detection and mixing. For the case of a rectifier, a fraction of RF input power is converted into DC output. To test the devices as a detector, the extracted circuit model is incorporated in a RF detection scheme within ADS. The nonlinear junction resistance of the diode is modeled with the Agilent Symbolically-Defined Device (SDD) tool. SDD is an equation based component, which captures the non-linear behavior in a single or multiple port device arrangement.

The MIM diode is modeled as a nonlinear resistor based on the measured *I-V* response. The MIM diode junction equivalent circuit consists of a resistor and a capacitor (see Fig. 6.1). The diode is biased with a DC voltage and excited with an incident RF signal. From the equivalent circuit model of the diode, the series resistor R_s is the total resistance created by the contact and lead metals, R_j is voltage dependent junction resistance (modeled with SDD) and C_j is the junction capacitance. L_{in}, C_{in}, L_{out}, and C_{out} are parasitic components that model the presence of the pad. Consequently, the circuit is used to simulate the detection capability of the diode. R_j was extracted from the *I-V* measurement. From the DC measurement, the relationship between measured voltage (V_m) and the measured current (I_m) is $V_m = I_m*(R_s + R_j)$. R_s has been extracted in Table 6.1 to 6.4 based on measured S-parameters and data fitting procedures. Hence,

R_s is known and R_j can be written as $R_j = (V_m - I_mR_s)/I_m$. This can be written as $I_m*R_j = (V_m - I_m*R_s)$ => $I*R_j = V$. Since R_j is voltage dependent, a polynomial fit between I and V can be established to model its efficiency in the SDD. Fig. 6.14 present the *I-V* curve represented with a 5th order polynomial equation $I= (3.7e\text{-}5V^5\text{-}1.5e\text{-}3V^4\text{+}1.7e\text{-}2V^3\text{-}5.3e\text{-}2V^2\text{-}3.6e\text{-}3V\text{+}0.11)*1e\text{-}9$ for the MIIM diode. As seen, the 5th order polynomial provides a good fit to the measured data.

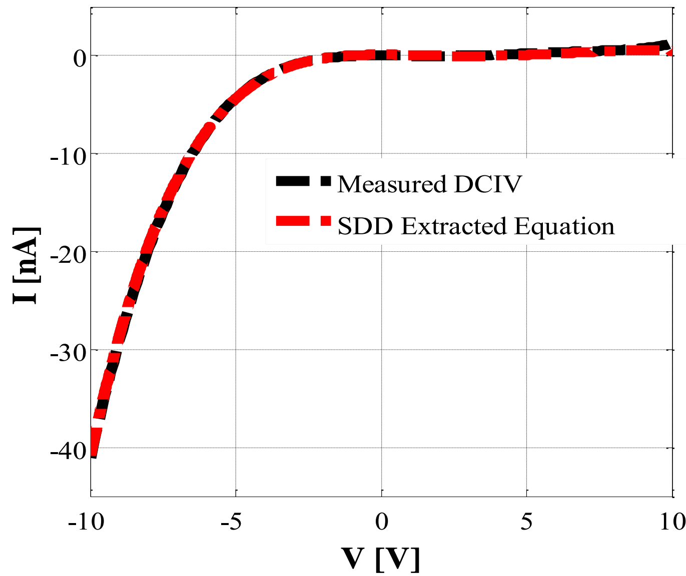

Figure 6.14: Measured I-V response vs. the 5th order polynomial fit used in SDD tool for a Pt-Al_2O_3-TiO_2-Ti MIIM diode.

MIM/MIIM/MIIIM diodes have been evaluated with ADS simulation in a typical detector configuration with parallel RC termination as shown in Fig. 6.15. An harmonic balance simulation in ADS were employed to study the nonlinear behavior at different power levelsl of the RF generator. The source provides the single frequency alternating signal at a specified available power. It also provides a DC bias voltage. The results of the simulation are presented in Fig. 6.16 and Fig. 6.17. The devices were excited with 65GHz RF signal at the power level from +5dBm to +30dBm. The video resistance and capacitor at detector output terminal were set to be

10kΩ and 100pF, respectively. The values of the video elements were chosen to implement DC filtering.

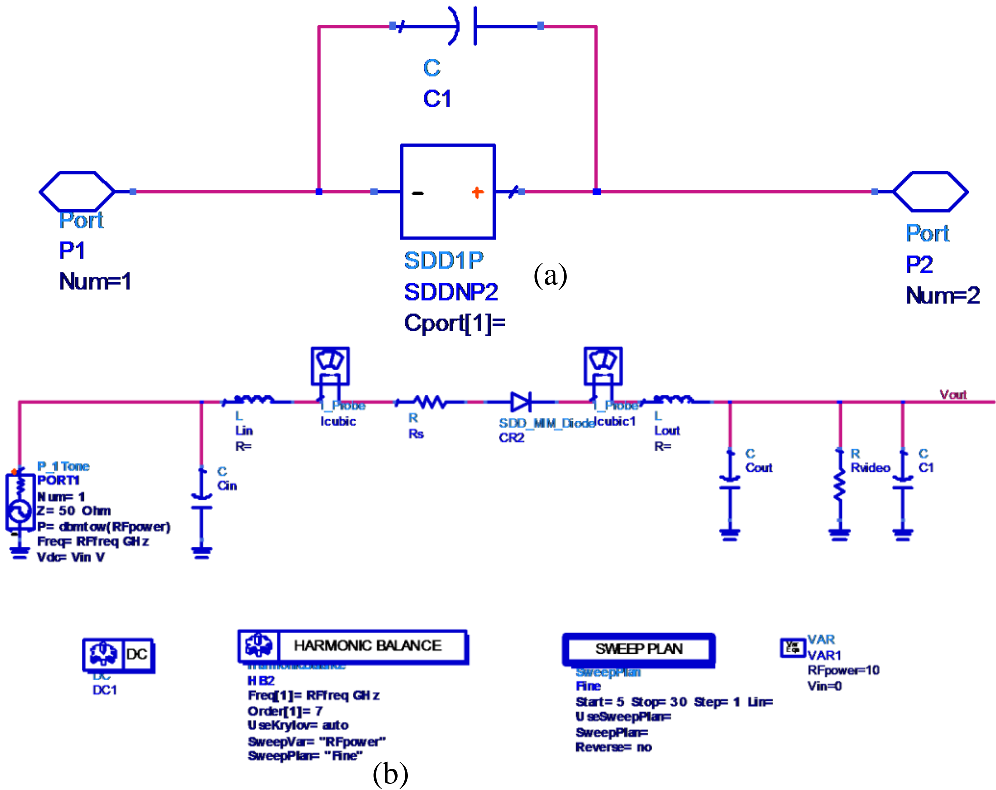

Figure 6.15: Schematic of the MIM diode detection implementation in ADS (Advanced Design System) software.

Fig. 6.16 and Fig. 6.17 show the detected voltage (V_{out}) versus input power from the presented results, (although no attempt was made to match the input impedance to the diode impedance), it is seen that 1.5mV to 6.3mV is detected from MIIIM diode at different bias voltages (see Fig.6.16 (a)), MIIM diode rectifier generates 1mV to 10mV (see Fig. 6.16(b)), whereas a MIM diode with HfO_2 5mV to 800mV rectified output and MIM diode with a Al_2O_3 tunnel junction generates 0.1mV to 70mV of output signal.

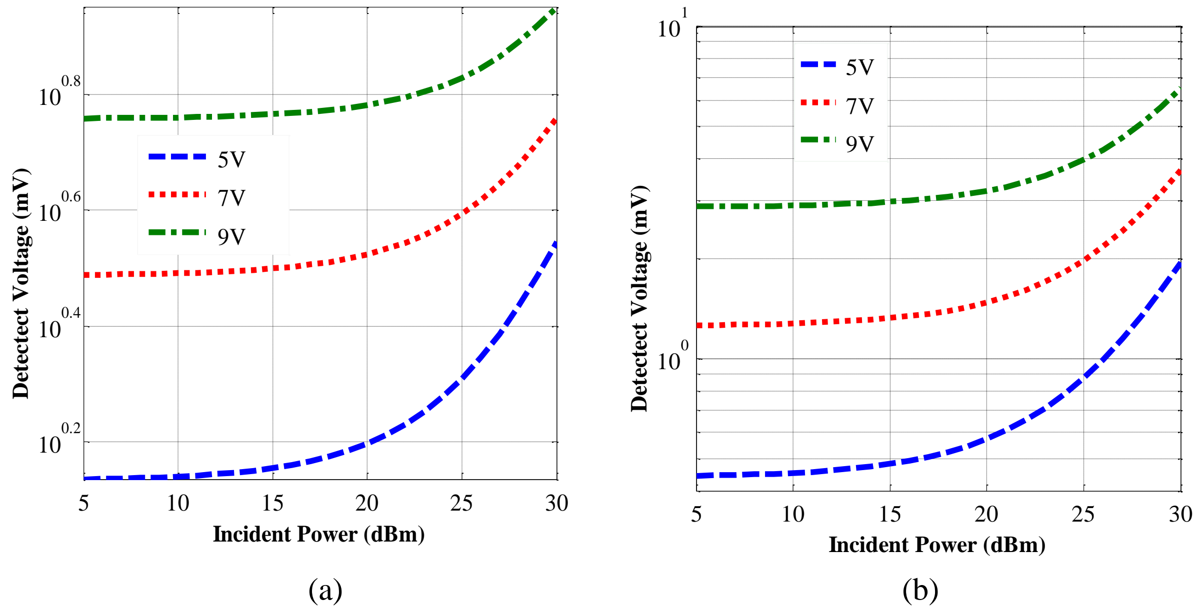

Figure 6.16: The simulated characteristics of nano-scale MIIIM and MIIM diodes showing detected the output voltage versus the input power. (a) Pt-Al_2O_3-HfO_2-TiO_2-Ti MIIIM diode detection plot; and (b) Pt-Al_2O_3-TiO_2-Ti MIIM diode detector

From the above result, Pt-HfO_2-Ti MIM diode's rectification efficiency was found to be the best among all diode. In Chapter 5, the Pt-HfO_2-Ti diode's responsivity (see Section 5.1.3) was found to be the , which is around $\pm 10^7$V/W at -0.28V bias voltage. However, although responsivity is lower at 1V bias voltage, the diode has also a lower differential resistance as seen from Fig. 5.6. Due to the lower differential resistance, the RF power coupled into the diode more efficiently and therefore a better rectification is achieved at 1V bias voltage despite its lower responsivity. As a result, the bias voltage is predominant in determining rectification performance of the diodes.

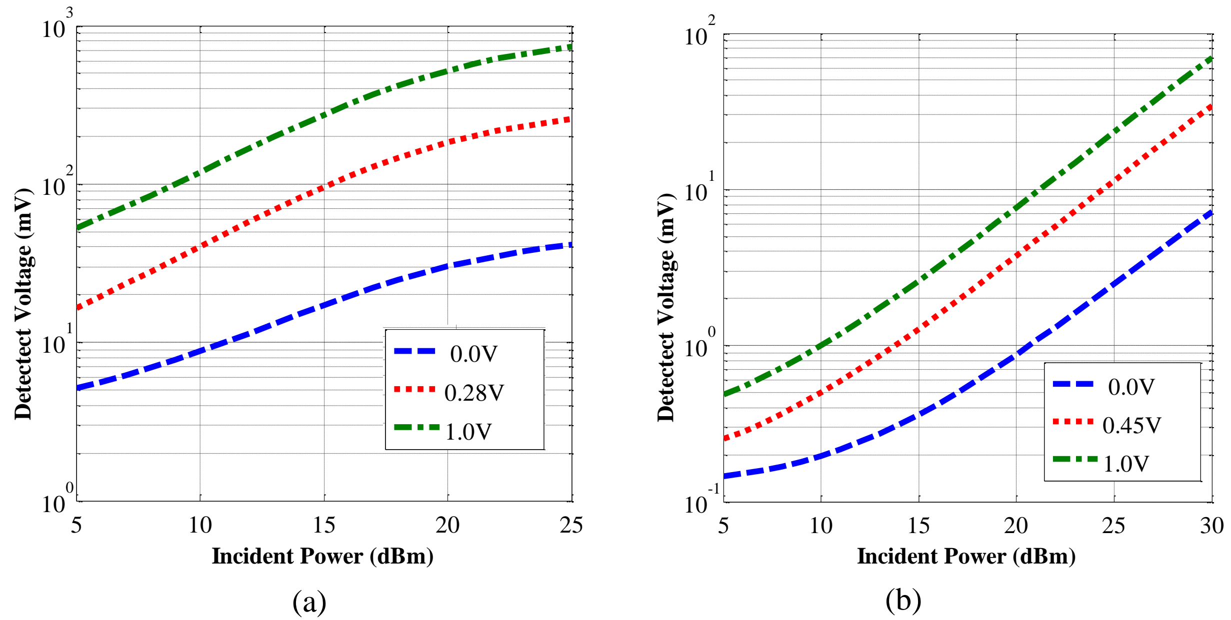

Figure 6.17: The detected voltage characteristics of nano junction MIM diodes showing the output voltage versus source input power. (a) Pt-HfO_2-Ti MIM diode; and (b) Pt-Al_2O_3-Ti MIM detection plot

Another condition is investigated to improve the performance of the diode. Fig. 6.18 presents the V_{out} versus incident RF power for Pt-HfO_2-Ti MIM diode and Pt- Al_2O_3-HfO_2-TiO_2-Ti MIIIM diode with A, B, and C plots. Plots A and C have 1MΩ video resistance connected in series with the diode but different source input impedance (while A has 50Ω, C has 200Ω). Plot B has 50Ω impedance at the source and 10kΩ video impedance. In both cases, the diode was biased at 1V. The results show that the value of the video resistance and different source impedance contributes to the magnitude of the detected voltage. The detector responsivity can be improved by maximizing the RF power delivered to the diode.

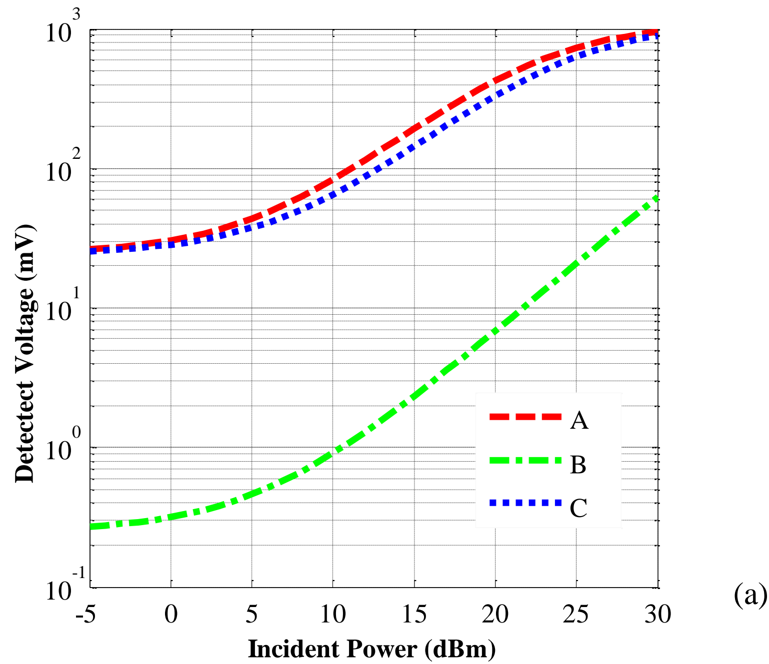

A- Input impedance of 50Ω, video resistance of 1M Ω, simulated at 1V
B - Input impedance of 50Ω, video resistance of 10k Ω, simulated at 1V
C - Input impedance of 200Ω, video resistance of 1M Ω, simulated at 1V

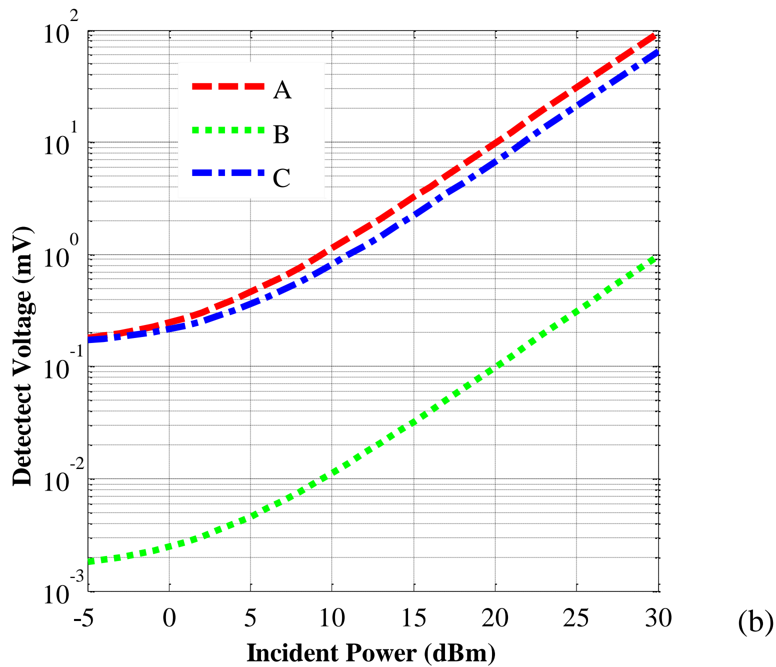

Figure 6.18: Detector output voltage versus input power simulated with different video resistance and input resistance. (a) a Pt-HfO_2-Ti MIM diode; and (b) a Pt- Al_2O_3-HfO_2-TiO_2-Ti MIIIM diode based detector.

6.3 Summary

RF characterizations of MIM/MIIM/MIIIM diodes were performed. The characterization method compares the measured data with equivalent circuit model to extract the equivalent circuit model parameters. First, the scattering parameters of the MIM diodes were measured using the VNA, with the setup described in Fig. 6.8 and Fig. 6.9. Subsequently a, RF circuit simulators (i.e., Advanced Design Systems (ADS)) were employed to improve the fitting between the measured results and response of the circuit model. By employing this methodology, the circuit model shown in Fig. 6.10 was used to extract lumped element model parameter. The summary of the extracted lumped element parameter for each device was presented in Table 6.1 – Table 6.4. The MIM diode parasitic element consisted of C_{in}, L_{in}, C_{out}, and L_{out}, and the voltage dependent lumped element parameters are of R_s, R_j and C_j.

From the rectification efficiency studies, it's observed that;

- The incident RF power level at which detection response transitions into the linear range is higher in devices with stacked junctions as compared to the MIM diodes with single tunnel layer diodes. Specifically, the transition occurs approximately at -50dBm for MIM diode, whereas MIIM/MIIIM diodes go through transition at -25dBm of power (see Fig. 6.19). This is because the barrier height in the stacked layers is higher than single layer, which result in higher impedance and RF mismatch.
- The level of detected output voltage varies when the device is biased under different voltages.
- The diode's rectification efficiency depends strongly on junction resistance. High junction resistance diodes require more voltage and high RF power for rectification.

- All nanofabricated MIM/MIIM/MIIIM diodes exhibited nonlinear response that provides RF rectification. Dual and triple layer junction provides lower rectification efficiency. However, there are uncertainties in their junction thickness that may significantly affect their *I-V* responses. In our future works, the effects of multiple tunnel junction on the rectification efficiency is going to be further explored, by comparing the strength of the rectified signals generated by MIM, MIIM, and MIIIM diodes..

CHAPTER 7: CONCLUDING REMARK AND FUTURE WORK

7.1 Conclusion

In this dissertation, we have described the procedures for carrying out high yield batch fabrication of MIM diodes. In addition, a procedure for characterizing planar MIM/MIIM/MIIIM tunneling diodes is presented, based on direct current (DC) measurements, scattering parameter measurements and directivity simulations. In designing and fabricating these diodes, the thickness of the thin-film tunnel material, sandwiched between two metal electrodes to create a barrier, has been associated to the linearity and junction differential resistance of the diode extracted from DC *I-V* characterization. This directly determines the responsivity of the diode. A stacked ultra-thin tunnel layers was also implemented to improve the asymmetry and the nonlinearity of the MIM diode. It was found that when a number of the stacked tunnel layers with different electron affinities are used, the performance (i.e asymmetry and nonlinearity) of the diode improves.

As a design strategy, a numerical analysis was developed to examine the behavior of the electron transport from one metal electrode to another metal electrode through the barrier. This was done for single and multiple barrier layers. In this effort, the tunneling theory base on quantum mechanical (QM) modeling of the current through MIM with a single and multiple tunnel layer(s) is presented. First, an airy function based on the transfer matrix method was employed to analyze expression for deriving electron tunneling probability. Secondly, to conduct the investigation of electron tunneling through the barrier, a well-known Wentzel-Kramers-

Brillouin (WKB) approximation method was also employed to calculate the tunneling probability of electron transporting through a thin film.

In Chapters 4 and Chapter 5, an investigation was conducted on MIM diodes having different tunnel materials, which were fabricated with a range of junction areas and junction thicknesses prepared by atomic layer deposition. The employment of the ALD process allows formation of pin-hole free tunneling layers with precisely controlled thickness in the sub-5nm range. The effect of the physical properties of the constituent tunneling layer, such as its composition and thickness, often result in a pronounced change in the *I-V* characteristics and the barrier height. MIIM and MIIIM diodes with stacked multiple tunneling layers were also investigated, which have exhibited superior responsivity as compared to that of MIM counterparts with a single tunnel layer. It is evident that the asymmetry of devices with multiple stacked tunnel layers is much more pronounced than that of the typical MIM diode. The nonlinearity is also significant improved in MIIM/MIIIM diodes, which suggests that MIIM/MIIIM diodes are superior in term of their rectification efficiencies when compared with that of the best MIM diode. With a generalized model for an MIM diode junction, the average barrier heights of the several devices were determined and extracted by fitting the model against measured *I-V* responses. Moreover, the results in this dissertation have verified the importance of the strategic choice of tunneling material and its impact on key diode performance parameters. With the procedure, the barrier height was deduced. Consequently, the exact value for electron affinity of the tunnel oxide was determined. The results were compared to the previously published studies on materials' electron affinities.

In addition, with the RF characterization and modeling approach, a procedure was developed to extract the characteristic impedance of the MIM tunneling diode. The

characterization and the modeling procedure developed in this dissertation to extract the MIM diode equivalent circuit model has led to an equivalent circuit model that is verified by RF testing at high frequencies. This was demonstrated with RF measurement up to 65GHz. Impedance mismatch between the diode and the antenna has been a challenge against efficient coupling between antenna and the diode. The novel procedure documented in this dissertation will assist the designers to accommodate the complex nature of diode impedance. The lumped element equivalent circuit of the diode is extracted from its measured S-parameter up to millimeter frequencies.

7.2 Contributions

- A thorough study was conducted to evaluate the impact of the material properties on the overall diode performance by strategically adjusting the device tunneling properties. For this purpose, numerous MIM diodes with different ALD metal oxides with varied thickness have been explored. Even though some of the materials in this experiment have been exployed by others individually, the extended work with in terms of micro/nano-fabrication and the approach we taken in this dissertation has not been reported previously.
- Direct study was conducted by performance comparison between devices with a single and multiple tunnel layer tunneling diodes. The DC and RF characterization of the stacked tunnel layer was investigated to demonstrate its performance benefits as compare to that of the single layer tunnel diode. This was done with different junction area ranging from nanoscale to microscale.
- A mathematical modeling and optimization procedure was developed to extract the mean barrier height of an MIM diode from its *I-V* response. As opposed to the prior efforts that

utilize the bulk properties of materials to determine the barrier height of an MIM diode, the approach presented in this dissertation derives an accurate empirical value based on the actual measurement of the device.

- There is presentation of additional process to improve on the repeatability of the fabrication process of MIM diode. This involves cleaning every layer of the lithography with piranha etching. It aids in reducing every residual resist that can create extra charge or hole within layers interfaces.
- A novel MIM diode equivalent model parameter extraction approach was developed. With this procedure, the actual values of the voltage dependent junction lumped element model parameters are ascertained, which reveals the characteristics impedance of the diode. One promising application of MIM diodes demands integration with antennas. However, the problem of impedance mismatch between antenna and coupled MIM diode could be addressed with this procedure.

7.3 Future Work

- The application of the MIM diode parameter extraction techniques of this work to design and characterize a rectifying antenna (i.e., rectenna) for the purpose of efficiently scavenging energy from EM radiation at quasi-optical frequencies (i.e. 100GHz to 1THz) would be one major future research area. Various antenna configurations could be employed for integration with these diodes for spectral image acquisition.
- Study could be conducted to explore MIM diode with organic monolayer individually or a stack of organic/inorganic tunnel layers.

REFERENCES

[1] L. Yujiri, M. Shoucri, and P. Moffa, "Passive millimeter wave imaging," *Microwave Magazine, IEEE,* vol. 4, pp. 39-50, 2003.

[2] K. S. Yngvesson, T. Korzeniowski, Y.-S. Kim, E. L. Kollberg, and J. F. Johansson, "The tapered slot antenna-a new integrated element for millimeter-wave applications," *Microwave Theory and Techniques, IEEE Transactions on,* vol. 37, pp. 365-374, 1989.

[3] G. M. Rebeiz, "Millimeter-wave and terahertz integrated circuit antennas," *Proceedings of the IEEE,* vol. 80, pp. 1748-1770, 1992.

[4] A. V. Boriskin, A. I. Nosich, S. V. Boriskina, T. M. Benson, P. Sewell, and A. Altintas, "Lens or resonator? Electromagnetic behavior of an extended hemielliptic lens for a sub-millimeter-wave receiver," *Microwave and optical technology letters,* vol. 43, pp. 515-518, 2004.

[5] C. Walczyk, C. Wenger, R. Sohal, M. Lukosius, A. Fox, J. Dabrowski*, et al.*, "Pulse-induced low-power resistive switching in HfO[sub 2] metal-insulator-metal diodes for nonvolatile memory applications," *Journal of Applied Physics,* vol. 105, pp. 114103-6, 2009.[6] p. 443, 2013.

[7] L. O. Hocker, D. R. Sokoloff, V. Daneu, A. Szoke, and A. Javan, "FREQUENCY MIXING IN THE INFRARED AND FAR-INFRARED USING A METAL-TO-METAL POINT CONTACT DIODE," *Applied Physics Letters,* vol. 12, pp. 401-402, 1968.

[8] B.-l. Twu and S. E. Schwarz, "Mechanism and properties of point-contact metal-insulator-metal diode detectors at 10.6 mu," *Applied Physics Letters,* vol. 25, pp. 595-598, 1974.

[9] C. Bradley and G. Edwards, "Characteristics of metal-insulator-metal point-contact diodes used for two-laser mixing and direct frequency measurements," *Quantum Electronics, IEEE Journal of,* vol. 9, pp. 548-549, 1973.

[10] H. W. Hubers, G. W. Schwaab, and H. P. Roser, "Video detection and mixing performance of GaAs Schottky-barrier diodes at 30 THz and comparison with metal-insulator-metal diodes," *Journal of Applied Physics,* vol. 75, pp. 4243-4248, 1994.

[11] S. W. M. Heiblum, J. Whinnery, T. Gustafson., "Characteristics of intergrated MOM junction at DC and at optical frequencies," *Quantum Electronics, IEEE Journal of,* vol. 14, pp. 159-169, 1978.

[12] R. Meservey, P. M. Tedrow, and J. S. Brooks, "Tunneling characteristics of amorphous Si barriers," *Journal of Applied Physics,* vol. 53, pp. 1563-1570, 1982.

[13] B. M. Kale, "Electron Tunneling Devices In Optics," *Optical Engineering,* vol. 24, pp. 242267-242267, 1985.

[14] J. O. McSpadden, F. Lu, and C. Kai, "Design and experiments of a high-conversion-efficiency 5.8-GHz rectenna," *Microwave Theory and Techniques, IEEE Transactions on,* vol. 46, pp. 2053-2060, 1998.

[15] J. O. McSpadden, T. Yoo, and C. Kai, "Theoretical and experimental investigation of a rectenna element for microwave power transmission," *Microwave Theory and Techniques, IEEE Transactions on,* vol. 40, pp. 2359-2366, 1992.

[16] M. Sarehraz, K. Buckle, T. Weller, E. Stefanakos, S. Bhansali, Y. Goswami*, et al.*, "Rectenna developments for solar energy collection," in *Photovoltaic Specialists Conference, 2005. Conference Record of the Thirty-first IEEE*, 2005, pp. 78-81.

[17] H. Gupta and M. B. Morais, "Theory of electrical characteristics for metal-oxide-insulator Schottky barrier and metal-insulator-metal structures," *Journal of Applied Physics,* vol. 68, pp. 176-182, 1990.

[18] G. Sachit, J. Saumil, and M. Garret, "Quantum theory of operation for rectenna solar cells," *Journal of Physics D: Applied Physics,* vol. 46, p. 135106, 2013.

[19] R. M. Osgood I, B. R. Kimball, and J. Carlson, "Nanoantenna-coupled MIM nanodiodes for efficient vis/nir energy conversion," 2007, pp. 665203-665203-11.

[20] P. C. D. Hobbs, R. B. Laibowitz, and F. R. Libsch, "Ni/NiO/Ni tunnel junctions for terahertz and infrared detection," *Applied Optics,* vol. 44, pp. 6813-6822, 2005/11/10 2005.

[21] F. Hindle, A. Cuisset, R. Bocquet, and G. Mouret, "Continuous-wave terahertz by photomixing: applications to gas phase pollutant detection and quantification," *Comptes Rendus Physique,* vol. 9, pp. 262-275, 2008.

[22] A. G. Davies, A. D. Burnett, W. Fan, E. H. Linfield, and J. E. Cunningham, "Terahertz spectroscopy of explosives and drugs," *Materials Today,* vol. 11, pp. 18-26, 2008.

[23] T. Ouchi, K. Kajiki, T. Koizumi, T. Itsuji, Y. Koyama, R. Sekiguchi*, et al.*, "Terahertz Imaging System for Medical Applications and Related High Efficiency Terahertz Devices," *Journal of Infrared, Millimeter, and Terahertz Waves,* pp. 1-13, 2013.

[24] C. Walczyk, C. Wenger, R. Sohal, M. Lukosius, A. Fox, J. Dąbrowski*, et al.*, "Pulse-induced low-power resistive switching in HfO2 metal-insulator-metal diodes for nonvolatile memory applications," *Journal of Applied Physics,* vol. 105, pp. -, 2009.

[25] S. Krishnan, E. Stefanakos, and S. Bhansali, "Effects of dielectric thickness and contact area on current–voltage characteristics of thin film metal–insulator–metal diodes," *Thin Solid Films,* vol. 516, pp. 2244-2250, 2008.

[26] S. Grover and G. Moddel, "Engineering the current–voltage characteristics of metal–insulator–metal diodes using double-insulator tunnel barriers," *Solid-State Electronics,* vol. 67, pp. 94-99, 2012.

[27] S. A. Mojarad, J. P. Goss, K. S. K. Kwa, Z. Zhou, R. A. S. Al-Hamadany, D. J. R. Appleby*, et al.*, "Leakage current asymmetry and resistive switching behavior of SrTiO[sub 3]," *Applied Physics Letters,* vol. 101, pp. 173507-3, 2012.

[28] N. Shinohara and H. Matsumoto, "Experimental study of large rectenna array for microwave energy transmission," *Microwave Theory and Techniques, IEEE Transactions on,* vol. 46, pp. 261-268, 1998.

[29] C. Fumeaux, W. Herrmann, F. Kneubühl, and H. Rothuizen, "Nanometer thin-film Ni–NiO–Ni diodes for detection and mixing of 30 THz radiation," *Infrared physics & technology,* vol. 39, pp. 123-183, 1998.

[30] J. Zhou, N. Park, J. W. Dawson, K. J. Vahala, M. A. Newkirk, and B. I. Miller, "Terahertz four-wave mixing spectroscopy for study of ultrafast dynamics in a semiconductor optical amplifier," *Applied Physics Letters,* vol. 63, pp. 1179-1181, 1993.

[31] A. Sanchez, J. C. F. Davis, K. C. Liu, and A. Javan, "The MOM tunneling diode: Theoretical estimate of its performance at microwave and infrared frequencies," *Journal of Applied Physics,* vol. 49, pp. 5270-5277, 1978.

[32] R. C. Augeri, "Heterodyne analysis of metal-oxide-metal diodes," *Journal of Applied Physics,* vol. 52, pp. 6395-6400, 1981.

[33] Y. S. Lee and SpringerLink, *Principles of terahertz science and technology*. New York: Springer, 2009.

[34] K. Humphreys, J. P. Loughran, M. Gradziel, W. Lanigan, T. Ward, J. A. Murphy*, et al.*, "Medical applications of terahertz imaging: a review of current technology and potential applications in biomedical engineering," in *Engineering in Medicine and Biology Society, 2004. IEMBS '04. 26th Annual International Conference of the IEEE*, 2004, pp. 1302-1305.

[35] J. A. L'huillier, G. Torosyan, M. Theuer, Y. Avetisyan, and R. Beigang, "Generation of THz radiation using bulk, periodically and aperiodically poled lithium niobate – Part 1: Theory," *Applied Physics B,* vol. 86, pp. 185-196, 2007/01/01 2007.

[36] H. A. G. A. Crocker, M.F. Kimmitt and L.E.S. Mathias, "Stimulated emission in the far infra-red," *Nature,* vol. 201, pp. 250-251, January 1964.

[37] T. Y. Chang, T. J. Bridges, and E. G. Burkhardt, "cw SUBMILLIMETER LASER ACTION IN OPTICALLY PUMPED METHYL FLUORIDE, METHYL ALCOHOL, AND VINYL CHLORIDE GASES," *Applied Physics Letters,* vol. 17, pp. 249-251, 1970.

[38] D. T. Hodges, F. B. Foote, and R. D. Reel, "Efficient high-power operation of the cw far-infrared waveguide laser," *Applied Physics Letters,* vol. 29, pp. 662-664, 1976.

[39] T. Kruczek, R. Leyman, D. Carnegie, N. Bazieva, G. Erbert, S. Schulz*, et al.*, "Continuous wave terahertz radiation from an InAs/GaAs quantum-dot photomixer device," *Applied Physics Letters,* vol. 101, pp. 081114-4, 2012.

[40] N. Sei, H. Ogawa, and K. Yamada, "Multi-range free-electron laser with a pair of dielectric multilayer mirrors," *Applied Physics Letters,* vol. 101, pp. 144101-4, 2012.

[41] P. Thoma, A. Scheuring, M. Hofherr, S. Wunsch, K. Il'in, N. Smale*, et al.*, "Real-time measurement of picosecond THz pulses by an ultra-fast YBa[sub 2]Cu[sub 3]O[sub 7 - d] detection system," *Applied Physics Letters,* vol. 101, pp. 142601-4, 2012.

[42] A. W. M. Lee, Q. Qin, S. Kumar, B. S. Williams, Q. Hu, and J. L. Reno, "Real-time terahertz imaging over a standoff distance (> 25 meters)," *Applied Physics Letters,* vol. 89, pp. 141125-3, 2006.

[43] F. Sizov, V. Petriakov, V. Zabudsky, D. Krasilnikov, M. Smoliy, and S. Dvoretski, "Millimeter-wave hybrid un-cooled narrow-gap hot-carrier and Schottky diodes direct detectors," *Applied Physics Letters,* vol. 101, pp. 082108-5, 2012.

[44] G. A. Blake, K. B. Laughlin, R. C. Cohen, K. L. Busarow, D. H. Gwo, C. A. Schmuttenmaer*, et al.*, "Tunable far infrared laser spectrometers," *Review of Scientific Instruments,* vol. 62, pp. 1693-1700, 1991.

[45] M. Klee, D. Beelen, W. Keur, R. Kiewitt, B. Kumar, R. Mauczok*, et al.*, "Application of Dielectric, Ferroelectric and Piezoelectric Thin Film Devices in Mobile Communication and Medical Systems," in *Applications of ferroelectrics, 2006. isaf '06. 15th ieee international symposium on the*, 2006, pp. 9-16.

[46] B. Berland, "Photovoltaic technologies beyond the horizon: optical rectenna solar cell," *Final Report, NREL/SR-520-33263,* 2003.

[47] D. Kotter, S. Novack, W. Slafer, and P. Pinhero, "Theory and manufacturing processes of solar nanoantenna electromagnetic collectors," *Journal of Solar Energy Engineering,* vol. 132, p. 011014, 2010.
[48] S. Basu and A. Dutta, "Modified heterojunction based on zinc oxide thin film for hydrogen gas-sensor application," *Sensors and Actuators B: Chemical,* vol. 22, pp. 83-87, 1994.
[49] R. H. Reuss, B. R. Chalamala, A. Moussessian, M. G. Kane, A. Kumar, D. C. Zhang*, et al.*, "Macroelectronics: Perspectives on Technology and Applications," *Proceedings of the IEEE,* vol. 93, pp. 1239-1256, 2005.
[50] J.-W. Choi, Y. S. Nam, and M. Fujihira, "Nanoscale fabrication of biomolecular layer and its application to biodevices," *Biotechnology and Bioprocess Engineering,* vol. 9, pp. 76-85, 2004.
[51] F. Sizov, "THz radiation sensors," *Opto-Electronics Review,* vol. 18, pp. 10-36, 2010/03/01 2010.
[52] J. Kiessling, R. Sowade, I. C. Mayorga, K. Buse, and I. Breunig, "Note: Coherent detection of terahertz radiation employing a continuous wave optical parametric source," *Review of Scientific Instruments,* vol. 82, 2011.
[53] D. P. Neikirk and D. B. Rutledge, "Air-bridge microbolometer for far-infrared detection," *Applied Physics Letters,* vol. 44, pp. 153-155, 1984.
[54] M. J. Golay, "The Theoretical and Practical Sensitivity of the Pneumatic Infra-Red Detector," *Review of Scientific Instruments,* vol. 20, pp. 816-820, 1949.
[55] S. M. Sze and K. K. Ng, *Physics of semiconductor devices*: Wiley.com, 2006.
[56] M. Tarasov, J. Svensson, J. Weis, L. Kuz'min, and E. Campbell, "Bolometer Based on Carbon Nanotubes," *JETP LETTERS,* vol. 84, 2006.
[57] V. Dobrovolsky, F. Sizov, Y. E. Kamenev, and A. Smirnov, "Ambient temperature or moderately cooled semiconductor hot electron bolometer for mm and sub-mm regions," *Opto-Electronics Review,* vol. 16, pp. 172-178, 2008.
[58] F. Sizov, V. Zabudsky, V. Dobrovolsky, N. Momot, Z. Tsybrii, M. Apats'ka*, et al.*, "THz/sub-THz detector based on electrons and holes heating by electromagnetic wave propagating along Hg1-xCdxTe layer," in *Proc. of SPIE Vol*, 2011, pp. 816728-1.
[59] P. Jayaweera, S. Matsik, A. Perera, Y. Paltiel, A. Sher, A. Raizman*, et al.*, "GaSb homojunctions for far-infrared (terahertz) detection," *Applied Physics Letters,* vol. 90, pp. 111109-111109-3, 2007.
[60] A. Perera, "5 Homo-and Heterojunction Interfacial Workfunction Internal Photo-Emission Detectors from UV to IR," *Semiconductors and Semimetals,* vol. 84, p. 243, 2011.
[61] M. Tarasov and L. Kuz'min, "Concept of a mixer based on a cold-electron bolometer," *Journal of Experimental and Theoretical Physics Letters,* vol. 81, pp. 538-541, 2005.
[62] A. Rostami, H. Rasooli, and H. Baghban, *Terahertz Technology* vol. 77: Springer, 2011.
[63] M. Shur, "Terahertz technology: devices and applications," in *Solid-State Circuits Conference, 2005. ESSCIRC 2005. Proceedings of the 31st European*, 2005, pp. 13-21.
[64] A. Lisauskas, D. Glaab, H. Roskos, E. Oejefors, and R. Pfeiffer, "Terahertz imaging with Si MOSFET focal-plane arrays," in *Proc. SPIE*, 2009, p. 72150J.
[65] F. Sizov, A. Golenkov, D. But, M. Sakhno, and V. Reva, "Sub-THz radiation room temperature sensitivity of long-channel silicon field effect transistors," *Opto-Electronics Review,* vol. 20, pp. 194-199, 2012.

[66] H. Hashiba, V. Antonov, L. Kulik, A. Tzalenchuk, P. Kleinschmid, S. Giblin*, et al.*, "Isolated quantum dot in application to terahertz photon counting," *Physical Review B,* vol. 73, p. 081310, 2006.

[67] O. Astafiev, S. Komiyama, T. Kutsuwa, V. Antonov, Y. Kawaguchi, and K. Hirakawa, "Single-photon detector in the microwave range," *Applied Physics Letters,* vol. 80, pp. 4250-4252, 2002.

[68] H. Manohara, E. Wong, E. Schlecht, R. Hunt, and P. Siegel, "Carbon nanotube Schottky diodes for high frequency applications," in *Infrared and Millimeter Waves and 13th International Conference on Terahertz Electronics, 2005. IRMMW-THz 2005. The Joint 30th International Conference on*, 2005, pp. 285-286.

[69] A. Rogalski and F. Sizov, "Terahertz detectors and focal plane arrays," *Opto-Electronics Review,* vol. 19, pp. 346-404, 2011.

[70] J. Grade, P. Haydon, and D. van der Weide, "Electronic terahertz antennas and probes for spectroscopic detection and diagnostics," *Proceedings of the IEEE,* vol. 95, pp. 1583-1591, 2007.

[71] A. Sharma and G. Singh, "Rectangular microstrip patch antenna design at THz frequency for short distance wireless communication systems," *Journal of Infrared, Millimeter, and Terahertz Waves,* vol. 30, pp. 1-7, 2009.

[72] P. H. Siegel, "Terahertz technology," *Microwave Theory and Techniques, IEEE Transactions on,* vol. 50, pp. 910-928, 2002.

[73] P. L. Richards, "Bolometers for infrared and millimeter waves," *Journal of Applied Physics,* vol. 76, pp. 1-24, 1994.

[74] P. Siegel and R. Dengler, "TERAHERTZ HETERODYNE IMAGING PART I: INTRODUCTION AND TECHNIQUES," *International Journal of Infrared and Millimeter Waves,* vol. 27, pp. 465-480, 2006/04/01 2006.

[75] D. Glaab, S. Boppel, A. Lisauskas, U. Pfeiffer, E. Ojefors, and H. G. Roskos, "Terahertz heterodyne detection with silicon field-effect transistors," *Applied Physics Letters,* vol. 96, pp. 042106-3, 2010.

[76] J. G. Simmons, "Generalized Formula for the Electric Tunnel Effect between Similar Electrodes Separated by a Thin Insulating Film," *Journal of Applied Physics,* vol. 34, pp. 1793-1803, 1963.

[77] J. Zmuidzinas and P. L. Richards, "Superconducting detectors and mixers for millimeter and submillimeter astrophysics," *Proceedings of the IEEE,* vol. 92, pp. 1597-1616, 2004.

[78] C. Y. E. Tong, R. Blundell, B. Bumble, J. A. Stern, and H. G. LeDuc, "Quantum limited heterodyne detection in superconducting non-linear transmission lines at sub-millimeter wavelengths," *Applied Physics Letters,* vol. 67, pp. 1304-1306, 1995.

[79] P. C. D. Hobbs, R. B. Laibowitz, and F. R. Libsch, "Ni/NiO/Ni tunnel junctions for terahertz and infrared detection," *Appl. Opt.,* vol. 44, pp. 6813-6822, 2005.

[80] E. Wiesendanger and F. Kneubühl, "Thin-film MOM-diodes for infrared detection," *Applied Physics A: Materials Science & Processing,* vol. 13, pp. 343-349, 1977.

[81] A. Sanchez, S. K. Singh, and A. Javan, "Generation of infrared radiation in a metal-to-metal point-contact diode at synthesized frequencies of incident fields: a high-speed broad-band light modulator," *Applied Physics Letters,* vol. 21, pp. 240-243, 1972.

[82] G. Rebeiz, W. Regehr, D. Rutledge, R. Savage, and N. Luhmann, Jr., "Submillimeter-wave antennas on thin membranes," *International Journal of Infrared and Millimeter Waves,* vol. 8, pp. 1249-1255, 1987/10/01 1987.

[83] U. R. Pfeiffer, E. Ojefors, A. Lisaukas, D. Glaab, and H. G. Roskos, "A CMOS focal-plane array for heterodyne terahertz imaging," in *Radio Frequency Integrated Circuits Symposium, 2009. RFIC 2009. IEEE*, 2009, pp. 433-436.
[84] D. P. Neikirk, W. W. Lam, and D. B. Rutledge, "Far-infrared microbolometer detectors," *International Journal of Infrared and Millimeter Waves,* vol. 5, pp. 245-278, 1984.
[85] S. I. Green, "Point Contact MOM Tunneling Detector Analysis," *Journal of Applied Physics,* vol. 42, pp. 1166-1169, 1971.
[86] H. W. Hübers, G. W. Schwaab, and H. P. Röser, "Video detection and mixing performance of GaAs Schottky-barrier diodes at 30 THz and comparison with metal-insulator-metal diodes," *Journal of Applied Physics,* vol. 75, pp. 4243-4248, 1994.
[87] S. Preu, S. Kim, R. Verma, P. G. Burke, M. S. Sherwin, and A. C. Gossard, "An improved model for non-resonant terahertz detection in field-effect transistors," *Journal of Applied Physics,* vol. 111, pp. 024502-9, 2012.
[88] J. G. Simmons, "Electric Tunnel Effect between Dissimilar Electrodes Separated by a Thin Insulating Film," *Journal of Applied Physics,* vol. 34, pp. 2581-2590, 1963.
[89] J. Fisher and I. Giaever, "Tunneling through thin insulating layers," *Journal of Applied Physics,* vol. 32, pp. 172-177, 1961.
[90] W. Brinkman, R. Dynes, and J. Rowell, "Tunneling conductance of asymmetrical barriers," *Journal of Applied Physics,* vol. 41, pp. 1915-1921, 1970.
[91] T. E. Hartman, "Tunneling Through Asymmetric Barriers," *Journal of Applied Physics,* vol. 35, pp. 3283-3294, 1964.
[92] J. A. Bean, Weeks, A., and Boreman, G. D. , "Performance Optimization of Antenna-Coupled Al/AlO_x/Pt Tunnel Biode Infrared Detectors," *IEEE Journal of Quantum Electronics,* vol. 47, p. 8, 2011.
[93] P. Maraghechi, A. Foroughi-Abari, K. Cadien, and A. Y. Elezzabi, "Enhanced rectifying response from metal-insulator-insulator-metal junctions," *Applied Physics Letters,* vol. 99, pp. 253503-253503-3, 2011.
[94] J. Simmons, "Conduction in thin dielectric films," *Journal of Physics D: Applied Physics,* vol. 4, p. 613, 1971.
[95] I. E. Hashem, N. H. Rafat, and E. A. Soliman, "Theoretical Study of Metal-Insulator-Metal Tunneling Diode Figures of Merit," *Quantum Electronics, IEEE Journal of,* vol. 49, pp. 72-79, 2013.
[96] D. Z. Y. Ting, E. T. Yu, and T. C. McGill, "Multiband treatment of quantum transport in interband tunnel devices," *Physical Review B,* vol. 45, pp. 3583-3592, 02/15/ 1992.
[97] O. Vallée, *Airy functions and applications to physics*: World Scientific, 2010.
[98] C. Cohen-Tannoudji, B. Diu, and F. Laloë, "Quantum mechanics," *New York,* vol. Volume 1, 1977.
[99] M. Depas, B. Vermeire, P. Mertens, R. Van Meirhaeghe, and M. Heyns, "Determination of tunnelling parameters in ultra-thin oxide layer poly-Si/SiO2/Si structures," *Solid-state electronics,* vol. 38, pp. 1465-1471, 1995.
[100] R. Lake and S. Datta, "Nonequilibrium Green's-function method applied to double-barrier resonant-tunneling diodes," *Physical Review B,* vol. 45, pp. 6670-6685, 03/15/ 1992.
[101] S. Datta, *Quantum transport: atom to transistor*: Cambridge University Press, 2005.

[102] A. Ghatak, K. Thyagarajan, and M. R. Shenoyu, "A novel numerical technique for solving the one-dimensional Schroedinger equation using matrix approach-application to quantum well structures," *Quantum Electronics, IEEE Journal of,* vol. 24, pp. 1524-1531, 1988.

[103] C. S. Lent and D. J. Kirkner, "The quantum transmitting boundary method," *Journal of Applied Physics,* vol. 67, pp. 6353-6359, 1990.

[104] J. Sun, R. Mains, K. Yang, and G. Haddad, "A self-consistent model of Γ-X mixing in GaAs/AlAs/GaAs quantum well structures using the quantum transmitting boundary method," *Journal of Applied Physics,* vol. 74, pp. 5053-5060, 1993.

[105] M. Leng and C. S. Lent, "Quantum transmitting boundary method in a magnetic field," *Journal of Applied Physics,* vol. 76, pp. 2240-2248, 1994.

[106] E. S. Daniel, X. Cartoixà, W. R. Frensley, D.-Y. Ting, and T. McGill, "Coupled drift-diffusion/quantum transmitting boundary method simulations of thin oxide devices with specific application to a silicon based tunnel switch diode," *Electron Devices, IEEE Transactions on,* vol. 47, pp. 1052-1060, 2000.

[107] R. H. Landau, *Quantum mechanics II*: Wiley.com, 2008.

[108] M. G. Chapline and S. X. Wang, "Analytical formula for the tunneling current versus voltage for multilayer barrier structures," *Journal of Applied Physics,* vol. 101, pp. 083706-083706-5, 2007.

[109] S. K. Masalmeh, H. K. E. Stadermann, and J. Korving, "Mixing and rectification properties of MIM diodes," *Physica B: Condensed Matter,* vol. 218, pp. 56-59, 2/1/ 1996.

[110] H. C. Torrey, C. A. Whitmer, S. A. Goudsmit, and L. B. Linford, *Crystal rectifiers*: McGraw-Hill New York, 1948.

[111] R. van der Heijden, H. Swartjes, and P. Wyder, "Contribution of the spreading resistance to high-frequency rectification in metal-metal point contacts," *Journal of Applied Physics,* vol. 55, pp. 1003-1011, 1984.

[112] S. Faris, T. Gustafson, and J. Wiesner, "Detection of optical and infrared radiation with DC-biased electron-tunneling metal-barrier-metal diodes," *Quantum Electronics, IEEE Journal of,* vol. 9, pp. 737-745, 1973.

[113] G. M. Elchinger, A. Sanchez, J. C. F. Davis, and A. Javan, "Mechanism of detection of radiation in a high-speed metal-metal oxide-metal junction in the visible region and at longer wavelengths," *Journal of Applied Physics,* vol. 47, pp. 591-594, 1976.

[114] *Micromanufacturing and Nanotechnology*. Berlin: Springer, 2006.

[115] A. A. Tseng, C. Kuan, C. D. Chen, and K. J. Ma, "Electron beam lithography in nanoscale fabrication: recent development," *Electronics Packaging Manufacturing, IEEE Transactions on,* vol. 26, pp. 141-149, 2003.

[116] K. Suzuki, B. Smith, and B. W. Smith, *Microlithography: science and technology* vol. 126: CRC press, 2010.

[117] R. L. Boxman, D. Sanders, and P. J. Martin, *Handbook of Vacuum Arc Science & Technology: Fundamentals and Applications*: William Andrew, 2008.

[118] *http://www.hht-eu.com/cms/Hitachi_SU-70_07_2006.html*.

[119] *http://nanolithography.gatech.edu/trdoc.html*.

[120] http://www.jeol.co.jp/en/products/list_sem.html.

[121] H. Takemura, H. Ohki, H. Nakazawa, Y. Nakagawa, M. Isobe, Y. Ochiai, *et al.*, "Performance of new E-beam lithography system JBX-9300FS," *Microelectron. Eng.,* vol. 53, pp. 329-332, 2000.

[122] D. M. Tennant, R. Fullowan, H. Takemura, M. Isobe, and Y. Nakagawa, "Evaluation of a 100 kV thermal field emission electron-beam nanolithography system," *Journal of Vacuum Science; Technology B,* vol. 18, pp. 3089-3094, 2000.

[123] G. S. May and C. J. Spanos, *Fundamentals of Semiconductor Manufacturing and Process Control*. Hoboken: John Wiley & Sons, Inc, 2006.

[124] R. L. Puurunen, "Surface chemistry of atomic layer deposition: A case study for the trimethylaluminum/water process," *Journal of Applied Physics,* vol. 97, pp. 121301-121301-52, 2005.

[125] S. George, A. Ott, and J. Klaus, "Surface chemistry for atomic layer growth," *The Journal of Physical Chemistry,* vol. 100, pp. 13121-13131, 1996.

[126] B. S. Lim, A. Rahtu, and R. G. Gordon, "Atomic layer deposition of transition metals," *Nature materials,* vol. 2, pp. 749-754, 2003.

[127] S. M. George, "Atomic layer deposition: an overview," *Chemical Reviews,* vol. 110, pp. 111-131, 2009.

[128] M. Leskelä and M. Ritala, "Atomic layer deposition chemistry: recent developments and future challenges," *Angewandte Chemie International Edition,* vol. 42, pp. 5548-5554, 2003.

[129] Y. Yasuoka, T. Sakurada, D. P. Siu, and T. K. Gustafson, "Resistance dependence of detected signals of MOM diodes," *Journal of Applied Physics,* vol. 50, pp. 5860-5864, 1979.

[130] R. Suzuki, N. Taoka, M. Yokoyama, S.-H. Kim, T. Hoshii, T. Maeda*, et al.*, "Impact of atomic layer deposition temperature on HfO[sub 2]/InGaAs metal-oxide-semiconductor interface properties," *Journal of Applied Physics,* vol. 112, pp. 084103-5, 2012.

[131] S. Rockwell, D. Lim, B. A. Bosco, J. H. Baker, B. Eliasson, K. Forsyth*, et al.*, "Characterization and Modeling of Metal/Double-Insulator/Metal Diodes for Millimeter Wave Wireless Receiver Applications," in *Radio Frequency Integrated Circuits (RFIC) Symposium, 2007 IEEE*, 2007, pp. 171-174.

[132] H. Geng, *Semiconductor Manufacturing Handbook*. New York: McGraw-Hill, 2005.

[133] S. Franssila, *Introduction to Microfabrication*. Chichester, West Sussex, England: J. Wiley, 2004.

[134] R. Brown, *RF/microwave Hybrids: Basics, Materials, and Processes*. Boston: Kluwer Academic Publishers, 2003.

[135] A. B. Hoofring, V. J. Kapoor, and W. Krawczonek, "Submicron nickel-oxide-gold tunnel diode detectors for rectennas," *Journal of Applied Physics,* vol. 66, pp. 430-437, 1989.

[136] J. P. Uyemura, *Physical design of CMOS integrated circuits using L-Edit*: PWS Publishing Company, 1995.

[137] X. Huang, W.-C. Lee, C. Kuo, D. Hisamoto, L. Chang, J. Kedzierski*, et al.*, "Sub 50-nm FinFET: PMOS," in *Electron Devices Meeting, 1999. IEDM'99. Technical Digest. International*, 1999, pp. 67-70.

[138] Y. Nishioka, N. Homma, H. Shinriki, K. Mukai, K. Yamaguchi, A. Uchida*, et al.*, "Ultra-thin Ta2O5 dielectric film for high-speed bipolar memories," *Electron Devices, IEEE Transactions on,* vol. 34, pp. 1957-1962, 1987.

[139] Y. Nishioka, H. Shinriki, and K. Mukai, "Time Dependent, Dielectric Breakdown Characteristics of Ta2 O 5/SiO2 Double Layers," *Journal of the Electrochemical Society,* vol. 136, pp. 872-873, 1989.

[140] J. Robertson, "Band offsets of wide-band-gap oxides and implications for future electronic devices," *Journal of Vacuum Science & Technology B,* vol. 18, pp. 1785-1791, 2000.

[141] G. D. Wilk, R. M. Wallace, and J. M. Anthony, "High-κ gate dielectrics: Current status and materials properties considerations," *Journal of Applied Physics,* vol. 89, pp. 5243-5275, 2001.

[142] M. Houssa, *High-K gate dielectrics*: Bristol; Philadelphia : Institute of Physics, c2004., 2004.

[143] N. Alimardani, J. F. Conley, E. W. Cowell, J. F. Wager, M. Chin, S. Kilpatrick*, et al.*, "Stability and bias stressing of metal/insulator/metal diodes," in *Integrated Reliability Workshop Final Report (IRW), 2010 IEEE International*, 2010, pp. 80-84.

[144] S. Grover and G. Moddel, "Applicability of Metal/Insulator/Metal (MIM) Diodes to Solar Rectennas," *Photovoltaics, IEEE Journal of,* vol. 1, pp. 78-83, 2011.

[145] S. A. Campbell, D. C. Gilmer, X.-c. Wang, M.-t. Hsieh, H.-S. Kim, W. L. Gladfelter*, et al.*, "MOSFET transistors fabricated with high permitivity TiO2 dielectrics," *Electron Devices, IEEE Transactions on,* vol. 44, pp. 104-109, 1997.

[146] S. A. Campbell, H.-S. Kim, D. C. Gilmer, B. He, T. Ma, and W. L. Gladfelter, "Titanium dioxide (TiO2)-based gate insulators," *IBM journal of research and development,* vol. 43, pp. 383-392, 1999.

[147] S. Krishnan, H. La Rosa, E. Stefanakos, S. Bhansali, and K. Buckle, "Design and development of batch fabricatable metal–insulator–metal diode and microstrip slot antenna as rectenna elements," *Sensors and Actuators A: Physical,* vol. 142, pp. 40-47, 2008.

[148] P. Esfandiari, G. Bernstein, P. Fay, W. Porod, B. Rakos, A. Zarandy*, et al.*, "Tunable antenna-coupled metal-oxide-metal (MOM) uncooled IR detector (Invited Paper)," 2005, pp. 470-482.

[149] E. N. Grossman, T. E. Harvey, and C. D. Reintsema, "Controlled barrier modification in Nb/NbOx/Ag metal insulator metal tunnel diodes," *Journal of Applied Physics,* vol. 91, pp. 10134-10139, 2002.

[150] N. Alimardani, E. William Cowell, J. F. Wager, J. F. Conley, D. R. Evans, M. Chin*, et al.*, "Impact of electrode roughness on metal-insulator-metal tunnel diodes with atomic layer deposited Al2O3 tunnel barriers," *Journal of Vacuum Science & Technology A,* vol. 30, 2012.

[151] J. Robertson, "High dielectric constant oxides," *The European Physical Journal - Applied Physics,* vol. 28, pp. 265-291, 2004.

[152] M. A. Caravaca, J. C. Miño, V. J. Pérez, R. A. C. and, and C. A. Ponce, "Ab initio study of the elastic properties of single and polycrystal TiO_2, ZrO_2 and HfO_2 in the cotunnite structure " *Condensed Matter* vol. 21, p. 11, 2009.

[153] "Mechanical Properties, Hardness and Electronic Structures of New Post-Cotunnite Phase (Fe2P-type) of TiO2," *Physica B: Condensed Matter,* 2013.

[154] L. L. Chang, P. J. Stiles, and L. Esaki, "Electron Tunneling between a Metal and a Semiconductor: Characteristics of Al-Al2O3-SnTe and −GeTe Junctions," *Journal of Applied Physics,* vol. 38, pp. 4440-4445, 1967.

[155] I. T. Wu, N. Kislov, and J. Wang, "Metal-insulator-metal tunneling diode for uncooled infrared high-speed detectors," 2010, pp. 76792K-76792K-7.

[156] H. Haug and S. Schmitt-Rink, "Basic mechanisms of the optical nonlinearities of semiconductors near the band edge," *Journal of the Optical Society of America B,* vol. 2, pp. 1135-1142, 1985/07/01 1985.

[157] N. Alimardani and J. F. Conley, "Step tunneling enhanced asymmetry in asymmetric electrode metal-insulator-insulator-metal tunnel diodes," *Applied Physics Letters,* vol. 102, pp. -, 2013.

[158] W. F. Brinkman, R. C. Dynes, and J. M. Rowell, "Tunneling Conductance of Asymmetrical Barriers," *Journal of Applied Physics,* vol. 41, pp. 1915-1921, 1970.

[159] T.-C. Tien, F.-M. Pan, L.-P. Wang, C.-H. Lee, Y.-L. Tung, S.-Y. Tsai*, et al.*, "Interfacial energy levels and related properties of atomic-layer-deposited Al2O3 films on nanoporous TiO2 electrodes of dye-sensitized solar cells," *Nanotechnology,* vol. 20, p. 305201, 2009.

[160] P. Periasamy, H. L. Guthrey, A. I. Abdulagatov, P. F. Ndione, J. J. Berry, D. S. Ginley*, et al.*, "Metal–Insulator–Metal Diodes: Role of the Insulator Layer on the Rectification Performance," *Advanced Materials,* vol. 25, pp. 1301-1308, 2013.

APPENDICES

Appendix I Email Showing Permission to Use Figure 3.7

USF

Mail

More

COMPOSE

Inbox (818)
Starred
Important
Sent Mail
Drafts (124)
[Imap]/Sent
[Imap]/Trash (26)
Follow up

Follow up

Try now

Unable to reach University of South Florida Mail. Please check your internet connection or company's network settings. Help

Search people...

Edikan Archibong
Henry Cabra
Al-Aakhir Ahad R...
Algarin amaris, P...
Cesar Morales

Permission to reproduce an image from your paper Inbox x

Adebimpe Ajayi <oajayi@mail.usf.edu> Feb 4
to riikka.puurunen

Hello,

I would like to reproduce Figure 2 from your paper titled "Surface chemistry of atomic layer deposition: A case study for the trimethylaluminum/water process". The reproduce figure will appear in my dissertation. Please let me know if you approve

Thanks

Olawale

Puurunen Riikka <Riikka.Puurunen@vtt.fi> Feb 4
to me

Dear Olawale,

Thank you for the request – yes, you have my permission to re-use it.

Greetings,
Riikka

From: Adebimpe Ajayi [mailto:oajayi@mail.usf.edu]
Sent: 04 February 2014 08:50
To: riikka.puurunen@iki.fi
Subject: Permission to reproduce an image from your paper

Appendix II Email Showing Permission to Use Figure 1.3

USF

Mail

COMPOSE

Inbox (818)
Starred
Important
Sent Mail
Drafts (124)
[Imap]/Sent
[Imap]/Trash (26)
Follow up

Try now

Unable to reach University of South Florida Mail. Please check your internet connection or company's network settings. Help

Search people...

Edikan Archibong
Henry Cabra
Al-Aakhir Ahad R...
Algarin amaris, P...
Cesar Morales

More

143

Permission to reproduce an image from your book Inbox x

Adebimpe Ajayi <oajayi@mail.usf.edu>
to leeys

Feb 3

Hello Dr. Lee,

I would like to reproduce Figure 1.1 from your book titled "Principles of Terahertz Science and Technology", that was published by Springer. The reproduced image would feature in my dissertation. Please let me know if you approve.

Thanks

Olawale

On Mon, Feb 3, 2014 at 2:30 AM, Adebimpe Ajayi <oajayi@mail.usf.edu> wrote:

> Hello Dr. Lee,
>
> I would like to reproduce Figure 1.1 from your book titled "Principles of Terahertz Science and Technology", that was published by Springer. The reproduced image would feature in my dissertation. Please let me know if you approve.
>
> Thanks
>
> Olawale

Yun-Shik Lee
to me

Feb 3

I permit you to reproduce Fig 1.1 from my book on the condition that you make a proper reference.

Yun-Shik Lee
Professor
Department of Physics
Oregon State University

Appendix III Email Showing Permission to Use Figure 1.3(b), Figure 3.3, and Figure 3.4

USF

Mail ▾

More ▾

COMPOSE

Inbox (819)

Starred

Important

Sent Mail

Drafts (124)

[Imap]/Sent

[Imap]/Trash (26)

Follow up

Gokhan (4)

Try now

Unable to reach University of South Florida Mail. Please check your internet connection or company's network settings. Help

Permission to reproduce some of the images in the SEM, E-Beam training handbook   Inbox x

Adebimpe Ajayi <oajayi@mail.usf.edu>   Feb 3

to Robert, Robert

Hello Rob,

I need your permission to reproduce some of the images of the tools at the center training courses. This will include, SEM, Hitachi, Karl Suss, and some other tools in the clea room.

The reproduced images will appear in my dissertation. Please let me know if you approve.

Thanks,

Olawale
Thanks

Olawale

Tufts, Robert   Feb 3

to me

Yes go ahead

--- Original Message ---

Appendix IV Email Showing Permission to Use Figure 5.5, and Figure 5.6

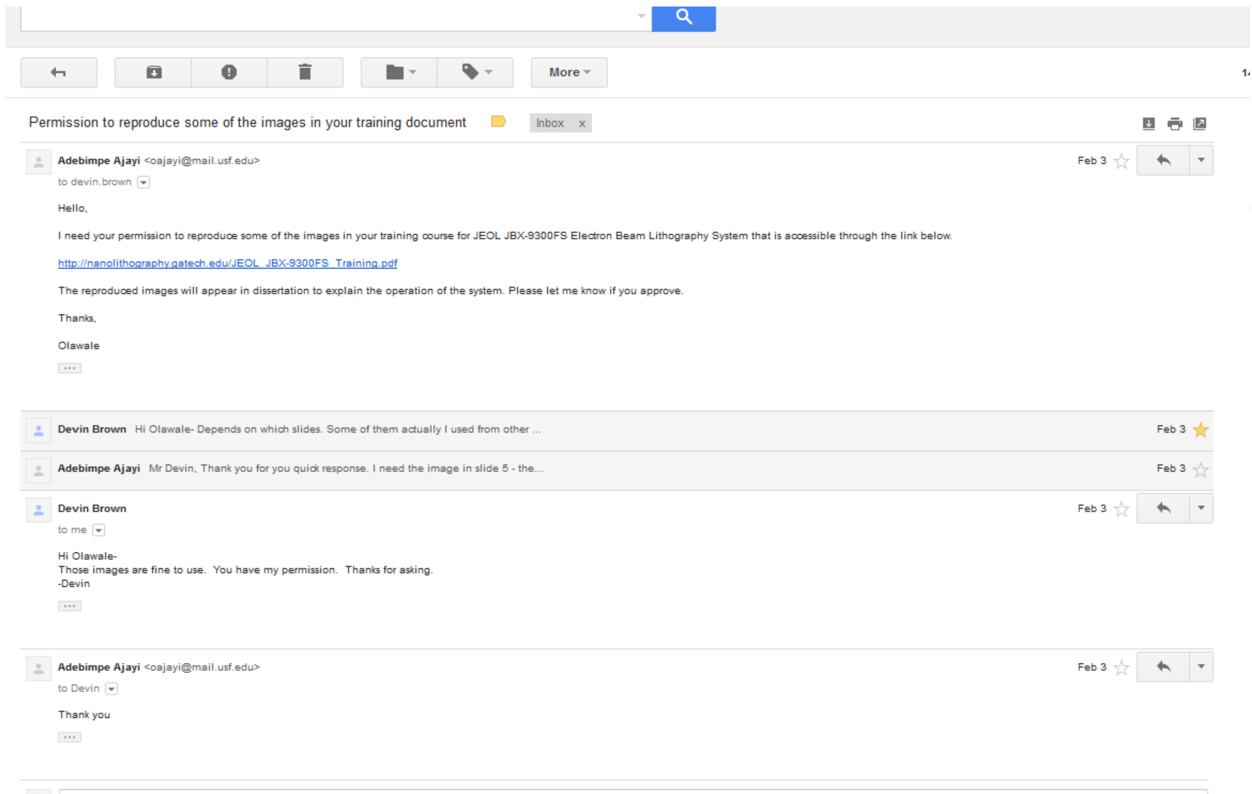

More

Permission to reproduce some of the images in your training document   Inbox x

Adebimpe Ajayi <oajayi@mail.usf.edu>   Feb 3
to devin.brown

Hello,

I need your permission to reproduce some of the images in your training course for JEOL JBX-9300FS Electron Beam Lithography System that is accessible through the link below.

http://nanolithography.gatech.edu/JEOL_JBX-9300FS_Training.pdf

The reproduced images will appear in dissertation to explain the operation of the system. Please let me know if you approve.

Thanks,

Olawale

Devin Brown Hi Olawale- Depends on which slides. Some of them actually I used from other ...   Feb 3

Adebimpe Ajayi Mr Devin, Thank you for you quick response. I need the image in slide 5 - the...   Feb 3

Devin Brown   Feb 3
to me

Hi Olawale-
Those images are fine to use. You have my permission. Thanks for asking.
-Devin

Adebimpe Ajayi <oajayi@mail.usf.edu>   Feb 3
to Devin

Thank you